Analysis of the influence of the hydrodynamics in hydrotreating of diesel oil in trickle bed reactors via MRI-measurements

Analyse des Einflusses der Hydrodynamik auf die hydrierende Entschwefelung von Dieselöl in Rieselbettreaktoren mittels MRI-Messungen

Zur Erlangung
des akademischen Grades eines

DOKTORS DER INGENIEURWISSENSCHAFTEN

(Dr.-Ing.)

von der Fakultät für Chemieingenieurwesen und Verfahrenstechnik des Karlsruher Instituts für Technologie (KIT)

genehmigte

DISSERTATION

von
Dipl.-Ing. Ngoc Luan Nguyen
aus Binhdinh, Vietnam

Tag des Kolloquiums: 12. 05. 2011

Referent: Prof. Dr.-Ing. Rainer Reimert

Korreferent: Prof. Dr.-Ing. Lothar Oellrich

Vorwort

Diese Arbeit entstand während meiner Tätigkeit als wissenschaftlicher Mitarbeiter am Lehrstuhl für Chemie und Technik im Bereich Gas, Erdöl und Kohle des Engler-Bunte-Institut der Universität Karlsruhe (TH) in den Jahren 2000 bis 2005. An dieser Stelle möchte ich all jenen danken, die für das Gelingen dieser Arbeit beigetragen haben.

Zusammenfassung

Dieselfraktionen werden durch katalytische Hydrierung der Schwefelverbindungen mit Wasserstoff entschwefelt. Dieser Prozeß wird meistens in Rieselbettreaktoren bei Temperaturen zwischen 300°C und 400°C und bei einem Druck von 30 bar bis 80 bar durchgeführt. Da die Anforderungen an der Produkte der Hydrierung ständig steigen, wird das Testen von neuen Katalysatoren und von veränderten Betriebsbedingungen in Laborreaktoren immer wichtiger. In der Literatur wird häufig berichtet, dass die Umsatzgrade in solchen Laborreaktoren deutlich unter den in den industriellen Anlagen erzielbaren Umsatzgraden liegen. Die wesentlich niedrigeren Flüssigkeitsbelastung in den Laborreaktoren scheinen dafür verantwortlich zu sein, den die Einflüsse der fluiddynamischen Nichtidealitäten und der äußeren Stofftransportvorgänge nimmt mit sinkenden Fluidgeschwindigkeit zu. Für die Auslegung von Rieselbettreaktor und für das Scale-up sind daher detaillierte Kenntnisse über die Fluiddynamik der Flüssigphase notwendig.

In der vorliegenden Arbeit wurde der Einfluss der Fluiddynamik und des äußeren Stofftransportes auf die hydrierende Entschwefelung von Dieselöl in einem Laborreaktor untersucht. Die geschah einerseits in Experimenten mit einem „Kaltmodell" zur Untersuchung der Fluiddynamik der Gas- und der Flüssigphase, ohne Reaktionen durchzuführen. Andererseits wurden die Reaktionen der hydrierenden Entschwefelung von Dieselöl in einer Laboranlage untersucht. Anschießend wurde ein Dreiphasenreaktormodell für die Vorausberechnung der hydrierenden Entschwefelung, aufbauend auf früher ermittelten experimentellen Daten, entwickelt.

Zur Untersuchung der Fluiddynamik wurde das Magnetic Resonance Imaging (MRI) als nicht invasive Methode angewendet, um Porosität, Flüssigkeitssättigung, Kanalbildung und Benetzungsgrad von Katalysatorschüttungen zu untersuchen und quantitativ zu bestimmen. Dazu wurde die örtliche Verteilung der flüssigen Phase von mit Luft/Wasser bzw. mit Stickstoff/Diesel durchströmten Katalysatorschüttungen zweidimensional und dreidimensional vermessen. Eine spezielle Apparatur wurde aus nicht magnetischem Material konstruiert, um Experimente auch bei erhöhtem Druck bis 20 bar und bei erhöhter Temperatur bis 150°C durchführen zu können.

Die detail Analyse der Porositäts- und zur Flüssigkeitsverteilung in den Schüttungen beweist, dass sich MRI durch deutlich gute örtliche Auflösung (100 μm bis 200 μm) hervorragend zum quantitativen Nachweis von Struktur und Phasenverteilung in porösen Medien eignet. Aus vermessenen dreidimensionalen Hohlraumgeometrien konnten die radialen und die axialen Abhängigkeiten der Porosität verschiedener Packungen ermittelt werden. Es hat sich gezeigt, dass die radiale Porositätsverteilung nicht nur von dem Verhältnis Reaktordurchmesser (D) zu der Partikelgröße (d_p) sondern auch von der Partikelgeometrie abhängt. Im Vergleich zur Schüttung mit kugelförmigen Partikeln weisen die Schüttungen aus Partikeln mit komplexer Geometrie (z.B. Zylinder, Trilobe) eine bessere Homogenität der

Porositätsverteilung innerhalb der Schüttung auf. Bei der statistischen Betrachtung der radialen Porositäten stellte sich heraus, dass die örtliche Porositätsverteilung in einer Schüttung als Gaußsche oder logarithmische Verteilungsfunktion ermittelt werden kann.

Aus zweidimensional ortsaufgelösten Messungen einer einphasigen Strömung konnten eine radiale Geschwindigkeitsverteilung im Zusammenhang mit der radialen Porositätsverteilung ermittelt werden. Es zeigte sich, dass das Fluid in Bereichen hoher Porosität mit hoher Geschwindigkeit fließt, da es in diesen Zonen bzw. Randzonen weniger Widerstand erfährt. Daraus ergeben sich ähnliche Kurvenverläufe für die radialen Porositäts- und Geschwindigkeitsverteilungen.

Die gemessenen dreidimensionalen Hohlraumstrukturen der Packungen eignen sich gut für die Erstellung des geometrischen Gitters für eine Strömungssimulation. Mit dem kommerziellen CFD Program FLUENT ist es möglich, die aus den MRI-Messungen vorliegende digitale Schüttungsgeometrie in einem Rechengitter abzubilden. Bisher wurde die Simulation nur an einphasige Strömung beschränkt werden. Für tiefe Kenntnisse auf dem Gebiet der zweiphasigen Strömung in komplexen Schüttungssystemen besteht noch der Bedarf für zukünftige Arbeiten sowohl der experimentellen Geschwindigkeitsmessungen mit MRI als auch der CFD Simulationen.

Anhand der Datenanalyse von den aufgenommenen dreidimensionalen Bildern der Schüttungen während der Experimente mit zweiphasiger Strömung war es nun erstmals möglich, die lokale Flüssigkeitsverteilung lokal in der Schüttung quantitativ zu untersuchen. Die Auswertung der Messungen bei verschiedenen Temperaturen zeigt, dass der flüssige Sättigungsgrad in Rieselbettreaktoren mit zunehmenden Temperaturen abnimmt. Dieser Effekt beruht auf den Einfluss der viskosen Kraft auf die flüssigen Phase in der Schüttung. Die Flüssigkeitsviskosität nimmt mit steigenden Temperaturen ab. Dadurch wird die viskose Kraft geringer und verursacht eine abnehmende Flüssigkeitsmenge in der Schüttung.

Der Einfluss der Temperatur, des Drucks, der Verweilzeit und des Gas/Öl-Verhältnisses auf die hydrierende Entschwefelung und auf die Hydrierung von aromatischen Schwefelverbindungen in Dieselkraftstoffen wurde in der Laboranlage untersucht. Verwendet wurde ein kommerzieller NiMo/γAl$_2$O$_3$-Katalysator. Die Temperatur wurde zwischen 300 °C und 380 °C, der Druck zwischen 40 bar und 80 bar und die Raumgeschwindigkeit zwischen 0.5 h^{-1} und 4 h^{-1} variiert. Parallel wurde das Verweilzeitverhalten in der Flüssigphase bei hohen Temperaturen und Drücken vermessen, um die Wichtigkeit der axialen Dispersion zu bestimmen. Danach musste der Einfluss der axialen Dispersion bei der Modellierung berücksichtigt werden.

Modellrechnungen zeigen, dass der Einfluss der wichtigen fluiddynamischen Parameter und des Gas-Flüssigkeitsstofftransports auf die Umsätze der hydrierenden Entschwefelung im Laborreaktor mit für die Praxis tauglicher Genauigkeit wiedergegeben wird. Durch die Verwendung der Ergebnisse der

Fluiddynamik im Kaltmodell konnten die Experimente im Labormaßstab besser ausgewertet werden. Das Modell kann daher für die Optimierung der Rieselbettreaktoren und schließlich für Scale-up bzw. Scale-down Anwendungen verwendet werden.

Summary

Diesel fractions are desulfurized by catalytic hydrogenation of sulfur components with hydrogen as a reactant. This process is so-called hydrodesulfurization (HDS) process and is typically carried out at temperatures between 300°C to 400°C and at pressures from 30 bars to 80 bars in trickle bed reactors. Since the product specifications are steadily becoming more severe, the testing of new catalysts and of modified operating conditions in laboratory reactors becomes increasingly important. In the literature, however, relative low conversion degrees in laboratory reactors are frequently reported in comparison with those in industrial ones. The significantly lower liquid velocities in laboratory reactor liquid seem to be responsible for such differences as the influence of the inhomogeneities in liquid flow increase with decrease of liquid velocities. For a meaningful evaluation of test results and for a reliable upscaling of trickle bed reactors, detail knowledge of fluid dynamic behaviour of gas and liquid phases in laboratory reactors is necessary.

In the present work, the influence of fluid dynamics and extraparticle mass transfer phenomena on the hydrodesulfurization of diesel oil in a laboratory reactor was examined. This was carried out on the one hand in experiments with a "cold flow" reactor without occurring chemical reactions in order to investigate the fluid dynamic behaviours of gas and liquid phases. On the other hand, the hydrogenation of sulfur components in diesel oils was investigated in a laboratory reactor. Finally, a heterogeneous model based on the previous experimental results was developed to predict the desulfurization performance of trickle bed reactors.

For investigation of the fluid dynamics, magnetic resonance imaging (MRI) technique was used as a non-invasive method to measure quantitatively the porosity, liquid saturation, channelling and wetting efficiency of the packed beds. The local distribution of liquid phase was then determined from two-dimensional (2D) and three-dimensional (3D) magnetic resonance images, which were acquired for 2-phase flow within the packings. The gas-liquid systems used in experiments were air-water, nitrogen-diesel and hydrogen-diesel. A special apparatus made of a nonmagnetic material was constructed that allowed in-situ measurements of gas and liquid distributions in packings at elevated pressure and temperature up to 20 bars and 150°C.

The detailed analysis of porosity and liquid distributions inside the packings have proven that MRI technique thanks to its ability to produce images of a high spatial resolution (100 mm to 200 mm) becomes a valuable tool for quantitative

measurement of geometrical structure and phase distribution within packed beds. From the measured 3-dimensional mages of void geometries the radial and axial dependence of porosity in packings containing particles of different shapes can be determined. It is indicated that the radial porosity distribution depends not only on the ratio of reactor diameter to particle diameter (D/d_p) but also on the particle geometries. Packings of particles having complex shapes (i.e. cylinder, trilobe) present a better homogeneity in porosity distribution as compared to that of packing of spherical particles. Results of a statistical analysis show that the randomly local porosity distribution inside the packings can be described by Gaussian or logarithm probability density functions.

The relationship between of radial velocity and radial porosity distribution can be determined from spatially 2-dimensional measurements of single phase liquid flow inside the packings of spheres. It is clearly recognized that liquid flows faster through the regions of higher porosities, where smaller resisting frictional forces exist. Therefore, the same profiles of radial velocities and porosities were observed.

The measured data of 3-dimensional packing structures are suitable for reconstruction of geometrical grid models which are necessary for computer fluid dynamic (CFD) simulations. The first step of this work is therefore to implement detailed geometrical information of randomly packed beds of spheres and trilobes into commercial CFD program FLUENT and to generate an appropriate grid for the simulation. In this work, CFD simulation was restricted for single phase flow only. For deeper understanding of two phase flow in complex packing structures, however, future works should pay attention to both experimental measurements of liquid velocity during two-phase flow with MRI-technique and CFD simulation.

Since the MRI technique can provide full 3D-images of the liquid phase distribution in the packed beds, it is capable to quantify the hydrodynamic parameters in both local and bed scales. The analysis of experimental data at different temperatures revealed that the liquid saturation reduces gradually as the experimental temperature increases. The effect of temperature on the liquid phase distribution can be explained by means of the viscous resistant force. Because the viscosity of diesel oil drops significantly when temperature increases, the viscous force acting on solid/liquid interface becomes smaller which causes a gradual reduction of the liquid saturation.

The influence of temperature, pressure, liquid hourly space velocity (LHSV) and gas/oil ratio on the hydrodesulfurization and hydrodearomatization reactions of diesel fuels was examined in a laboratory plant. A commercial Ni/Mo-γAl$_2$O$_3$ catalyst (Criterion 424) was used. The experiments were performed at different temperatures in the range from 300°C to 380°C, pressures from 40 bar to 80 bar and LHSV from 0.5 h^{-1} to 4 h^{-1}. Subsequently, the residence time distribution experiments were carried out at high temperatures and pressures, in order to examine the importance of axial dispersion at laboratory scale. The influence of the axial dispersion was therefore considered in the reactor model.

The model reproduces correctly the influence of important fluid dynamic parameters (axial dispersion, liquid saturation) and mass transfer resistance on the conversion of hydrodesulfurization reaction in a quantitative manner. The results obtained from fluid dynamic experiments with "cold flow" model contribute to a better evaluation of HDS experiments in laboratory reactors.The model is therefore capable to optimize the operation of trickle bed reactors and is consequently helpful for scale up/scale down purposes.

Contents

Notation

Symbol	Description	Definition	Unit
A	Cross section, surface	L^2	m^2
A_0	Reactor cross section	πR^2	m^2
$A_{cat,L}$	Catalyst surface covered with liquid in reactor	$\sum_{i=1}^{n} S_{p,L,i}$	m^2
$A_{cat,0}$	Catalyst surface in reactor	$\sum_{i=1}^{n} S_{p,i}$	m^2
AARE (%)	Average absolute relative error	$\dfrac{1}{m}\sum_{i=1}^{m}\left|\dfrac{\varepsilon_{exp,i}-\varepsilon_{pred,i}}{\varepsilon_{exp,i}}\right|\times 100$	–
a_l	Gas-liquid interfacial area per unit of reactor volume	$\dfrac{A_{G/L,total}}{V_0}$	$\dfrac{m^2}{m^3}$
a_S	Liquid-solid interfacial area per unit of reactor volume	$\dfrac{A_{L/S,total}}{V_0}$	$\dfrac{m^2}{m^3}$
a_v	External catalyst surface per reactor volume		$\dfrac{m^2}{m^3}$
B_0	Static magnetic field	$\mu_0\,\mu_r\,I_{err}\dfrac{N}{L}$	$\dfrac{V\,s}{m^2}$
B_1	Radio frequency field	–	$\dfrac{V\,s}{m^2}$
$C_{i,0}$	Initial concentration of compound i	N/V	mol/dm^3
$C_{i,res}$	Residual concentration of compound i at reactor outlet	N/V	mol/dm^3
C_i	Concentration of compound i	N/V	mol/dm^3
$C_{A,iS}$	Concentration of reactant A at catalyst pellet external surface	N/V	mol/dm^3
D	Diameter of reactor	L	m
D_{ax}	Axial dispersion coefficient	–	m^2/s
d_p	Characteristic length of a particle	$6V_p/S_p$	m
E	Activation energy	–	J/mol
F	Force	$m\dfrac{du}{dt}$	$\dfrac{kg\,m}{s^2}$
$f(x)$	Function in general	–	–
$G_x,\,G_y,\,G_z$	Magnetic gradients	$\dfrac{\partial B}{\partial x},\,\dfrac{\partial B}{\partial y},\,\dfrac{\partial B}{\partial z}$	$\dfrac{V\,s}{m^3}$
H_i	Henry coefficient	$C_{G,i}^{*}/C_{L,i}^{*}$	–

h_b	Bulk liquid holdup	$\dfrac{V_L}{V_0} = \varepsilon_b \beta_b$	–
I	Angular momentum	$\sqrt{I(I+1)}\hbar$	Js
I	Nuclear spin quantum number	–	–
K_{ad}	Adsorption coefficient of H_2S	–	m/s
k	Reaction coefficient		
k_G	Gas phase mass transfer coefficient	–	m/s
K_L	Global liquid side mass transfer coefficient	$\dfrac{1}{K_L} = \dfrac{1}{k_L} + \dfrac{1}{Hk_G}$	–
k_L	Gas side gas-liquid mass transfer coefficient	$\dfrac{\Phi_L}{aV_0\left(C_L - C_L^*\right)}$	–
k_S	Solid phase mass transfer coefficient	–	m/s
k_r	Surface reaction rate constant	–	$\dfrac{m^3}{kg\,cat.s}$
L	Length of reactor	–	m
LHSV	Liquid hourly space velocity	$3600 \cdot \dfrac{{}^V\Phi_L}{V_0}$	h^{-1}
M_0	Equilibrium magnetisation	$M_0 = N\dfrac{\gamma^2\hbar^2 I(I-1)}{3k_BT}B_0$	Am^2
m	Mass	–	kg
m	Number of annulli	–	–
m_{cat}	Weight of catalyst bed	–	kg
m_p	Weight of a catalyst particle	–	kg
n	Number of slices in a 3D-image	–	–
n_1, n_2	Reaction order of sulfur and hydrogen	–	–
N	Number of moles	–	mol
N	Number of nuclei	–	–
N_L	Number of liquid filled voxels in a segment	–	–
N_G	Number of gas filled voxels in a segment	–	–
N_V	Number of void space voxels in a segment	$N_L + N_G$	–

p	Absolute total pressure	$\dfrac{F}{A}$	$\dfrac{kg}{m\,s^2}$
p_i	Partial pressure of substance i (H$_2$, H$_2$S)	–	$\dfrac{kg}{m\,s^2}$
R	Radius of reactor	$\dfrac{D}{2}$	m
r	Radial coordinate	L	m
r_i	Reaction rate per unit of mass	$\dfrac{1}{m_{cat}}\dfrac{dN_i}{dt}$	–
S_p	Surface area of a catalyst particle	–	m^2
T	Temperature	–	K
T_1	Spin-lattice relaxation time	t	s
T_2	Spin-spin relaxation time	t	s
t	Time	–	s
u	Velocity	$\dfrac{\mathrm{d}L}{\mathrm{d}t}$	$\dfrac{m}{s}$
u_{0L}	Liquid superficial velocity	$\dfrac{{}^V\Phi_L}{A_0}$	$\dfrac{m}{s}$
u_{0G}	Gas superficial velocity	$\dfrac{{}^V\Phi_G}{A_0}$	$\dfrac{m}{s}$
u_G	Interstitial gas velocity	$\dfrac{{}^V\Phi_G}{\varepsilon_b(1-\beta_b)A_0}$	$\dfrac{m}{s}$
u_L	Actual or interstitial liquid velocity	$\dfrac{{}^V\Phi_L}{\varepsilon_b\beta_{b,d}A_0}$	$\dfrac{m}{s}$
V	Volume	L^3	m^3
$V_{H,bed}$	Void volume of a catalyst bed excluding the pores' volume of total catalyst particles	L^3	m^3
$V_{H,cat}$	Pores' volume of total catalyst particles in a packed bed	L^3	m^3
$V_{H,p}$	Volume of pores in a catalyst particle	L^3	m^3
$V_{L,d}$	Dynamic liquid volume (freely moving part of external liquid volume)	L^3	m^3
V_L	External liquid volume lying between particles	$V_{L,d} + V_{L,st}$	m^3

$V_{L,int}$	Internal liquid volume to be held in catalysts' pores	L^3	m³
$V_{L,st}$	Static liquid volume (non-active part of external liquid volume remaining around the catalyst contacting points)	L^3	m³
V_0	Volume of reactor	$V_S + V_{H,cat} + V_{H,bed}$	m³
V_p	Volume of a catalyst particle including the pores	L^3	m³
V_S	Volume of solid phase in a catalyst bed	L^3	m³
x	Space coordinate	L	m
x	Molar fraction in the liquid phase		–
X	Conversion	$\dfrac{C_{i,0} - C_i}{C_{i,0}}$	–
y	Space coordinate	L	m
y	Molar fraction in the gas phase		–
z	Space coordinate, distance from the inlet of reactor	L	m

Greek symbols

Symbol	Description	Definition	Unit
β_b or β_{ext}	Bulk liquid saturation	$\dfrac{V_L}{\varepsilon_b V_0}$	–
β_{int}	Internal liquid saturation	$\dfrac{V_{L,int}}{V_{H,bed}}$ *in most cases the particles' pores are filled with liquid due to capillary forces, therefore,* $\dfrac{V_{H,cat}}{V_{H,bed}} = \dfrac{V_{H,cat}}{\varepsilon_b V_0} =$ $= \dfrac{1}{\varepsilon_b}\left(1 - \dfrac{\rho_b}{\rho_s} - \varepsilon_b\right) = \dfrac{\rho_b}{\varepsilon_b}\left(\dfrac{1}{\rho_p} - \dfrac{1}{\rho_s}\right)$	–
$\beta_{b,t}$	Total bulk liquid saturation	$\beta_b + \beta_{int} = \beta_{b,d} + \beta_{b,st} + \beta_{int}$	–
$\beta_{b,d}$	Bulk dynamic liquid saturation	$\dfrac{V_{L,d}}{V_{H,bed}} = \dfrac{V_{L,d}}{\varepsilon_b V_0}$	–
$\beta_{b,st}$ or $\beta_{b,st,ext}$	Bulk (external) static liquid saturation	$\dfrac{V_{L,st}}{V_{H,bed}} = \dfrac{V_{L,st}}{\varepsilon_b V_0}$	–

$\beta_{b,st,t}$	Total static liquid saturation	$\beta_{b,st} + \beta_{int} = \dfrac{V_{L,st}}{V_{H,bed}} + \dfrac{V_{H,cat}}{V_{H,bed}}$	–
β_r	Radial liquid saturation	$\dfrac{V_{L,rj}}{\varepsilon_{rj}V_{0,rj}} = \dfrac{1}{n} \cdot \sum\limits_{i=1}^{n} \beta_{zi,\,rj}$	–
β_z	Vertical liquid saturation	$\dfrac{V_{L,zi}}{\varepsilon_{zi}V_{0,zi}} = \dfrac{1}{m} \sum\limits_{j=1}^{m} \beta_{zi,rj}$	–
$\beta_{zi,rj}$	Local liquid saturation of the annulus rj in slice zi extracted from a MRI-image	$\dfrac{V_{L,zi,rj}}{\varepsilon_{zi,rj}V_{0,zi,rj}} = \left.\dfrac{N_{L,}}{N_L + N_G}\right|_{zi,\,rj}$	–
Δ	Difference	–	–
∇	Nabla-operator	$\left(\dfrac{\partial}{\partial x}; \dfrac{\partial}{\partial y}; \dfrac{\partial}{\partial z}\right)$	–
δ	Filmdicke	L	m
ε_b or ε_{ext}	Bulk porosity of a catalyst bed or external porosity	$\dfrac{V_{H,bed}}{V_0}$	–
ε_{int}	Internal porosity of a catalyst bed	$\dfrac{V_{H,cat}}{V_0} = 1 - \dfrac{\rho_b}{\rho_s} - \varepsilon_b = \rho_b\left(\dfrac{1}{\rho_p} - \dfrac{1}{\rho_s}\right)$	–
ε_p	Catalysts' porosity	$\dfrac{V_{H,cat}}{V_{cat}} = 1 - \dfrac{\rho_p}{\rho_s}$	–
ε_t	Total porosity of a catalyst bed	$\varepsilon_b + \varepsilon_{int} = \dfrac{V_{H,bed}}{V_0} + \dfrac{V_{H,cat}}{V_0} = 1 - \dfrac{\rho_b}{\rho_s}$	–
$\varepsilon_{zi,rj}$	Local axial porosity of the annulus rj in slice zi extracted from a MRI-image	$\dfrac{V_{H,zi,rj}}{V_{0,zi,rj}} = \left.\dfrac{N_L}{N_0}\right|_{zi,\,rj}$	–
η	Dynamic viscosity	$\dfrac{\tau}{\nabla u}$	$\dfrac{kg}{m\,s}$
$\eta_{ce,b}$	Bulk wetting efficiency	$\dfrac{A_{cat,L}}{A_{cat,0}} = \dfrac{1}{m}\sum\limits_{j=1}^{m}\eta_{ce,rj} = \dfrac{1}{n}\sum\limits_{i=1}^{n}\eta_{ce,zi}$	–
$\eta_{ce,r}$	Radial wetting efficiency	$\eta_{ce,r} = \dfrac{1}{n} \cdot \sum\limits_{i=1}^{n}\eta_{ce,\,zi,rj}$	–
$\eta_{ce,z}$	Vertical wetting efficiency	$\eta_{ce,z} = \dfrac{1}{m} \cdot \sum\limits_{j=1}^{m}\eta_{ce,\,zi,rj}$	–
$\eta_{ce,zi,rj}$	Local wetting efficiency	$\dfrac{A_{cat,L,zi,rj}}{A_{cat,0,zi,rj}} = \left.\dfrac{N_{SL}}{N_{SL,0}}\right|_{zi,\,rj}$	–
ν	Kinematic viscosity	$\dfrac{\eta}{\rho}$	$\dfrac{m^2}{s}$

ρ	Density	$\dfrac{m}{V}$	$\dfrac{kg}{m^3}$
ρ_b	Reactor loading (mass of catalyst per reactor volume)	$\dfrac{m_{cat}}{V_0} = \dfrac{m_{cat}}{V_S + V_{H,cat} + V_{H,bed}}$	$\dfrac{kg}{m^3}$
ρ_p	Catalyst particles' density including the pores	$\dfrac{m_{cat}}{V_{cat}} = \dfrac{m_{cat}}{V_S + V_{H,cat}}$	$\dfrac{kg}{m^3}$
ρ_s	Density of solid phase of a catalyst bed	$\dfrac{m_{cat}}{V_S}$	$\dfrac{kg}{m^3}$
σ	Surface tension	$\dfrac{F}{2L}$	$\dfrac{kg}{s^2}$
$\sigma(\%)$	Standard deviation	$\dfrac{\sqrt{\sum\limits_{i=1}^{m}\left(\left|\dfrac{\varepsilon_{exp,i} - \varepsilon_{pred,i}}{\varepsilon_{exp,i}}\right| - AARE\right)^2}}{m-1} \times 100$	
$^V\Phi$	Volumetric flow rate	$\dfrac{dV}{dt}$	$\dfrac{m^3}{s}$
$^n\Phi$	mole flow rate	$\dfrac{dn}{dt}$	$\dfrac{mol}{s}$
ϕ	Packing sphericity factor	$\dfrac{S_p}{S_{sphere}}\ for\ V_p = V_{sphere}$	$-$
τ	Shear stress	$\dfrac{F}{A}$	$\dfrac{N}{m^2}$
τ	Mean residence time	$\dfrac{\varepsilon_b \beta_b V_0}{^V\Phi_L}$	s
ω	Larmor precessing frequency	$\dfrac{1}{t}$	$\dfrac{1}{s}$
ω_0	Larmor frequence	γB_0	$\dfrac{1}{s}$

Dimensionsless numbers

Symbol	Description	Definition
Bo	Bond-number	$\dfrac{\rho_L g d_p^2}{\sigma}$
Bo	Bodenstein-number	$\dfrac{u_L d_p}{D_{ax}}$
Ga_L	Galileo-number	$\dfrac{d_p g}{v_L^2}$
Pe	Péclet-number	$\dfrac{u_L L}{D_{ax}}$

Re_G	Reynolds-number for the gas phase	$\dfrac{u_{0G}\, d_p}{\nu_G}$	
Re_L	Reynolds-number for the liquid phase	$\dfrac{u_{0L}\, d_p}{\nu_L}$	
Sh	Sherwood-number	$\dfrac{\beta\, d_p}{D}$	

Constants

Symbol	Description	Definition	Unit
g	gravitational acceleration	9,80665	$\dfrac{m}{s^2}$
h	Planck's constant	$6{,}626 \cdot 10^{-34}$	Js
$\hbar$	Planck's constant	$\dfrac{h}{2\pi}$	Js
k_B	Boltzmann constant	$\dfrac{R}{N_A}$	$\dfrac{J}{K}$
N_A	Avogadro constant	$6{,}022 \cdot 10^{-23}$	$\dfrac{1}{mol}$
R	Universal gas constant	8,314	$\dfrac{J}{molK}$
γ	gyromagnetic constant	42,577 (for ^{1}H Isotop)	$\dfrac{MHz}{T}$

Subscripts

Index	Meaning
0	Time or initial value
ax	axial
b	bulk
cat	catalyst
d	dynamic
exp	experience
ext	external
int	internal
G	gas phase
H	void

L	liquid phase
p	particle
pred	prediction
r_j	annular segment j in a slice of a MRI 3D-image
S	solid phase
st	static
z_i	z_i^{th}-slice in a MRI 3D-image

Superscripts

Index	Meaning
*	Thermodynamic equilibrium

Abbreviations

DMDS	Dimethyl-disulfide
DB	benzolthiophene
DBT	dibenzolthiophene
GO	Gas oil
HC	Hydrocarbon
HDA	Hydrodearomatization
HDN	Hydrodenitrogenation
HDS	Hydrodesulfurization
HDT	Hydrotreating
LCO	Light cycle oil
MRI	Magnetic resonance imaging
NMR	Nuclear magnetic resonance
ppm	Weight fraction in parts per million
RTD	Residence time distribution
TBR	Trickle bed reactor
ULSD	Ultra low sulfur diesel
wt%	Weight fraction in percent
XS	Pseudocomponent with sulfur

1 Problem statement and purpose of the study

Driven by the efforts in reducing air pollution, especially in large urban areas, government regulations in many countries call for reduction of impurities in transportation fuels. The environmental legislation for product specifications is mainly focusing on reducing sulfur oxide, nitrogen oxides, aromatics, fuel vapour and soot particulate emissions. Especially the reduction of sulfur oxides (SOx) and nitrogen oxides (NOx) originated from fuel combustion that cause acid rain, is probably the major concern of petroleum refining industry worldwide. Due to the ernormous progress in reducing sulfur in fuels in the last decades, the problem of acid rain has almost been solved. However, it is known that sulfur existing in fuels even at a small concentration can poison vehicle catalytic converters for exhaust gas treatment thereby increasing e.g. nitrogen oxides and hydrocarbon emissions.

To cope with this problem, the new regulation will further reduce the remaining sulfur in diesel oil and, therefore, creates a major challenge for fuel processing. In addition, the increasing demand for diesel fuel has put refineries all over the world under strong pressures to increase the capacities of their hydrodesulfurization units. By 2005/2006, refiners in the EU, USA and in Japan were required to reduce sulfur levels to below 15 ppmw. For instance, driven by ambitious German environmental policy, the German refiners have already produced ultra low sulfur diesel (ULSD) fuels of 10 ppmw since 2003, much earlier than other countries in the European Union. Fig. 1.1a shows that to a good approximation diesel sulfur specification in Germany has been tightened strongly over the last two decades.
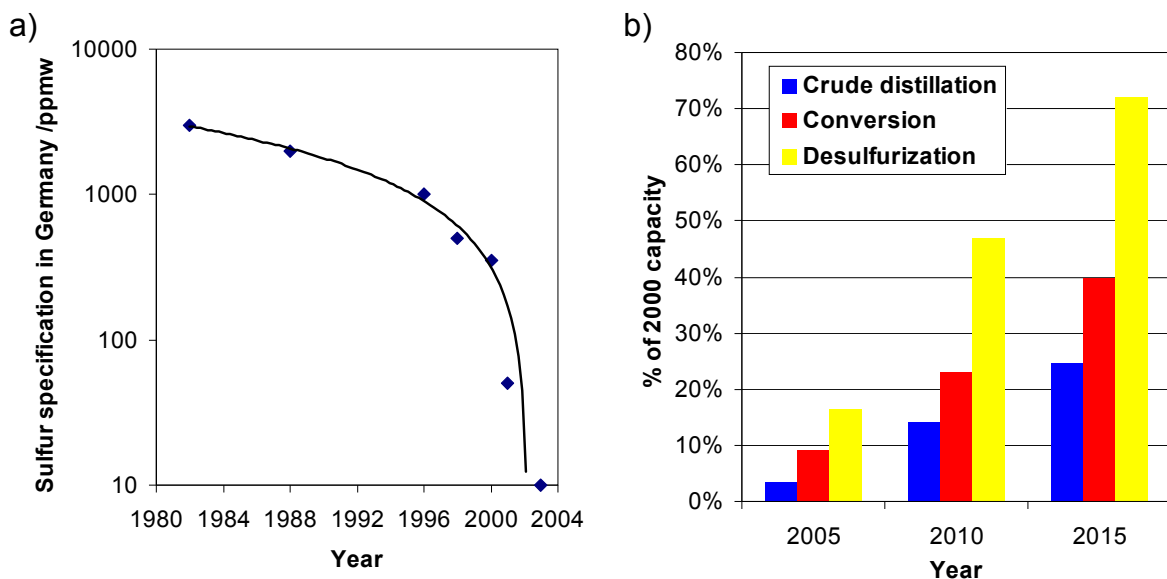

Figure 1.1: a) Development of diesel sulfur specification in Germany (logarithmic scale) over the years b) Predictions of incremental global capacity requirements during 2005 – 2015 [Har04].

According to various estimation models, global capacity requirements for refining processes, especially for desulfurization will increase rapidly during 2005 - 2015 as shown in Fig. 1.1b [Sil04; Har04]. In year 2009, world crude oil distillation capacity was about 86.10^6 b/d. An equivalence of 84% of that capacity was devoted to further conversion to higher value products by catalytic processes. The desulfurization capacity accounts for about 45% of the conversion capacity. By 2015, global middle distillate desulfurization will increase by over 100% percent and consequently the costs for total gasoline and distillate desulfurization could reach $12 billion/year [EIA10, Fin04].

From the technical point of view, the goal of reaching such an extremely low sulfur diesel specification (< 15 ppmw) will scale exponentially in difficulty, because desulfurized middle distillates have a low total sulfur content but a disproportionally high concentration of refractory sulfur species. This primary goal could only be achieved by using high performance hydrotreating catalysts and by modifying the reactor design in order to improve the processes' efficiency. Therefore, a great amount of research and development effort has already been devoted in the areas of catalyst improvement and process optimization.

In order to avoid waste of material, time and cost, modifications of the operating conditions and new catalyst systems are tested in laboratory plants with small scale reactors before application in industrial units. However, the down-scaling of trickle bed reactors is generally limited due to the influences of hydrodynamic factors. The length of the laboratory reactors is much shorter than that of industrial ones which leads to lower liquid velocities when operating the same liquid hourly space velocity (LHSV). These differences in velocities and in reactor geometries lead to a number of phenomena such as mixing, axial dispersion and bypass flow etc. in the catalyst bed, which consequently reduce the overall conversion of desulfurization reaction in laboratory reactors. In this case the experimental results from small reactors do not reflect the intrinsic kinetics alone. If these results are extrapolated without a correction of predictions of the performance in the commercial unit will be wrong. Therefore, a fundamental understanding of the hydrodynamics of trickle bed reactors is necessary to evaluate the scale-up behaviour.

In this context, the main objective of this work is to determine the impact of hydrodynamic non-idealities on the hydrotreating of gas oil fractions in bench scale reactors. To achieve this goal, two experimental studies have been carried out. On the one side, the hydronamic behavior of two phase flow in packed beds was investigated by using Magnetic Resonance Imaging (MRI) technique. On the other side, catalytic experiments were carried out in a bench scale reactor, whose geometry and catalyst bed are the same as it is used in hydrodynamic experiments. On the basis of both experimental results, a multiphase reactor model was developed to predict the hydrodesulfurization performances.

2 Basic theories and background of the work

2.1 Hydrotreating of middle disttillates

A modern oil refinery has a large number of highly integrated physical and chemical processes, which are employed to convert crude oil into valuable products such as liquid petroleum gas (LPG), gasoline, jet and diesel fuels, heating oils, wax, lubricants, bitumen and petrochemical products, Fig. 2.1.
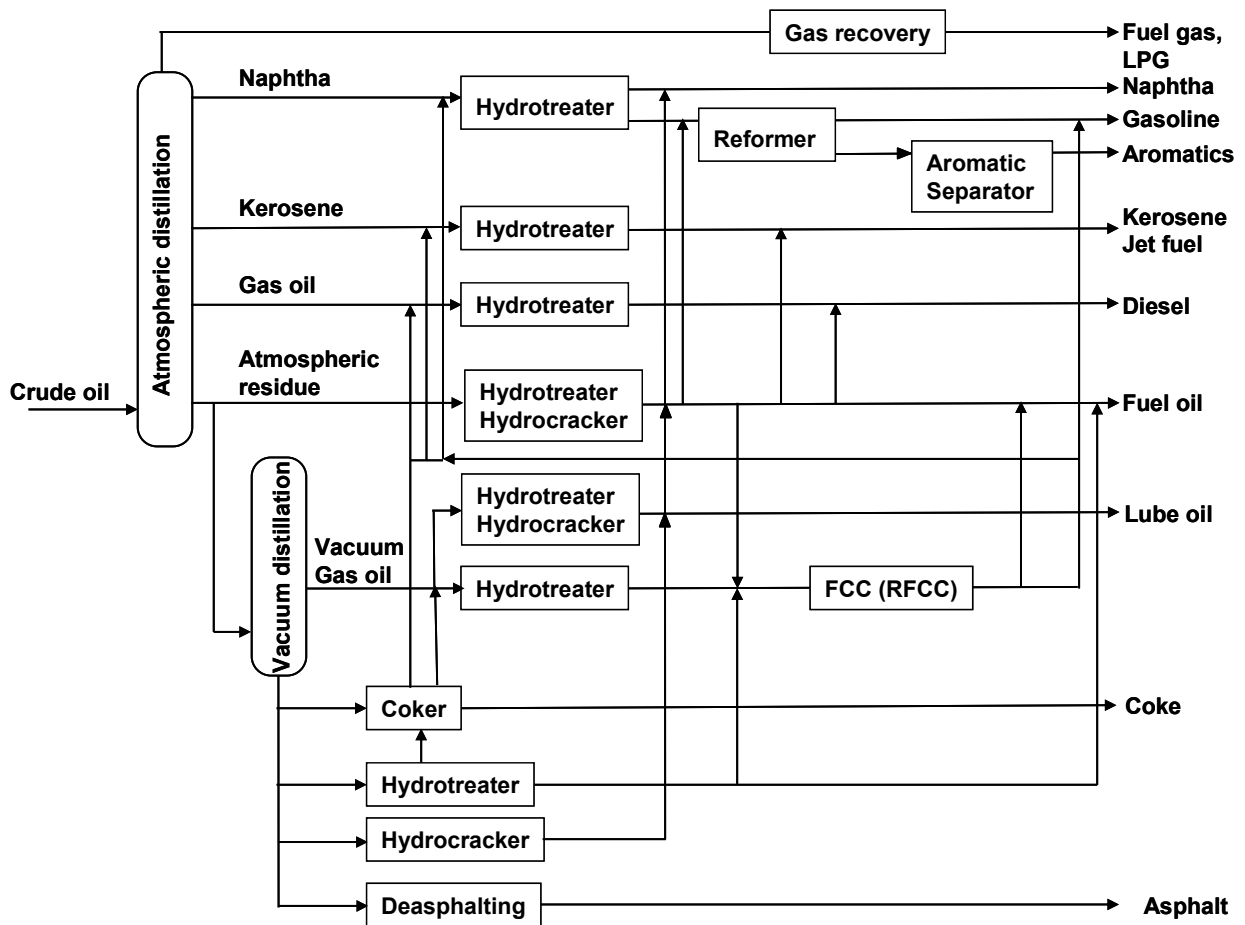
Figure 2.1: Schematic representation of an oil refinery with possible locations of hydrotreating units (adapted from [Bab03])

Crude oil is first desalted and then fed to the atmospheric distillation column, in which it is split into different boiling fractions. The resulting streams are further treated and purified by a variety of conversion processes to meet quality requirements and environmental specifications for various products. As can be seen in Fig. 2.1, almost all main fuel streams have to undergo hydrotreating to meet the new fuel specification. In hydrotreating processes, contaminants such as sulfur, nitrogen, polyaromatics and metals are converted by reaction with hydrogen in the presence of suitable catalysts. Because sulfur concentration in crude oils (Tab.2.1) is much

higher than that of other contaminants, its removal has become one of the most important technological challenges in refining industry.

Type of crude, origin	Sulfur content of crude, wt %	Sulfur content of atmospheric residue, wt %
Ekofisk, Norway	0.1	0.3
Forties, United Kingdom	0.3	0.6
Es-Sider, Libya	0.5	0.9
Alaska, USA	1.0	1.5
West Siberia, Russia	1.5	2.6
Isthmus, Mexico	1.6	3.0
Kuwait, Kuwait	2.5	3.8
Arabian light, Saudi Arabia	3.0	4.5

Table 2.1: Sulfur contents of selected crude oils and of their atmospheric residues [Ull06]

Hydrotreating for sulfur removal is called hydrodesulfurization (HDS). The global increase in the use of transportation fuels, especially diesel fuel and the increased production of high sulfur crude oils [Sei08, IEA07] require a large investment for the installation of adequate hydrotreating capacities in refineries. This work focuses on hydrodesulfurization of middle distillates, which are predominantly used as automotive diesel fuels and as heating fuels. In addition to HDS, diesel fuel processing must also satisfy other related diesel fuel specifications such as cetane number, oxidation stability and colour throughout the HDS process cycle [Luc00].
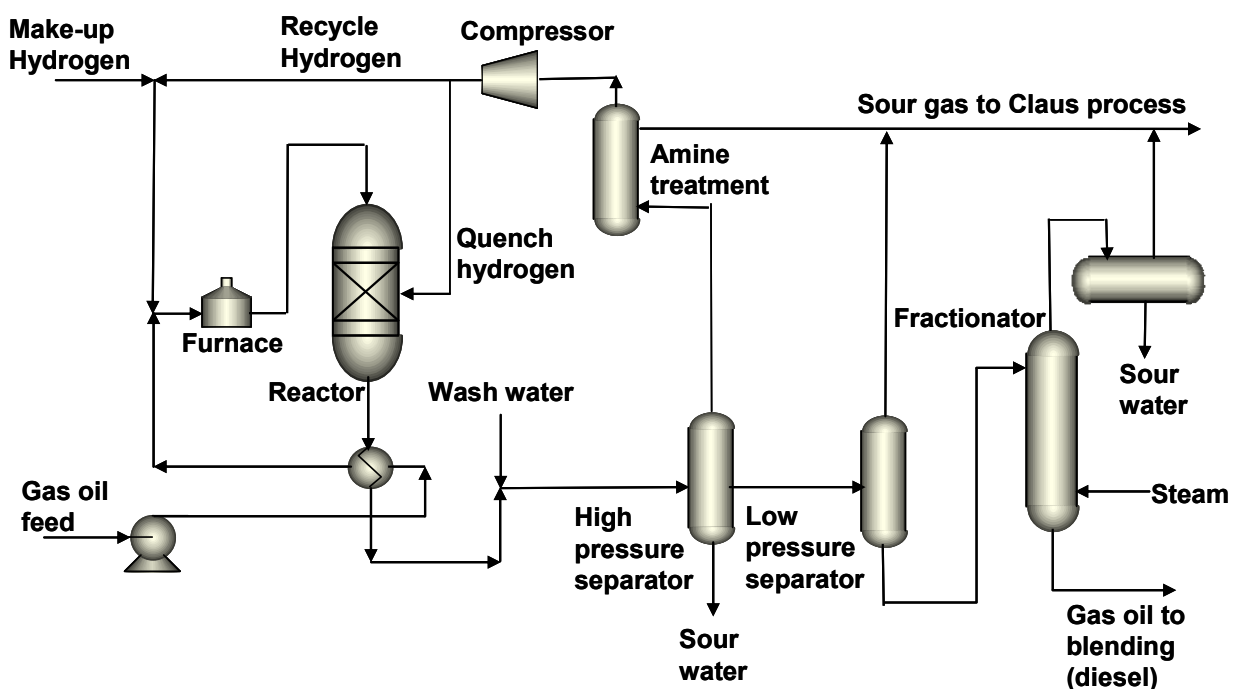

Figure 2.2: Typical single stage hydrodesulfurization flow unit scheme for middle distillate oil

Conventional HDS technology usually consists of a single stage process in which hydrodesulfurization reaction takes place in a fixed bed reactor mostly operated in trickle mode and under elevated pressure in the range from 20 to 100 bars. The flow diagram of a typical single stage HDS process is illustrated in Fig. 2.2. The feed stream consists of a gas oil fraction and contains contaminants like sulfur and nitrogen compounds. It is mixed with recycle and with make-up hydrogen. The quantity of the added hydrogen is significantly higher than stoichiometric need because of the following reasons:

- The high pressure improves the solubility of gaseous hydrogen and hence positively influences the hydrodesulfurization reaction and the heat transfer.

- The excess of hydrogen slows down the formation of coke and thus prolongs the life of catalyst.

The mixture is then heated in a furnace to reaction temperature (320 °C – 350 °C) and flows cocurrently downwards through the catalyst bed which has a length of 20 m – 30 m. In the reactor, sulfur and nitrogen compounds in the feedstock are converted into H_2S and NH_3, respectively. The reactions are exothermic and a too high temperature provokes the formation of coke. Therefore the catalyst bed is sometimes interrupted by so-called "quenches" where a cold stream of hydrogen rich gas is injected. The reaction products leave the reactor and after cooling enter two in series arranged liquid/gas separators. The hydrogen-rich gas from the high-pressure separation is recycled to be combined with the feedstock. The low-pressure gas stream rich in H_2S is first washed by means of amines (neutralization reaction). The sour gas from the regenerator for the solvent is processed in a gas treating unit (Claus process) where about 95% of the sulfur is recovered. The liquid product stream is normally sent to a stripping column for removal of solved H_2S and other undesirable components. The single stage process is generally applied for diesel specifications allowing sulfur contents in the order of 500 ppm.

Feed stock	Paraffinic crude			Naphthenic crude		Vacuum distillate		Vacuum residue		Deasphalted vacuum residue
Process	Atmospheric distillation			Atmospheric distillation		FCC LCO	Hydro cracking	Vis breaking	Coking	Hydro cracking
Yield, wt %	30.3	32.8	36.7	29.2	47.2	10-15	30-40	5-15	35	20
Density at 15°C (kg/m^3)	835	825	843	827	856	930	814	845	900	807
Distillation, °C										
IBP	170	180	170	180	170	170	220	170	170	260
FBP	370	375	400	350	370	370	370	370	370	380
Cloud point, °C	5	-2	1	-10	-20	-5	-17	-4	-8	-13
Pour point, °C	-12	-9	-6	-18	-33	-14	-20	-18	-20	-18
Centane number	50	51	54	45	43	24	64	40	28	70
Sulfur, wt %	0.12	0.04	0.83	0.8	0.09	2.8	0.001	2.33	2.1	0.0005

Table 2.2: Typical yields and characteristics of blending components available for the diesel pool (source IFP) [Luc00]

Diesel fuels are often blends of straight-run gas oil and other refinery streams. Tab. 2.2 gives typical characteristics for potential diesel pool blending stocks including the wide variety of feedstock sulfur contents and cetane numbers. The table also shows that most feedstocks except those from hydrocracking units will have to undergo hydrodesulfurization before being sent to the diesel pool.

2.1.1   Technical approaches to deep and ultra-deep desulfurization

Although HDS processes are in use since 1930, improvement is still necessary due to the economic and environmental reasons. Especially in the last few years, the ultra low sulfur specification (< 10 ppm) for transportation fuels becomes one of the major challenges faced by oil refineries. Refiners were to revamp existing units or even have to build grass root units for production of ultra low sulfur diesel (ULSD). In this section, various options for the revamp and some new HDS processes are presented:

a) Application of catalysts with higher activity

The employment of the most active hydrotreating catalysts or catalytic systems can improve considerably the desulfurisation performance of the existing hydrotreating units. For example catalysts developed by Akzo Nobel (KF757, KF848, Nebula), Haldor Topsøe (TK573, TK 574) or Criterion, series "Ascent" and "Centinel" have 300 % - 350 % higher desulfurizing activity compared to those used in the 1980s [Cou01, Tor05]. However, the use of improved catalysts alone can reduce the sulfur concentration from 350 ppm down to 50 ppm, therefore, more active catalysts will have to be developed to meet the forthcoming sulfur specification (<10 ppm) in transportation fuels.

b) Adjustment of the feed with respect to final boiling point or feed composition

The distillation curve, particularly the distillation end point of the feedstock, has a pronounced impact on operating conditions of deep HDS. Investigation of the desulfurization of various sulfur species indicates that the most difficult to remove (called refractory compounds), which are bound in aromatic rings, are associated with the higher boiling point fractions. One of the most efficient ways for the production of ULSD is to use "easier feeds", as straight run gas oil or light gas oil. Many of the existing units can produce ULSD by means of "cutting off" the refractory sulfur compounds (for example dibenzothiophenes), contained in feeds with high final boiling ends and in feeds with high aromatic levels (as catalytic gas oil from FCC). However, even for using such easy feeds, it will be necessary to use higher activity catalysts.

c) Rise of operating temperature

This alternative has quite limited efficiency and causes additional costs due to the shorter cycles between catalyst regenerations. This method, however, has to be applied for feeds having high concentrations of aromatic compounds.

d) Improvement of gas/liquid distribution internals

To ensure efficient utilization of all the catalyst in the reactor, it is essential to attain a uniform distribution of the feedstock and the hydrogen throughout the entire catalyst bed. Topsøe has developed a dense flexible tray, which creates highly uniform liquid distribution. The tests with Topsøe's TK 554 catalyst indicate that an improved vapour-liquid distributor can reduce the reaction temperature necessary to meet a 50 ppm sulfur level by 10°C, which in turn would increase catalyst life and allow a cycle length from 10 to 18 months [Bin00].

e) Increase of the hydrogen / feed ratio

The increase of circulating gas reduces the inhibiting effect of H_2S and NH_3, and will increase the desulfurization catalyst activity. However, this impact is rather low. For example, the increase of the H_2/ feed ratio by 50 % can reduce the reaction temperature by about 5 – 8°C. The applicable H_2/ feed ratio depends on the hydraulics and the compressors' capacity.

f) Increase of H_2 partial pressure

Total operating pressure in the reactor seldom can be increased but the extension of H_2 partial pressure is an efficient way for improvement of desulfurization reaction. This can be accomplished by recycle gas scrubbing or improvement of fresh gas quality. The fresh gas purity can be maximized by addition of a pressure swing adsorption PSA to the hydrogen source.

g) Installation of a two-stage reactor system

To further reduce the sulfur content without decreasing the throughput, additional catalyst volume can be installed. One way of doing this is to install an additional reactor operated either in cocurrent/cocurrent or in cocurrent/countercurrent mode (Fig. 2.3 a and 2.3 b). Generally, in the first stage the sulfur and nitrogen concentrations are reduced to levels that allow the application of noble metal (Pt, Pd) catalysts in the second stage to improve at the same time other fuel specifications such as cetane number or aromatics content via hydrodearomatization (HDA) reactions. Because the application of noble metal catalysts for deep HDS is limited by their sulfur resistance, an interstage removal of H_2S and NH_3 is essential. Conventional HDS reactors operate with co-current supply of oil and hydrogen. As the reaction progresses down the reactor, the reaction slows down considerably for two reasons: (1) the hydrogen partial pressure reduces as hydrogen is consumed and (2) the H_2S formed inhibits the reaction rates. The use of a countercurrent reactor can provide a more preferable concentration profile. The main advantage of this operation mode is the high hydrogen partial pressure and the low H_2S

concentration at the final stage of the second reactor that favor the conversion of the most refractory sulfur compounds.

a)   b)

Figure 2.3: Schematic representation of two-stage reactors a) cocurrent configuration b) countercurrent configuration [Rei99]

2.1.2 Hydrodesulfurization reactions

Sulfur present in the gas oil fractions can be classified in aliphatic and thiophenic (aromatic) sulfur compounds. The low-boiling gas oil fractions contain mainly aliphatic compounds: mercaptans, sulfides and disulfides. They are very reactive under conventional hydrotreating conditions and therefore easily converted. High boiling gas oil fractions like light cycle oil (LCO) and coker gas oil contain predominantly thiophenic rings such as refractory benzothiophene (BT) and dibenzothiophene (DBT). Methyl-substituted BTs and DBTs are even more difficult to desulfurize than non-substituted ones because of steric hindrances through the akyl groups [Sch99, Te03, Moc96]. Fig. 2.4 illustrates the qualitative relationship between the reactivities of some representative sulfur compounds and their ring sizes associated with their boiling temperatures [Sch99]. It is clearly shown in this figure that, most refractory sulfur compounds remaining in Brent gas oil fuel at sulfur level lower than 500 ppmw are the dibenzolthiophenes with alkyl substituents at the 4- and/or 6-position, and are lower in HDS reactivities. To match the current sulfur specification (< 50 ppm) mandated in many countries, the petroleum refining industry is facing a major challenge to overcome the difficulty in converting these refractory compounds in

diesel oil fractions, when the quality of crude oils continue to decline in terms of increased sulfur content and decreased API gravity.
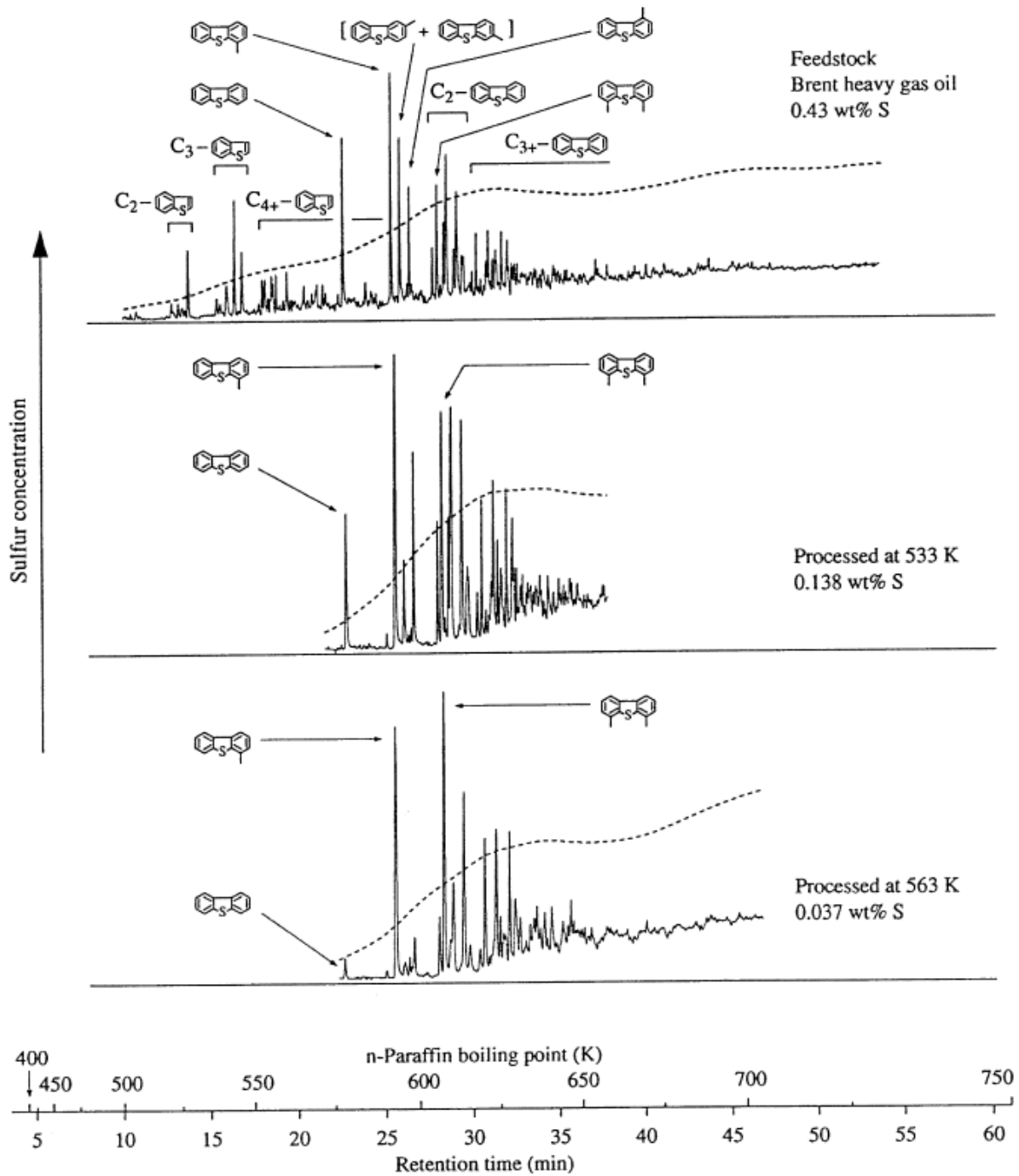

Figure 2.4: HDS reactivities of various sulfur compounds in Brent heavy gas oil, GC-PFPD chromatograms [Sch99]. Curves are normalized as corresponding to the sulfur amount in the 600 – 750 K boiling range.

Conventional HDS of organic sulfur compounds is exothermic and no thermodynamic limitation exists under industrial conditions [Kab99]. Substantial progress has been made in the fundamental understanding of the HDS reaction mechanism, and kinetics as well as the development of hydrotreating catalysts was reviewed several

9

times [Whi98, Te03, Son03, Ho04]. Two distinct pathways for the HDS of sulfur compounds (Fig. 2.5) are discussed. The first is direct hydrogenolysis. Almost all forms of mercaptans, sulfides and disulfides as well as the majority of BTs and unsubstituted DBTs are removed by this pathway. In the second pathway the aromatic rings in the DBT structure are first hydrogenated and sulfur atoms are subsequently removed by hydrogenolysis. Both pathways occur in parallel employing different active sites of the catalyst surface. The second pathway, however, is much slower than the first and depends on favourable thermodynamic conditions. Recently, Pedernera and co-workers [Ped03, Cho02] found that hydrogenation of aromatics in diesel oils is limited to temperatures above 350°C. Due to steric hindrance, substituted DBTs react preferably via hydrogenation pathway. When diesel sulfur level is lowered to below 100 ppmw, almost all of the remaining sulfur belongs to the DBT group. An important consequence of the described mechanism is that active catalysts for deep HDS reactions are expected to be found among catalysts with a high hydrogenation activity.
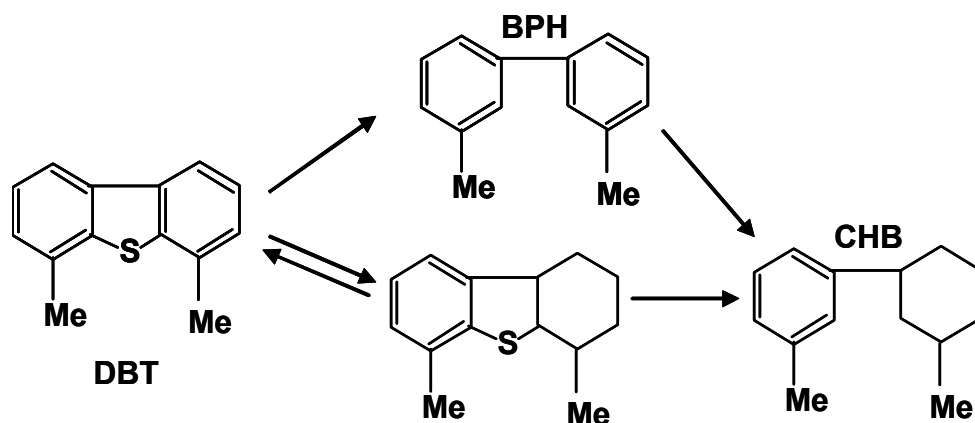

Figure 2.5: Proposed reaction scheme for the HDS of substituted DBT

2.1.3   Hydrotreating catalysts

The type of catalysts used for hydrotreating processes mainly depends on the specific reaction and process requirements. For hydrotreating of feedstocks that contain appreciable concentrations of sulfur and nitrogen, mixed sulfides of CoMo, NiMo or NiW supported on high porous aluminia are used. CoMo catalysts are used for HDS reactions, while NiMo catalysts are preferred for hydrodenitrogenation (HDN) and hydrodearomatization (HDA). Noble metal catalysts, like Pd and Pt, have gained increasing attention due to their high hydrogenation activity. However, their application for deep HDS is limited by their sulfur resistance. Therefore, many companies (IFP, Shell, Criterion, Haldor Topsøe) have developed two-stage processes using noble metal catalysts in a second reactor for aromatic hydrogenation, when most of the sulfur compounds and H_2S have been removed from the process stream leaving the first reactor (see Fig. 2.3a). Information on new

and improved catalysts for deep HDS can be found in some published theses and reviews [Rei99, Cou01, Bab03, Son03, Top05].

Hydrotreating catalysts for industrial use are manufactured in various shapes like sphere, cylinder, trilobe, tetralobe, Raschig ring. Very common are trilobe extrudates with a diameter of 1 mm to 2 mm and a length of about 3 mm to 5 mm. The rates of hydrotreating reactions are often affected by diffusion in the catalyst pores. Therefore, the selection of catalyst particle size and shape as well as of pore structure is important. During operation, deposition of metals and coke at the pore entrance may occur, limiting the diffusion of reactants and products. When the catalyst size is very small, the catalyst bed acts as a granular bed filter capturing fine solid particles. Bed plugging causes an increased pressure drop, especially at the top of the reactor leading to maldistribution of the liquid flow and an increase of operating costs. This problem of pressure drop can be reduced by packing larger particles of catalysts on the top of reactors and small particles towards the bottom.

The activity of hydrotreating catalysts diminishes with time due to the deposition of coke and metals (Ni, V) on the catalyst surface. Both the presence of metals as sulfides on the catalyst surface and their penetration into the pores are responsible for a decrease of the intrinsic reaction rate and the effective diffusion rate. Generally, the deactivation rate of HDS catalysts is high at the first period of their life cycle, while their initial activity is also highest. Next follows a period in which the performance is quite stable. Therefore, results of experiments with new catalysts being at the beginning of cycle are often not comparable with those obtained at a later time. In order to reduce this experimental effect, it is suggested that meaningful measurements should be conducted in the stable regime of a catalyst's life time.

2.1.4   Hydrotreating reactors and scaling problems

Industrial hydrotreating generally employs a large fixed bed reactor. As shown in Fig. 2.6, gas and liquid streams flow cocurrently downward through multiple catalyst beds. Liquid trickles over the catalyst particles by gravity while the remaining gas fills the porous space. Due to the low liquid velocities, maldistribution, channelling and incomplete catalyst wetting occurs, which may lead to hot-spot formation and bypassing in the catalyst bed. Therefore, much attention is currently paid on improvement of the reactor internals such as gas/liquid distributor, quench mixing and redistribution in order to meet potential ultra-low sulfur fuels specifications.
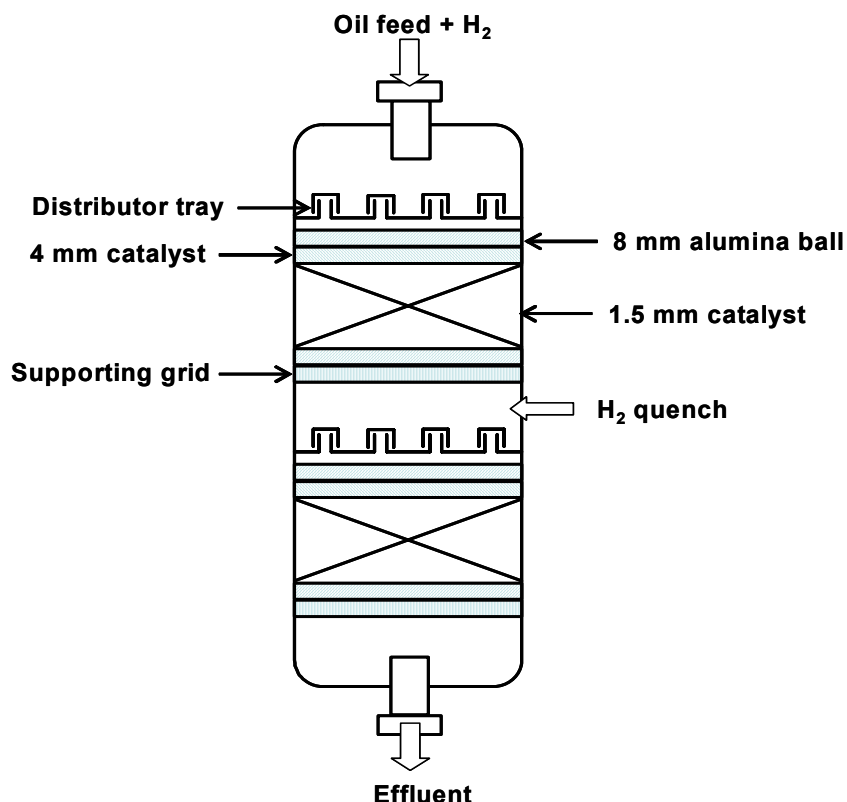
Figure 2.6 : Schematics of an industrial trickle bed reactor

Development of new processes and testing of new catalysts should be made in laboratory scale plants before those being applied in commercial scale. Experiments performing in small scale have some advantages: relatively low installation and equipment costs, smaller consumption of feedstock and process gas such as hydrogen. However, the problem encountered in the down scaling is how to reduce the size of the reactors without detracting from the accuracy and the meaningfulness of the process data which can be obtained from laboratory scale plants. The main limiting factors for downsizing trickle bed reactors are:

1. Most laboratory experiments have been performed under isothermal conditions, whereas the operation of commercial size trickle bed reactors is essentially adiabatic. Moreover, in commercial size units, the major part of the gas phase is the recycle of the hydrogen rich process gas taken from the high pressure separator (see Fig. 2.2). In order to avoid high degrees of complexity the small scale plants are generally operated in a "once through" mode.

2. Since the length of an industrial reactor is much greater than that of a small scale reactor, it is not possible to operate both reactors at the same liquid hourly space velocity (LHSV) and at the same superficial fluid velocities simultaneously. As it is shown in Tab. 2.3, the liquid velocities in small scale reactors are normally much lower than those in commercial ones. These differences in velocities and particle Reynolds numbers (i. e. Reynolds numbers with particle diameter as characteristic dimension) lead to differences in hydrodynamics. This results in a lower conversion in small reactors what has often been observed. How the low fluid velocities influence

hydrodynamic behaviour in the packed bed will be further discussed in the following sections.

	Commercial	Pilot Plant	Bench Scale	Micro flow
Volume (m^3)	100	0.010	0.00015	0.000008
Reduction factor	1	10^4	$7 \cdot 10^5$	$1.3 \cdot 10^7$
Diameter (mm)	2500	120	30	10
Length (mm)	20000	900	200	90
LHSV (m^3/m^3/h)	2	2	2	2
Liquid velocity (mm/s)	11	0.5	0.1	0.05
Particle Reynolds number (Re_L)	55	2.5	0.55	0.25

Table 2.3: Dimensions of typical trickle bed reactors [Sie98c]. $\nu = 3 \times 10^{-7}$ m^2/s, $d_p = 1.5$ mm

Production of ultra low sulfur diesel necessitates an optimum and reliable reactor performance and more severe operating conditions: longer catalytic beds, higher temperatures, a higher partial pressure of hydrogen or longer contact times in the reactors.

2.2   Fluid dynamics and mass transport in 3-phase reactors

The design and the scale-up of trickle bed reactors require not only precise knowledge of the reaction kinetics, but also reliable data of the fluid dynamics in the packed bed as well as for the gas-liquid mass transfer. In practical process development in a small scale plant, however, it is not possible to study both aspects of chemistry (i. e. reaction kinetics) and of physical phenomena (i. e. fluid dynamics and mass transfer) simultaneously. Therefore, the studies of fluid dynamics and of reaction kinetics were decoupled, which is permissible in most cases of trickle flow hydroprocessing of oils [Sie98c]. Following this way, kinetic data of actual feedstocks with commercial catalysts can be determined in a relatively small reactor (e.g. bench-scale units), whereas fluid dynamic characteristics such as liquid and gas hold-ups, pressure drop, heat and mass transport phenomena and residence time distributions are studied on a representative, not necessarily small scale in so-called cold models, as discussed by Sie and Krishna [Sie98a].

The importance of multiphase reactors in petroleum, petrochemical, chemical and other industries attracted many researchers. Several excellent reviews of hydrodynamics and transport phenomena in trickle bed reactors (TBRs) are available [Gia92, Wes92, Sar96, Dud02]. However, in most of the previous literature the packing is treated as a homogeneous system and bulk properties of the flow are considered to prevail everywhere.

In the last decade, some non-invasive measurement techniques such as x-ray, capacitance tomography and magnetic resonance imaging (MRI) [Pet03, Sta06] have been increasingly applied that provide more detailed information on local liquid distribution and flow texture within the packed beds. Understanding of local flow behaviour inside the catalyst beds would improve design and scale-up of TBRs. In the next sections some important factors that characterize the fluid dynamic situation of the 2-phase flow in the packed beds are discussed.

2.2.1 Flow regime

In a trickle-bed, various flow regimes are distinguished, depending on gas and liquid flow rates, fluid properties and packing characteristics. Broadly, flow regimes are classified in high and low interaction regimes, which can be observed for co-current downward flow in packed beds depending on the gas and the liquid flow rates, as qualitatively illustrated in Fig. 2.7 [Gia92].

$$\lambda = \left(\frac{\rho_G \rho_L}{\rho_{air} \rho_W} \right)^{0.5} \qquad \psi = \frac{\sigma_W}{\sigma_L} \left(\frac{\eta_L}{\eta_W} \left(\frac{\rho_W}{\rho_L} \right)^2 \right)^{1/3}$$
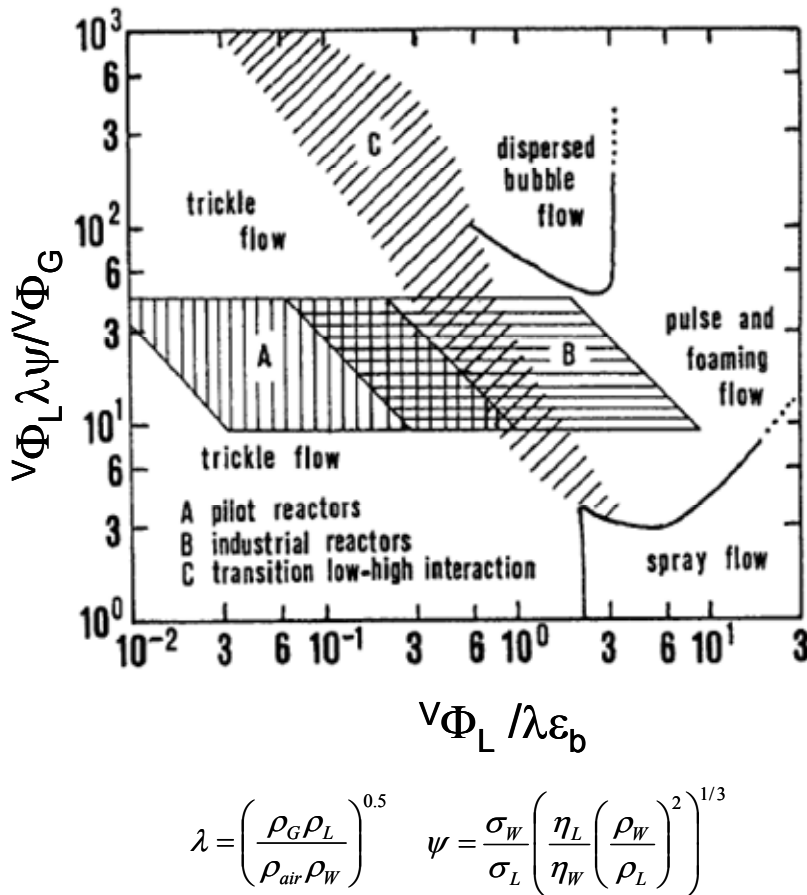
Figure 2.7: Generalized flow pattern diagram for co-current downflow operation [Gia92]

The low interaction regime is also called trickle flow regime, which prevails at relatively low liquid and gas flow rates. The liquid trickles over the packing in the form of a thin film, and the gas phase is the continuous phase filling the void space in the packing. The high interaction flow regimes include three other different flow patterns:

14

pulsing, spray and dispersed bubble. Each flow regime corresponds to a specific gas-liquid interaction thus having a great influence on parameters as liquid holdup, pressure drop and mass and heat transfer rates. For this reason, knowledge of flow regimes in which the reactor will be operated is very important for the design and scale-up purposes.

As shown in the flow map (Fig. 2.7), the transition between low and high interaction regimes is plotted as overlapping areas based on the results of many experimental studies [Gia92]. Since many industrial reactors are operated in the trickle flow regime, or near the transition between the trickle flow and the pulse flow regimes, the prediction of the boundaries between these two flow regimes is of a particular interest. The pulse flow occurs at higher gas and liquid flow rates compared to trickle flow. It is characterized by the passage of liquid-rich bubbly waves called pulses that prevent the flow of gas. Due to the lack of general theory to describe the mechanisms governing the transitions, a convenient method for predicting the transition is to make use of empirical flow map regimes.

Some studies aim at essential process intensification of a trickle-bed reactor by non-steady state operation. This mode of operation can be achieved through either flow variation or interruption [Boe01]. The bed is periodically flushed with liquid, while the gas phase is fed continuously. During the liquid flush, thermal energy and products are removed from the catalyst, while in between flushes, the gaseous reactants can more easily adsorb on the catalyst. The overall rate limiting mass transport of the gaseous reactant to the catalyst is increased. Haure et al. [Hau89] used this concept for the oxidation of SO_2 to sulfuric acid. They reported an increase in oxidation rates up to 50%. However, no study has been reported in the open literature on the translation of laboratory scale reactor unsteady state performance data to large reactors.

2.2.2   Pressure drop and liquid saturation

The basic hydrodynamic parameters for design, scale up and operation of trickle bed reactors are pressure drop and liquid saturation. A pressure drop arises in a trickle bed reactor due to the friction at the gas-liquid interface and represents the dissipated energy. Knowledge of pressure drop is therefore essential for sizing the compression equipment. Moreover, a significant pressure drop may change the partial pressure profiles along the reactor and thereby influence the observed reaction rates. In practice, pressure drop increases gradually during the operation cycle due to the reduction of void space in the catalyst bed caused by the deposition of coke, polymers or corrosion products. If the pressure drop builds up beyond the allowed limits of pumps and compressors feeding the packed bed, then the column must be stopped and the catalytic charge dumped and exchanged with a fresh packing unit.

The amount of liquid held inside the packed beds plays an important role for the reactor performance because the mean residence time of the liquid in the reactor, and hence the conversion achieved, depends on it. Its distribution in the catalyst bed affects significantly the local heat and mass transfer inside the reactor. A quantity which is frequently used in the literature to characterise the liquid phase in packed bed reactors is the total liquid saturation ($\beta_{b,t}$). In general, it consists of two fractions: the internal liquid saturation (β_{int}) and the external liquid saturation (β_{ext} or β_b) (eq. 2.1). The internal liquid saturation (β_{int}) is defined as liquid volume held internally in the pores of the catalyst particles ($V_{L,int}$) per unit of void volumes of the bed without pores' volume ($V_{H,bed}$). This fraction is also called as internal static liquid saturation ($\beta_{b,st,int}$), because the liquid volume remains stagnant in the pores after the gas and liquid flows have stopped. The external liquid saturation β_b is defined as liquid volume held outside the catalyst particles (V_L) per unit of void volume ($V_{H,bed}$) of the bed excluding the pores in catalyst particles in a two-phase flow (eq. 2.1). The external amount of liquid in the reactor bed is further divided into static and dynamic parts. The dynamic liquid saturation ($\beta_{b,d}$) is the freely flowing liquid volume relative to the void volume between catalyst particles, whereas the external static liquid saturation ($\beta_{b,st}$) is the fraction of liquid that is stagnated between catalyst particles (eq. 2.2). The dynamic part depends on two-phase flows, and relies strongly on the operating variables. The static part instead is influenced only by liquid phase physical properties, bed structure and particle sizes. In fact, the total static liquid saturation ($\beta_{b,st,t}$) is the sum of internal and external static liquid saturations (eq. 2.3). For porous particles, besides very exothermic reactions the pores are supposed to be filled entirely with liquid because of capillary force. For non-porous particles, the external liquid saturation, β_b is equivalent to the total liquid saturation, $\beta_{b,t}$. Fig. 2.8 illustrates the distribution of gas and liquid phases in a cross section of a non-porous packing.

$$\beta_{b,t} = \beta_{ext} + \beta_{int} = \beta_b + \beta_{int} = \frac{V_L}{V_{H,bed}} + \frac{V_{L,int}}{V_{H,bed}} \qquad (2.1)$$

$$where: \quad V_{H,bed} = V_G + V_L$$

$$\beta_b = \beta_{b,d} + \beta_{b,st} = \frac{V_{L,d}}{V_{H,bed}} + \frac{V_{L,st}}{V_{H,bed}} \qquad (2.2)$$

$$\beta_{b,st,t} = \beta_{b,st} + \beta_{int} = \frac{V_{L,st}}{V_{H,bed}} + \frac{V_{L,cat}}{V_{H,bed}} \qquad (2.3)$$

Another quantity which is also frequently used in the literature is the liquid holdup (h_b). It is defined as the liquid volume (V_L) present in a unit volume of the reactor (V_0). Thus, the relationship between the liquid holdup and the liquid saturation is given as:

$$h_{b,i} = \frac{V_{L,i}}{V_0} = \frac{\varepsilon_b V_{L,i}}{V_{H,bed}} = \varepsilon_b \beta_{b,i}$$

$$where \quad \varepsilon_b = \frac{V_{H,bed}}{V_0}$$

$$i = st \; (static), \; d \; (dynamic), \; or \; t \; (total)$$

(2.4)

$A_0 d_s \varepsilon_b (1-\beta_{b,ex})$: gas phase

$A_0 d_s \varepsilon_b \beta_{b,ex}$: liquid phase

$A_0 d_s (1-\varepsilon_{b,ex})$: solid phase
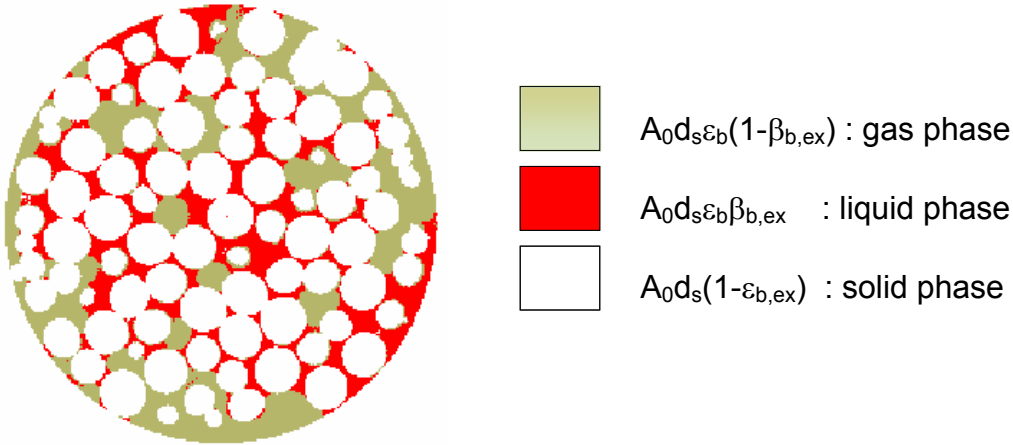
Figure 2.8: Illustration of gas, liquid and solid phases' distribution in a three phase reactor. The image was obtained from a measurement using MRI-technique during two phase flow in a packed bed of glass beads (d_p = 2 mm). Experiment was carried out at atmospheric temperature (T = 25^0C) and pressure (p = 1 atm) with water and air superficial velocity of u_{0L} = 3.88 mm/s, and u_{0G} = 21mm/s, respectively. Slice thickness is d_s = 84 μm.

For fluid dynamics, the external liquid saturation is important. On the one hand it determines the mean liquid phase resident time as discussed above, on the other hand it influences the wetting of the outer surface of catalyst and the pressure drop across the bed. Under steady state operating conditions, the change of fluid dynamic parameters can be explained physically by means of the dissipation energy. The dissipation energy is due to resisting frictional forces at the particle surfaces and driving forces acting on liquid flow. The driving forces consist of the pressure gradient, interaction drag forces and the gravitational force. The pressure gradient depends, besides the bed characteristics, on the velocity and on the density of the flowing fluids. The drag forces result from the particle-fluid interactions as well as the fluid-fluid. Generally, for given gas and liquid velocities, the increase of pressure is equivalent with the increase of gas density which leads to a higher interaction drag force resulting in a higher pressure gradient as well as a reduction of the mean residence time of liquid or a decrease of liquid saturation. The gravitational force depends on the liquid density and is not affected by high pressure. Therefore, the effect of gas on the pressure drop can be split into an effect of the gas velocity and

another due to gas density. With the increase of operating pressure, the operating range in trickle flow regime also increases (see Fig. 2.7).

There have been a large number of studies in the literature devoted to the description of the hydrodynamic and many other aspects of trickle bed reactors. Some excellent reviews in this field [Dud02, Gia92, Wam91] are available. However, in spite of considerable research, a quantitative description of two-phase flow through a packed bed based on fundamental principle has not yet been successfully achieved because of the following difficulties: (i) the complexity of the gas/liquid flow pattern prevailing in trickle bed, (ii) the complexity of the inner geometry of the porous bed, and (iii) the complex interaction between flowing phases and bed properties. Thus, most hydrodynamic models reported in the literature use an empirical approach based on dimensional analysis to produce explicit correlations for estimating liquid saturation and pressure drop. Each empirical correlation has been established on the basis of a data set obtained in a specific range of operating conditions, fluid properties and bed characteristics. They have several parameters for fitting the experimental results. These parameters are not universal constants. Moreover, these correlations have no physical basis and cannot be extrapolated outside the range of experimental data. The predicted values from these empirical models vary considerably.

Another approach for quantifying the hydrodynamic behavior of the multiphase flow is based on the equations of motion and considers determination of drag forces of gas and liquid phases at various operation regimes. Narasimhan et al. (Nar02) have developed a model using the fundamental force balance in an element reactor volume, which is shown schematically in Fig. 2.9. It is assumed that the whole liquid flows as a falling film and the gas phase flows as a continuous phase. In the figure, the interaction force exerted on the gas phase can be divided into two components. The first component F_i is the drag force acting on the gas phase due to the relative motion between gas and liquid phases. The second component F_{pG} is intepreted as gas-particle drag force, which is opposed by an equal and opposite force applied by the particles on the other side of the liquid layer. Similarly, the liquid phase force can also be broken into two components, F_{pG} and F_{pL}. The first component F_{pG} is simply a reaction to the force by which the gas pushes against the particle. The second component represents the force acting on the particles due to the liquid motion. It should be noted that the quantities F_{pG}, F_{pL} and F_i are the drag forces per unit volume of total bed volume. Under steady state, one dimensional flow conditions, the force balance on the gas phase is given by

$$-dp A_G = \rho_G dV_G g + \left(F_{PG} + F_i\right) A_0 dz \qquad (2.5a)$$

Acording to equations 2.1 and 2.2, the relation of the volume of gas phase (V_G) with the external liquid saturation (β_b) is

$$V_G = (1 - \beta_b) V_{H,bed} = \varepsilon_b (1 - \beta_b) V_0 \qquad (2.5b)$$

$$or \quad dV_G = A_G dz = \varepsilon_b (1 - \beta_b) A_0 dz$$

After transforming, equation 2.5a can be written as:

$$-\frac{dp}{dz}\varepsilon_b(1-\beta_b) = \rho_G g \varepsilon_b(1-\beta_b) + F_{PG} + F_i \qquad (2.5c)$$

Similarly, the force balance on the liquid phase yields

$$-dpA_L = \rho_L dV_L g + (F_{PG} - F_i)A_0 dz \qquad (2.6a)$$

or $-\dfrac{dp}{dz}\varepsilon_b\beta_b = \rho_L g \varepsilon_b \beta_b + F_{pL} - F_i$ $\qquad (2.6b)$

where:

$$V_L = \beta_b V_{H,bed} = \varepsilon_b \beta_b V_0$$
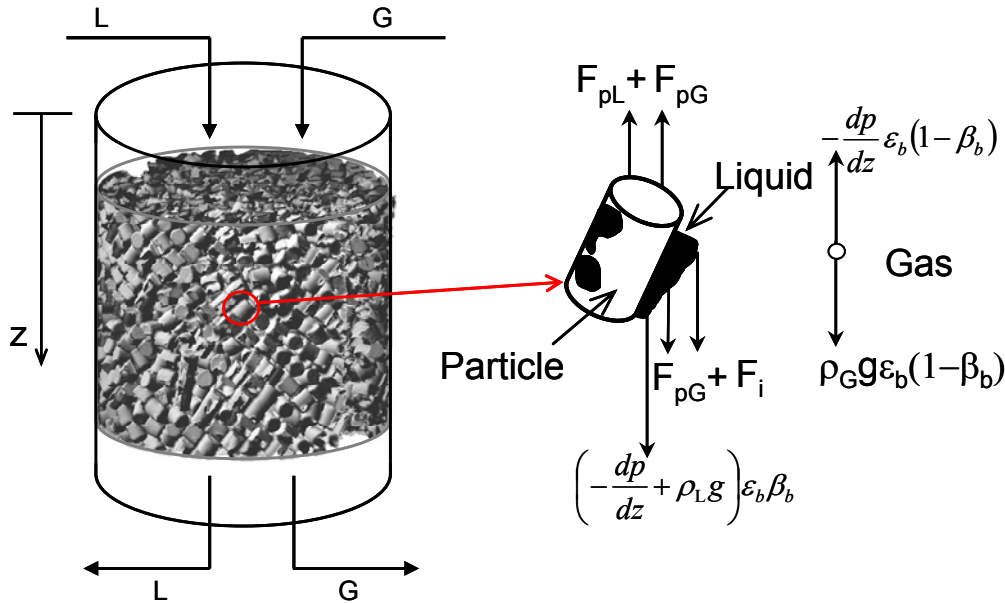$$or \quad dV_L = A_L dz = \varepsilon_b \beta_b A_0 dz$$

Figure 2.9: Schematic representation of acting forces in the three-phase system

The coupling between the equations dictates the relationship between pressure drop and liquid saturation, and it is not necessary to have a separate correlation for each of these hydrodynamic parameters. The key issue for solving these equations is the determination of the drag forces. However, because of the complex fluid dynamics, the drag forces are difficult to describe on the basis of first principles. Therefore, the prediction of two-phase pressure drop and liquid saturation generally is based on empirical correlations and semi-theoretical models. It is noted that no correlation emerges as clearly predominant over others. However, those based on theoretical models seem more reliable than strictly empirical correlations.

2.2.3 Maldistribution and wetting efficiency

The common problem that frequently occurs during the operation of trickle bed reactor is the occurrence of liquid phase maldistribution. This problem becomes more apparent in small scale reactors when gas and liquid velocities are reduced due to scaling down effects. A great deal of effort goes into the design of liquid distributors and redistribution of liquid in quench boxes to minimize maldistribution and achieve uniform flow. Liquid maldistribution may result in two undesirable effects. With no supply of the liquid reactant to the dry parts of the bed, which is generally referred to as incomplete wetting, no liquid phase reaction in these regions occurs and the reactor is not fully utilized. In contrast, if a sufficient amount of liquid is vapourized, reaction may proceed in these unwetted regions. Without the liquid phase removing the reaction heat, however, this may cause hot spots. A basic understanding of the impact of liquid maldistribution on reactor performance is thus essential.

The heterogeneity of the bed structure affects significantly flow distribution inside the packed bed. The wall region of the packings is particularly problematic since the void volume is higher than elsewhere in the reactor. This is why liquid and gas tend to flow towards the reactor wall, which affects the performance of reactors. Wall flow generally varies with ratio of bed diameter to particle diameter (D/d_p). It is recommended that a minimal ratio of about 20 has to be chosen to neglect the influence of wall effects [Sie98c].

Incomplete wetting of particles occurs at low liquid flow rates when the liquid film breaks into rivulets. Wetting efficiency is an important parameter for the design of trickle bed reactors, as it gives an indication of the extent of catalyst utilization. Since the catalyst particles are generally porous, it can be distinguished between the internal (within the catalyst pores) and the external wetting (outer surface of the catalyst particles) efficiency. The pores of the catalyst are generally regarded as completely filled with liquid due to capillary forces and, hence, the value of internal wetting efficiency, η_{ci}, is always one. In contrast, the external wetting efficiency, η_{ce}, which is defined as the fraction of the external area of the catalyst particles effectively wetted by the liquid flowing down the bed, is mostly smaller than 1 and depends on several factors such as bed structure, liquid velocity, gas & liquid viscosities.

The importance of the wetting efficiency results mainly from the fact that it influences the reactor yield or, strictly speaking, the effectiveness factor of the catalyst particles. As shown in Fig. 2.9, the liquid flow around catalyst particle is not uniform, which leads to a non-uniform concentration of the reactants and products at the outer surface of the catalyst. As a result, the concentration profiles inside the pores are non-symmetrical. Conventional catalyst effectiveness factors are therefore not applicable for partially wetted catalyst particles. Several models dealing with the dependence of the effectiveness factor on partial wetting of catalyst particles are proposed in literature [Dud77, Rin89, Bur90].

The apparent reaction rate over incompletely wetted catalytic particles can be smaller or greater than the rate observed on completely wetted packing. This depends on whether the limiting reactant is present only in the liquid phase or in both, gas and liquid phases. Liquid-limited reactions are frequently encountered in high pressure operations, such as occurs in hydrodesulfurization processes, in which the gaseous reactant, H_2, dissolves in the liquid phase in a large excess and the key reactant in the liquid phase has a low vapor pressure. In this case, a decrease in the catalyst-liquid contacting reduces the surface for mass transfer between the liquid and the catalyst causing a decrease in the reaction rate. However, for highly exothermic reactions with a volatile liquid reactant, a gas phase reaction can occur on the dry area of the catalyst and consequently a high reaction rate is observed.

Generally an increase of the fluid velocities and of the gas density causes an increased shear stress at the liquid-gas interface, which improves wetting efficiency by increasing the liquid spreading in the packing. Since liquid velocity in laboratory reactors is much smaller than that in commercial ones, pilot plants are particularly concerned by liquid maldistribution problems. Most correlations and semi-theoretical models for predicting the wetting efficiency based on experimental results are extensively discussed and summarised by Dudukovic et al. [Dud02].

2.2.4 Axial dispersion

The evaluation of kinetic data from fixed bed catalytic reactors is usually based on the assumption of "plug" flow, that is, all reactants existing in a phase have the same velocity. Consequently, at steady state all reactants have the same residence time which is given by

$$\tau_{phase,i} = \frac{V_{phase,i}}{V \Phi_{phase,i}}$$ (2.7)

However, relevant deviations from plug flow can occur in short bed experimental reactors due to the higher influence of inevitable axial dispersion. Because velocity distribution in the catalyst bed is not uniform, there is no unique residence time for all reactants but a residence time distribution (RTD) exists. In this case equation 2.4 represents the mean residence time.

The phenomenon of deviations from ideal plug flow is commonly called back mixing. This term summarizes numerous effects like fluid maldistribution, wall effects, convective mixing due to turbulences and eddies and molecular diffusion. A parameter to evaluate the back mixing on a marcroscale is the effective axial dispersion coefficient D_{ax} usually determined by residence time distribution (RTD) experiments. In these experiments an inert tracer is injected in the feed stream and its occurence in the effluent is measured over time.

The degree of back mixing is often characterized by the dimensionless Peclet number,

$$Pe = \frac{u_L \cdot L}{D_{ax}}$$
(2.8)

which is based on the catalytic bed length L. Another dimensionless number based on the characteristic particle diameter is often called the Bodenstein number as described in the following relation:

$$Bo = \frac{u_L \cdot d_p}{D_{ax}}$$
(2.9)

Principally the back mixing occurs in both liquid and gas phases. However, deviations from plug flow in the gas phase are generally not of interest [Fro90]. A criterion for adequate performance of trickle bed reactors has been proposed by Mears [Mea71] on the basis of the assumption that the actual reactor should not contain more than 5% extra catalyst to achieve the same conversion as an ideal reactor. This criterion is given by eq. 2.10, where n is the reaction order and X is the conversion.

$$Pe > 20n \ln\left(\frac{1}{1-X}\right)$$
(2.10)

Gierman [Gie88] refined this criterion and concluded, based on his practical experience, that this could be relaxed by using a factor of 8 instead of the factor 20.

2.2.5 Mass transfer

The hydrotreating reactions in a trickle bed reactor always involve both transport and chemical reaction processes, since reaction species must be transported to and removed from the surface site, where the chemical reaction takes place. The overall conversion rate can be controlled in the following steps: (a) mass transfer of reactants and/or products between the bulk gas phase and the liquid-gas interface, (b) mass transfer through the liquid film surrounding the catalyst particles, (c) diffusion within the liquid filled catalyst pores, and (d) intrinsic kinetics of reaction at the catalyst surface. Determination of the rate-limiting steps plays an important role for the design. If the gas-liquid or the liquid-solid mass transfer rates are low compared to the intrinsic reaction rate, the fluid dynamic behaviour largely dominates the conversion achievable in a trickle bed reactor.

Fig. 2.10 shows schematically the transport of molecules from the gas phase to the active surface of a spherical catalyst in trickle bed reactors.
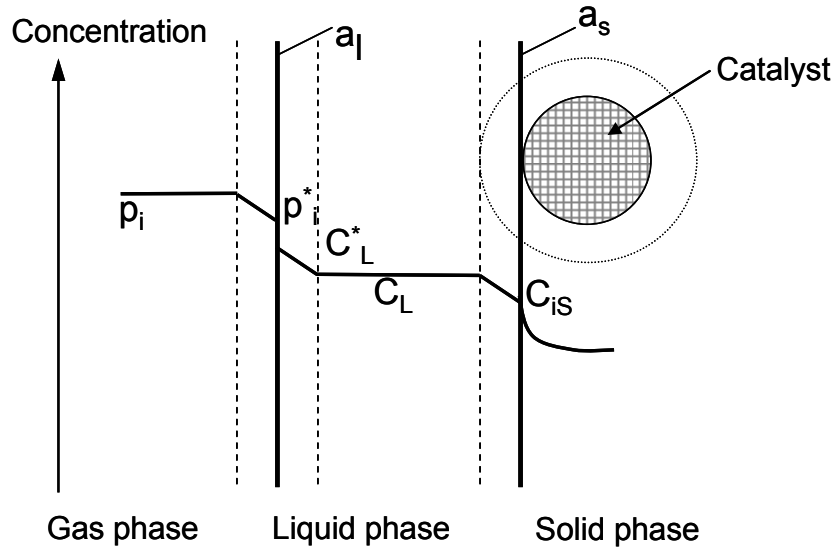
Figure 2.10: Concentration profile for mass transfer and reaction in series in a 3-phase system

For the case of hydrotreating reactions, the relative magnitude of various mass transfer resistances can be estimated as follows [Sie98c]:

- Resistance from bulk gas to gas-liquid interface   Negligible

- Resistance from gas-liquid interface to bulk liquid   2 %

- Resistance from bulk liquid to external catalyst surface   21 %

- Resistance due to intraparticle diffusion and reaction   77%

If first-order kinetics are assumed and the overall reaction rate as well as the mass transfer at any point in the reactor is at steady state, then, the mass balance of the reactor is as follows:

$$d^{n}\Phi = k_{G}a_{I}\left(C_{G} - C_{G}^{*}\right)dV = k_{L}a_{I}\left(C_{L}^{*} - C_{L}\right)dV = k_{S}a_{S}(C_{L} - C_{iS})dV = \eta k_{r}\rho_{b}C_{iS}dV \quad (2.11)$$

In equation 2.11, the parameter a_I is defined as the specific gas-liquid surface area (m^{-1}) and a_S as the specific catalyst particle area (m^{-1}), both per unit volume of reactor. k_G is the gas phase mass transfer coefficient for the transfer from gas to liquid, and k_L and k_S are the liquid phase mass transfer coefficient for the tranfers from gas to liquid and liquid to solid, respectively (all with the dimension m/s). k_r is the surface reaction rate constant, C_{iS} is the concentration at catalyst particle external surface and η is the overall effectiveness factor. At the gas-liquid interface the assumed equilibrium can be expressed as a Henry's law constant:

$$H = \frac{C_{G}^{*}}{C_{L}^{*}} \quad (2.12)$$

Combining equations (2.11) and (2.12) and eliminating the unknown concentrations C_{G}^{*}, C_{L}^{*}, C_L and C_{iS} results in:

$$d^n\Phi = \frac{\dfrac{C_G}{H}}{\dfrac{1}{Hk_Ga_I} + \dfrac{1}{k_La_I} + \dfrac{1}{k_Sa_S} + \dfrac{1}{\rho_b\eta k_r}} dV \qquad (2.13)$$

The conversion rate appears to depend on four resistants in series: the gas phase transfer resistance, two liquid phase transfer resistances, and the kinetic resistance. The highest resistance limits the conversion rate. Herein the global mass transfer coefficient K is defined as:

$$\frac{1}{K} = \frac{1}{Hk_Ga_I} + \frac{1}{k_La_I} + \frac{1}{k_Sa_S} + \frac{1}{\rho_b\eta k_r} \qquad (2.14)$$

As discussed above, the resistance in the gas film is negligible in most cases of hydrotreating operations. Therefore, the global mass transfer coefficient may be approximated as:

$$\frac{1}{K} \approx \frac{1}{k_La_I} + \frac{1}{k_Sa_S} + \frac{1}{\rho_b\eta k_r} \qquad (2.15)$$

The mass transfer coefficients, k_L, and k_S depend on a number of variables, such as type of packing, flow rates, wetting of particles, and geometry of the column. Several differing correlations for predicting these coefficients in trickle bed reactors over the past 40 years have been proposed. An overview of the available relations is given in [Dud02]. Among these correlations, the most general ones that can be recommended for design purposes appear to be those of Larachi et. al. [Lar03], which have been validated over broad ranges of experimental data.

2.3   Hydrotreating modelling

For scaling up purposes and for evaluating the experimental results from small scale plants, various models for the analysis and the design of trickle bed reactors have been developed. Most of the models reported in the literature can be classified in two categories: the pseudo-homogeneous and the heterogeneous models. The former considers the bed as a pseudo-continuum, while the later distinguishes between temperatures and concentrations in the bulk gas phase and those inside or at the surface of the catalyst.

The pseudo-homogeneous models have been widely used because of their convenient mathematical form. In order to simplify the model, the following assumptions are made: plug flow; absence of external mass transfer limitations, thermal gradients and stagnant zones; complete particle wetting. Furthermore, it is assumed that the reaction occurs only at the liquid catalyst interface and with no evaporation or condensation. For plug flow conditions a mass balance of sulfur compounds in the liquid phase can be written in partial differential form:

$$^V\Phi_L dC_{XS} = r_{XS}\rho_b dV \tag{2.16}$$

A power law kinetics is considered which accounts for the summed up concentration of the sulfur compounds, C_{XS}, and the partial pressure of hydrogen, p_G, at reaction condition.

$$r_{XS} = -kC_{XS}^{n1}p_G^{n2} \tag{2.17}$$

Substituting r_{XS} in (2.16) by equation (2.17) and integrating from the initial condition of $C_{XS} = C_{XS,0}$ over the whole reactor with the assumptions of constant partial pressure of hydrogen and that $n1 \neq 1$ yields:

$$\frac{C_{XS,0}^{1-n1}}{n_1 - 1}\left[(1 - X_{XS})^{1-n1} - 1\right] = \frac{3600}{LHSV} \cdot k\rho_b p_G^{n2} \tag{2.18}$$

For deep hydrodesulfurization reaction performing at severe operating conditions, however, homogeneous models with their simplified assumptions may lead to inaccurate predictions. Several multiphase models, therefore, have been developed to overcome the shortcomings of the pseudo-homogeneous models. A general heterogeneous model contains the mass-, heat- and momentum balances of gas, liquid and solid phases. These balances are linked by transport terms. Some models of this kind account for the effect of partial wetting and transport of the gaseous reactant to dry external areas of the catalyst. Others consider evaporation effects by adding vapour-liquid equilibrium calculations and flash units to mass balance equations. There are two different approaches for phase equilibria calculations. One involves measurements of bulk properties employing equation of states considering the phases as single compounds. The other one is based on continuous thermodynamics, which is rarely used in real systems such as distillation petroleum. In addition, some models account for liquid flow non-uniformity and maldistribution by using an axial dispersion model. Furthermore, most of models use mathematical expressions for HDS-reaction rate described with the help of kinetic equations of the Langmuir-Hinshelwood type, which accounts for the concentrations of sulfur compounds, hydrogen and hydrogen sulfide. It is noted that the modelling of the removal of the refractory sulfur compounds for deep HDS is more complex since there are two parallel routes (direct and hydrogenation) as discussed in section 2.1.2.

3 MRI-method in chemical engineering

In this study magnetic resonance imaging (MRI) was used to investigate the fluid dynamic behaviour of multiphase flow in trickle beds. Therefore, some knowledge about MRI and the data produced by MRI scanners is necessary. This chapter describes briefly the application of this technique in chemical engineering and introduces its basic principles. A detailed review of the physics of MRI falls outside the scope of this manuscript. A complete description on this topic is found in comprehensive books of the authors Blümich [Blu00], Kimmich [Kim97] and Callaghan [Cal91]. The basics and practical aspects of MRI applied in chemical engineering is recently reviewed in [Har06].

Nuclear Magnetic Resonance (NMR) method, in particular Magnetic Resonance Imaging (MRI) has been increasingly used in chemical and process engineering. A number of researchers have developed various MRI experimental techniques to investigate different aspects of the fluid distribution and flow in porous systems. Recent advances in this field are reported in a comprehensive book [Sta05]. In Germany, a research group at the Universität Karlsruhe (TH) focused on the use of MRI to gain better understanding of structure, mass transport processes and multiphase flow behaviour in porous media. The major advantages of this technique are their ability to visualize the internal structure of optically opaque systems in three dimensions without interfering with the multiphase flow. There are also various non-invasive techniques such as capacitance tomography [Rei98], X-ray tomography [Toy96], optical methods [Gie88], which are used to characterise the hydrodynamic behaviour of two-phase flow within trickle bed reactors. Some of these techniques offer faster data acquisition than MRI. In contrast, MRI has the potential for relatively high spatial resolutions of 20 μm – 300 μm, which allows to distinguish between gas, liquid and solid phases in the packed beds. Another interesting combination is MRI and NMR spectroscopy. Koptyug et al. [Kop04] have employed these techniques to visualize the interaction of mass and heat transport processes and a chemical reaction at elevated temperatures.

The physical basis of Nuclear Magnetic Resonance (NMR) is the quantum-mechanical angular momentum and magnetic dipole moment of NMR-active atomic nuclei. An atom consists of three basic particles, namely protons, neutrons and electrons. If an atom has an even number of both protons and neutrons, then the angular momentum is zero. If an atom has an uneven number of neutrons or protons, then the atom has a certain angular momentum. The angular momentum is expressed as a vector quantity having both magnitude and direction. The magnetic dipole moment is also a vector quantity having both magnitude and direction and is oriented in the same direction as the angular momentum I.

$$M = \gamma I \tag{3.1}$$

Where γ is known as the gyromagnetic ratio, and is specific to each magnetically active nucleus. There are some nuclei, which are magnetically active, such as: ^1H, ^{13}C, ^{19}F, ^{31}P, ^{23}Na.
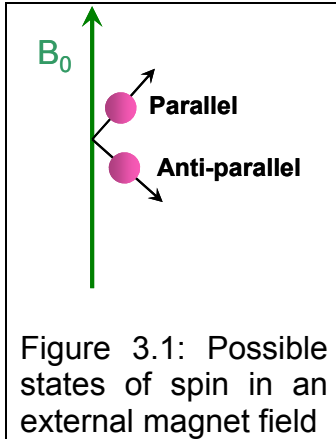

Figure 3.1: Possible states of spin in an external magnet field

Of all stable isotopes, the nucleus of the hydrogen atom, ^1H, has the largest γ. Furthermore, it is abundant in the nature and is contained in all organic matter, and especially in water. That is the reason why it is widely used in NMR experiments. Because of the quantum-mechanical spin characteristics of the proton, if it is placed in an external magnetic field, two different states exist. The z component of the spin is either parallel or anti-parallel to B_0. The magnitude of the spin is equal in both states. According to the uncertainty principle, the transverse component of the spin can not be determined. Quantum-mechanical superpositions of both states precess around the axis of the external B_0 (Fig. 3.2) at the precessional resonance frequency, ω_0, which is given by the Larmor's equation 3.2.

$$\omega_0 = \gamma B_0 \tag{3.2}$$
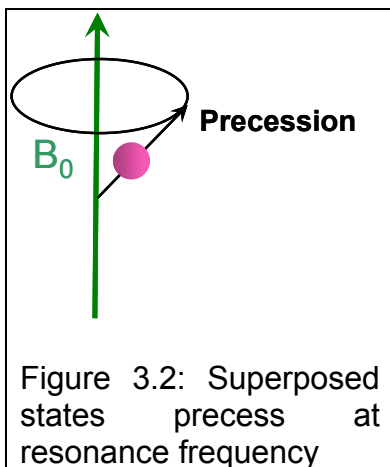
Figure 3.2: Superposed states precess at resonance frequency

The precessional frequency is proportional to the external static magnetic field, B_0. Increasing B_0 will increase the precessional frequency and conversely, decreasing B_0 will decrease the precessional frequency. This is analogous to a spinning top. It will precess due to the force of gravity. If the gravity were to be decreased (as it is on the moon), then the top would precess slower.

When many protons, like for a sample to be imaged, are placed in a strong, uniform static magnetic field B_0, some of them align anti-parallel and a slight majority aligns parallel. Spins aligned in the parallel orientation are called to be in a low energy state while spins in the antiparallel orientation are at a high-energy state (Fig. 3.3). The energy difference between the high and the low energy states is proportional to the strength of the externally applied magnetic field, B_0. Also the number of spins in the low energy state is related to the strength of B_0. The higher the B_0, the greater the number of spins aligned in the low-energy state.

The number of spins in the low energy state in excess of the number in the high-energy state is referred to as the spin excess. The magnetic moments of these excess spins add to form the net magnetization and thus the sample placed in the magnetic field becomes magnetized. The net magnetization, M_0, at thermal

equilibrium is also represented as a vector quantity which is given by the Curie law for nuclear paramagnetism (eq. 3.3). According to thermodynamics, the average number of excess spins is given by the Boltzmann distribution, resulting in

$$M_0 = N \frac{\gamma^2 \hbar^2 I(I-1)}{3k_B T} B_0 \qquad (3.3)$$

The parameters have the following meanings: I is the nuclear spin quantum number, γ is the gyromagnetic ratio specific for a given isotope (see eqs. 3.1 & 3.2), $\hbar$ is Planck's constant, k_B is Boltzmann's constant, N is the number of nuclei and T is the temperature.

If a sample is inserted in a magnetic field of strength of 10 Tesla at room temperature (T = 298 K), there is a tiny fraction of about 0.007% in population of the ^{1}H nuclei aligned with the field.

Figure 3.3: Schematic representation of two different energy states of spins.
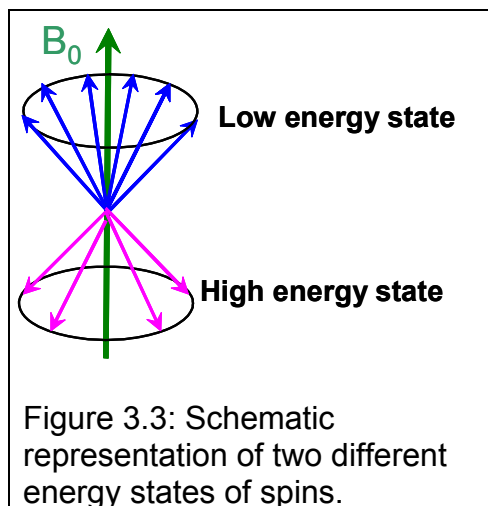
The essential consequence resulting from eq. 3.3 is that the magnetization increases linearly with the number of nuclei and the magnetic field and with the square of the gyromagnetic ratio γ. M_0 is the quantity which after all translates into the measured NMR signal. So it should be as large as possible. In order to obtain maximum magnetization a very strong magnetic field is used and nuclei with a large γ are chosen. As discussed above, ^{1}H nuclei have the largest γ (2.675 10^8 rad s^{-1} T^{-1}) and exist abundantly in nature as compared to other nuclei. Therefore, they are commonly used in MRI experiments.

Once the sample has become magnetized, that means the spins are in either the high or low energy state, a condition is reached known as thermal equilibrium. It should be noted that at equilibrium, the individual spins creating the net magnetization do not precess in phase. The MR signal, however, is not measured at this equilibrium state, but it is measured with the response of the non-equilibrium transverse magnetization which is induced in a receiver coil enclosing the sample. In any MR experiment, an electromagnetic radio frequency (rf) is applied perpendicular to B_0 at the resonance (Larmor) frequency into the sample, then individual spins begin to precess in phase and create a net magnetization vector to tilt away from B_0. As the rf pulse continues, some of the spins in the lower energy state absorb energy from the rf field and make a transition into the higher energy state. This has the effect of "tipping" the net magnetization toward the transverse plane. For the purpose of this explanation, it is assumed that sufficient energy is applied to produce a 90-degree flip of the net magnetization. In such an example, it is said that a 90-degree flip angle, or a 90-degree pulse has been applied (Fig. 3.4). The rf field is also referred to as B_1.
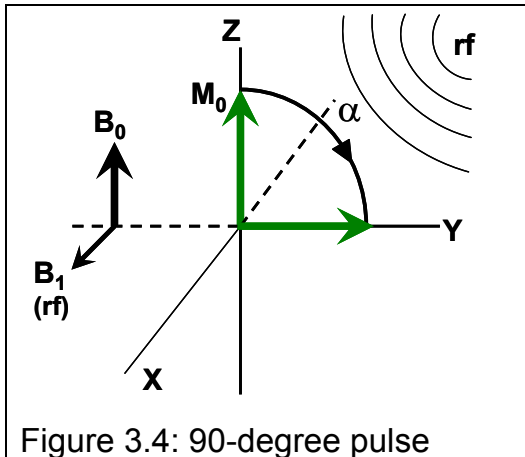
Figure 3.4: 90-degree pulse

The receiver coil is oriented perpendicular to B_0. As the magnetization (now referred to as transverse magnetization, or M_{xy}) precesses through the receiver coil, a current or signal is induced in the coil. The principle behind this signal induction is Faraday's law of induction. This states that if a magnetic field is moved through a conductor, a current will be produced in the conductor.
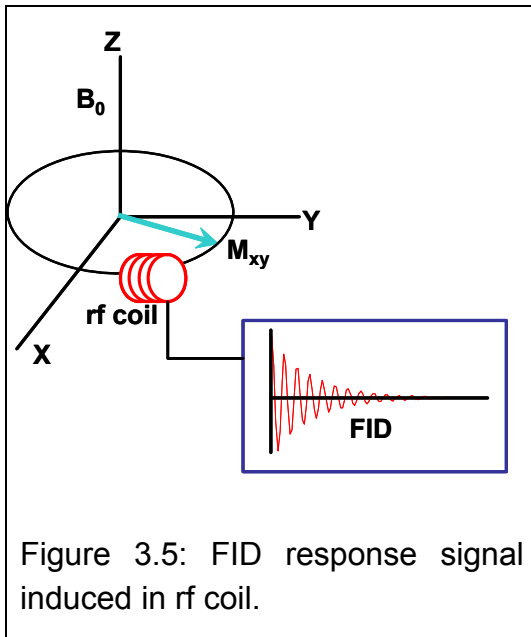

Figure 3.5: FID response signal induced in rf coil.

In order to detect the signal produced in the coil, the transmitter must be turned off. When the rf pulse is discontinued, the nuclei realign themselves such that their net magnetic moment M is again parallel with B_0. This return to thermal equilibrium is referred to as *relaxation*. During relaxation, the nuclei lose energy by emitting their own rf signal. This signal is referred to as the *free-induction decay* (FID) response signal. The FID response signal is measured by a conductive field coil placed around the object being imaged (Fig. 3.5). The time-dependence of M in the magnetic field, describing this precession motion, follows the essential equation:

$$\frac{dM}{dt} = \gamma \, M(t) \times B(t)$$

(3.4)

It is noted that the time dependence of the magnetization vector M(t) is related to the crossproduct of M and B. Its solution is a precession of M around B.

The relaxation process yields information not only about the magnitude of the magnetization vector, but also about the physicochemical environment of the spin system under study. The recovery of the longitudinal component of the magnetization, M_z, to its equilibrium value M_0 is known as longitudinal relaxation. During this relaxation process, the excited spins can only relax by transferring the excess energy to its surroundings, often referred as the lattice. Therefore, this relaxation process is also called spin-lattice relaxation. The time constant to describe this relaxation process is called spin-lattice (or longitudinal) relaxation time T_1. For homogeneous systems, the rate of equilibration is often described by

$$\frac{dM_z}{dt} = -\frac{M_z - M_0}{T_1}$$

(3.5)

29

The solution of this equation (with initial condition $M_z(t=0) = 0$) is an exponential function as given by

$$M_z(t) = M_0 \left[1 - e^{-t/T_1}\right] \qquad (3.6)$$

The time constant which describes the return to equilibrium of the transverse magnetization, M_{XY}, is called the spin-spin relaxation time, T_2:

$$\frac{dM_{xy}}{dt} = -\frac{M_{xy}}{T_2} \Rightarrow M_{xy} = M_{xy,0} e^{-\frac{t}{T_2}} \qquad (3.7)$$

T_2 is always less than or equal to T_1. Two factors contribute to the decay of transverse magnetization:

1) Molecular interactions lead to a *pure T_2 molecular effect*.

2) Variations in B_o or in local susceptibility lead to an *inhomogeneous T_2* effect. The combination of these two factors is what actually results in the decay of transverse magnetization. The combined tranverse relaxation time constant is often given the symbol T_2*.

When MR images are acquired, the rf pulse B_1 is repeated at a predetermined rate. The period of the rf pulse sequence is the *repetition time*, TR. The FID response signals can be refocused and measured at various times within the TR interval. The time between which the rf pulse is applied and the response signal is measured is the *echo delay time*, TE. By adjusting TR and TE the acquired MR image can be made to contrast different types of material in one sample system.

To produce a 3D image, the FID resonance signal must be encoded for each dimension (eq. 3.9). As example, encoding in the axial direction, the direction of B_0, is accomplished by adding a gradient magnetic field to B_0. This gradient causes the Larmor frequency to change linearly in axial direction. Thus, an axial slice can be selected by choosing the frequency of a narrow-banded B_1 pulse to correspond to the Larmor frequency of that slice. The 2D spatial reconstruction in each axial slice can be accomplished using frequency and phase encoding. A ''preparation'' gradient, G_y, is applied causing the resonant frequencies of the nuclei to vary according to their position in the y-direction. G_y is then removed and another gradient, G_x, is applied perpendicular to G_y during data acquisition. As a result, the resonant frequencies of the nuclei vary in the x-direction due to G_x and have a phase variation in the y-direction due to the previously applied G_y. Thus, x-direction is encoded by frequency and y-direction samples by phase.

The gradients correlate the Larmor precessing frequencies with spatial coordinates given by eq. 3.8; whereas the signal intensity is proportional to the amount of active material (e. g. protons) and function of relaxation times (T_1, T_2, or T_2*).

$$\omega(r) = \gamma(B_0 + G\,r) \qquad (3.8)$$

where G is the vector of magnetic field gradient given by equation 3.9 and r is the position vector of the spins in the sample.

$$G = \left(\frac{\partial B}{\partial x}, \frac{\partial B}{\partial y}, \frac{\partial B}{\partial z} \right) = \left(G_x, G_y, G_z \right) \qquad (3.9)$$

If the spins at position r have a local density $\rho(r)$, then the transverse magnetization expressed as a complex number dS obtained from an elemental volume dV with a time-independent gradient, is given by

$$dS(G,t) = \rho(r) \exp[i\gamma t(B_0 + Gr)]dV \qquad (3.10)$$

In the case of pulsed rf excitation, Fourier Transform is needed for extracting the frequency and intensity information, resulting in the so-called MR signals. These signals are turned into digital images, which characterize the signal from each "voxel" (volume element) of the image.
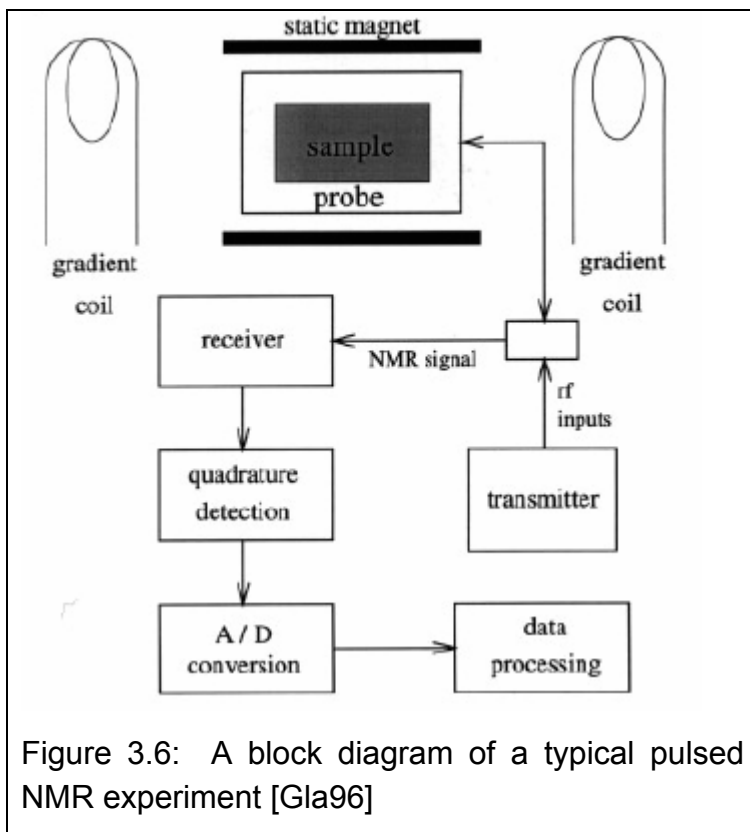
Figure 3.6: A block diagram of a typical pulsed NMR experiment [Gla96]

The major devices of a MRI system are illustrated in Fig. 3.6. The most expensive of the imaging system is the static magnet. Most magnets are of the superconducting type. It is made of superconducting wire which has an electrical resistance close to zero when it is cooled close down to 4 K by immersion in liquid helium. Once current flows in the coil, it will continue to flow as long as the coil is kept at liquid helium temperature. The field strength of the magnets is normally greater than 1 Tesla (i.e. 20000 greater than the earth's magnet field). In contrary to the magnet, the gradient coils function at room temperature. For an axial gradient, e. g. currents in two coils flow in opposite directions creating a magnetic field gradient between the two coils. The B field at one coil adds to the B_0 field while the B field at the center of the other coil subtracts from the B_0 field. The rf transmitter creates the B_1 field which rotates the net magnetization in a pulse sequence.

4 Scope of this study (Methodology)

As explained in chapter 1, the purpose of this study is to determine the influence of hydrodynamics on the lowering of the overall hydrodesulfurization reaction rates in bench scale reactors. Fig. 4.1 outlines a scheme of the present work which consists of experimental investigations and a mathematical model that predicts the HDS performance by accounting for the important fluid dynamic non-idealities and for mass transfer phenomena. As already mentioned in chapter 2.2, the experiments dedicated to fluid dynamics can be separated from those for studying the HDS reaction. This leads to a reduction of complexity and investment because conversions of HDS reaction at high temperature and pressure conditions can be studied in relatively small reactor systems whereas fluid dynamics are typically studied on a representative, not necessarily small scale at relaxed operating conditions.
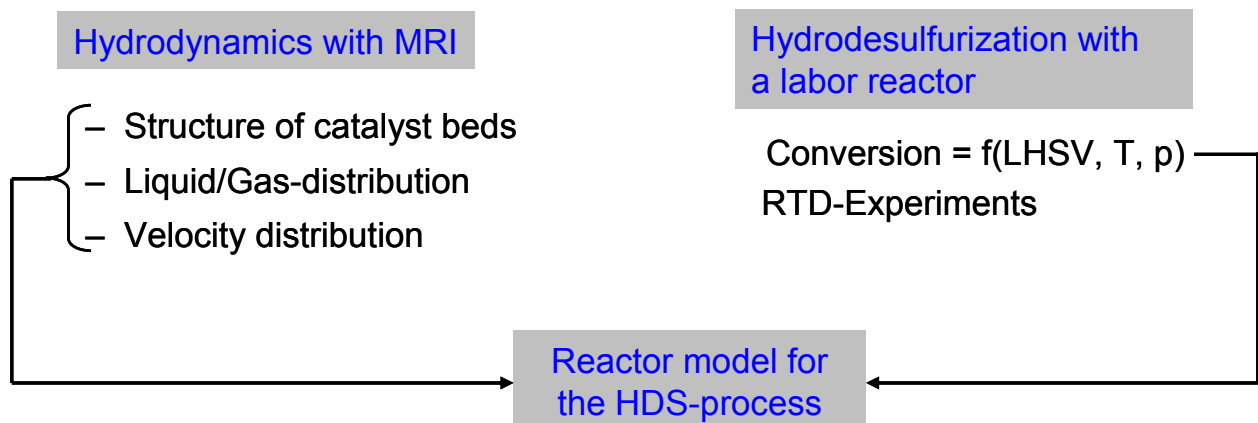
Figure 4.1: Schematic procedure of this study.

Following this approach, the experimental investigations can be divided into three parts. The first part of the work is so-called "cold flow" experiments. The objective of these experiments is to understand the effects of particle geometry and physical properties of the working fluids on flow texture and gas/liquid distribution in the packed beds with the use of MRI as a non-invasive technique. The major advantage of using MRI is that it has a sufficient spatial resolution to identify the spatial heterogeneity and the liquid distribution inside the packed bed at the micro or particle level. The local properties importantly influence the fluid dynamic behaviour of the process which are crucial for understanding the macroscopic or bed scale behaviour of the reactor. As reactor temperature and pressure will affect the fluid dynamics, efforts were made to perform measurements at elevated temperatures and pressures with real feed stock (e. g. diesel). To see the influence of the operating conditions and to allow for comparison with data from literature, measurements were also carried out under atmospheric condition with real feed stock and with different gas/liquid systems.

In order to combine the results of MRI-measurements with the data obtained from HDS experiments in a bench scale plant it is necessary to construct an apparatus having the same geometry (i.e. inner diameter and length) as the reactor used in catalytic experiments. Likewise, the packing was charged with trilobe particles, which have identically the form of catalyst particles used in HDS experiments. However, they are applied without the active metals Ni and Mo on the alumina catalyst support, because these metals have paramagnetic property and cause distortion of magnetic field in the MRI-system.

The second part of the work is to measure the dispersion of the liquid phase in a trickle bed reactor without chemical reaction. As explained in chapter 2.3.1, the axial dispersion in trickle bed reactors comprises two mechanisms: (1) convective dispersion within the packing due to wall effects and flow non-uniformities, (2) diffusive dispersion arising from molecular diffusion within the liquid phase. In most practical situations, the first mechanism is dominant. In this study, the axial dispersion was examined by means of residence time distribution (RTD) experiments. The pulse method with squalane as the tracer substance was used to measure the resident time distribution. Experiments were carried out in a bench scale reactor at high temperatures and pressures in order to determine the influence of the axial dispersion on the reactor performance at operating conditions.

The third part of the experimental study aims at determining the conversion for the HDS reaction at the same bench scale plant used for RTD-measurements. The experimental conditions were kept similar to those applied in industrial hydrotreating processes regarding temperature, pressure and contact time. A commercial Ni/Mo-γAl_2O_3 catalyst (Criterion 424) was used in this study. As mentioned above, the reactor was filled with trilobe catalyst pellets of the same size and by the same procedure used in MRI-experiment.

The experimental results obtained from MRI, RTD and HDS measurements were then integrated in a multiphase reactor model. The objective was a simulation program that predicts the HDS performance accounting for the fluid dynamics and mass transfer phenomena. The differential mass balances of the reactants H_2, H_2S and S-compounds are based on the two-film theory [Kor96]. The model includes the mathematical expression for the HDS reaction rate of the Langmuir-Hinshelwood type to take into account the inhibition of H_2S as reported in a previous study by Pedernera [Ped03]. This process simulation is therefore capable of predicting the process condition effects on sulphur removal in laboratory reactor and can therefore be used for scale-up purposes.

5 Experimental methods

In the following, the experimental methods are introduced for the three experimental parts of this work and the corresponding calculation procedures are introduced.

5.1 MRI-experiment

5.1.1 Experimental plant

A scheme of the experimental setup is illustrated in Fig. 5.1. All MRI-experiments were performed by using a Bruker Avance 200 NMR Spectrometer. The vertically arranged superconducting magnet generates a magnetic field of 4.7 T in a room-temperature bore of 150 mm. Spatial resolution was achieved with a Bruker mini 0.36 gradient system producing gradients of up to 0.14 T/m in three orthogonal directions, respectively. As antenna, an open-ended Bruker bird-cage probe head with 64 mm inner diameter was used. Standard RARE and MSME pulse sequences as delivered by Bruker were employed for the acquisition of three-dimensional (3D) and two-dimensional (2D)-multislice spin-density images of the liquid in the bed. From the 3D-images liquid saturation and wetting efficiency in fixed beds during the two-phase flow were retrieved. A detailed description of employed sequences can be found with Blümich [Blu00] and Callaghan [Cal91].

A special apparatus, which consists of a double wall tube, was placed in the center of the NMR spectrometer. The material used for construction of this apparatus is polyphenylene sulphide (PPS). The inner tube having a diameter of 19 mm contains a packed bed of spherical glass beads (d_p = 2 mm) or of porous Al_2O_3 trilobes (d_p = 2 mm). In the annular gap, a temperature controlled solution of perfluorinated polyether was circulated to keep the temperature of the packed bed constant during the experiment. The advantage of using perfluorinated polyether is that its molecule has no proton, and thus cannot contribute signals and cannot cause interference with signals from the packed bed during the MRI-measurements. Liquid feed was pumped by a metering pump and mixed with gas. After passing the preheating zone, both streams flowed cocurrently through the packed bed. The gas flow rate was controlled by a flow meter. After leaving the packed bed, the gas/liquid mixture was separated in a high pressure separator. The operating conditions ranged in temperature from 20°C to 150°C and in pressure from 1 bar to 20 bars. Pressure drop across the packed bed was measured with a pressure difference transmitter. Water, diesel oil and polyethylene glycol were used together with nitrogen, hydrogen and compressed air. Prior to the experimental runs, the packings were prewetted by soaking with liquid.
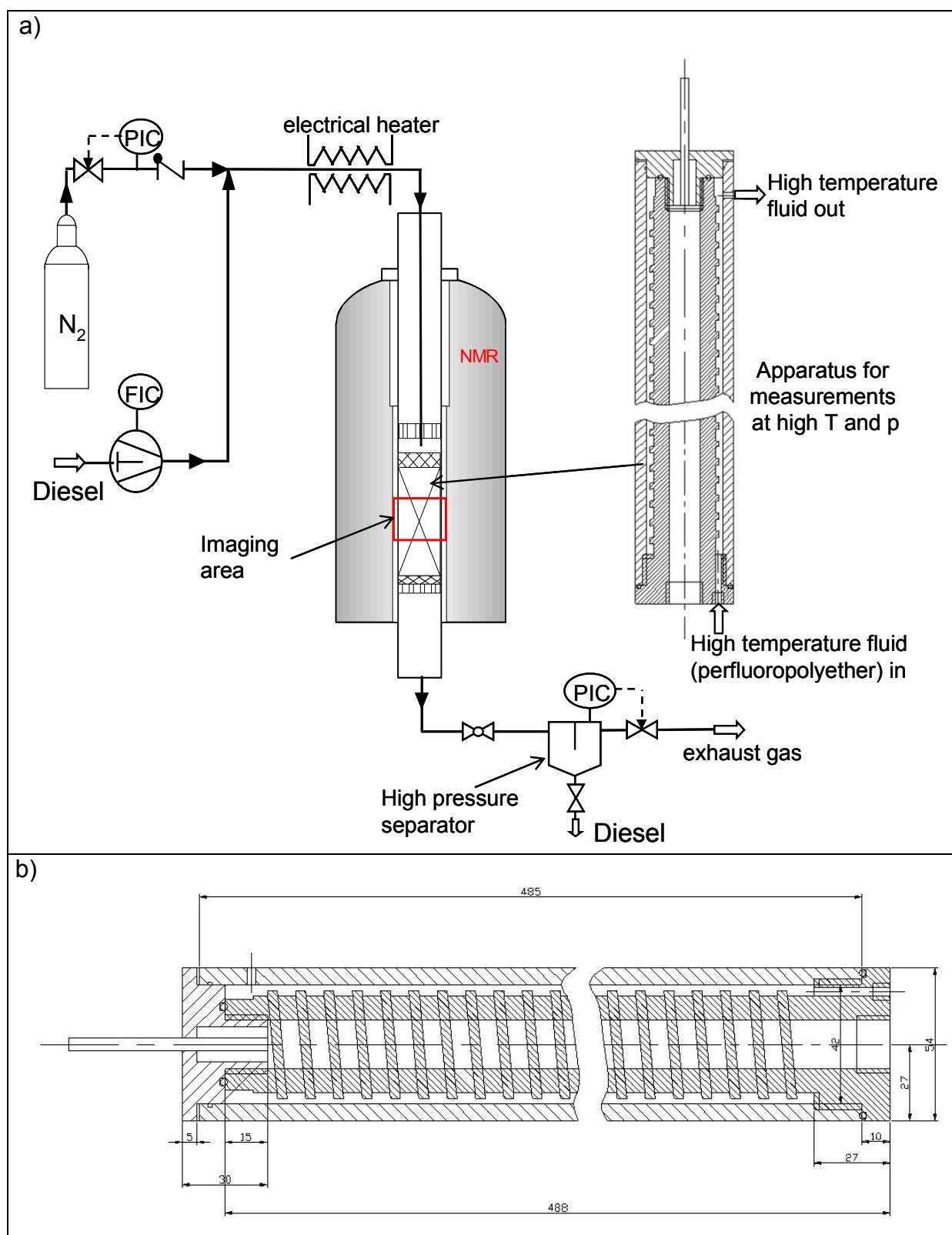
Figure 5.1: a) Scheme for MRI experiment set-up, b) Longitudinal cut of the apparatus used for experiments at high temperatures and pressures.

The obtained image data were further analyzed for quantitative determination of porosity of packed beds and liquid phase distribution.

5.1.2 Data analysis

The MRI raw data were first Fourier transformed and then transferred to local computers for further off-line processing with the help of the software PV-WAVE® from *Visual Numerics* and MATLAB®. The first step of any analysis of the image data is the elimination of the noise signals which are caused by small anomalies in the measurement electronics and depend on imaging parameters. In the following example, the method to eliminate the noise signals for determining the voidage in packed beds is presented. Fig. 5.2a is a horizontal slice having a matrix of 256 x 256 extracted from a 3D-image, which was taken at zero flow and the packed bed was saturated with polyethyleneglycol solution. The signal intensities in one line of this matrix shown in Fig. 5.2b can be classified in two groups. The first group contains voxels having high densities, over the noise level (I_0 = 5000) as indicated by a horizontal bar in Fig. 5.2b.
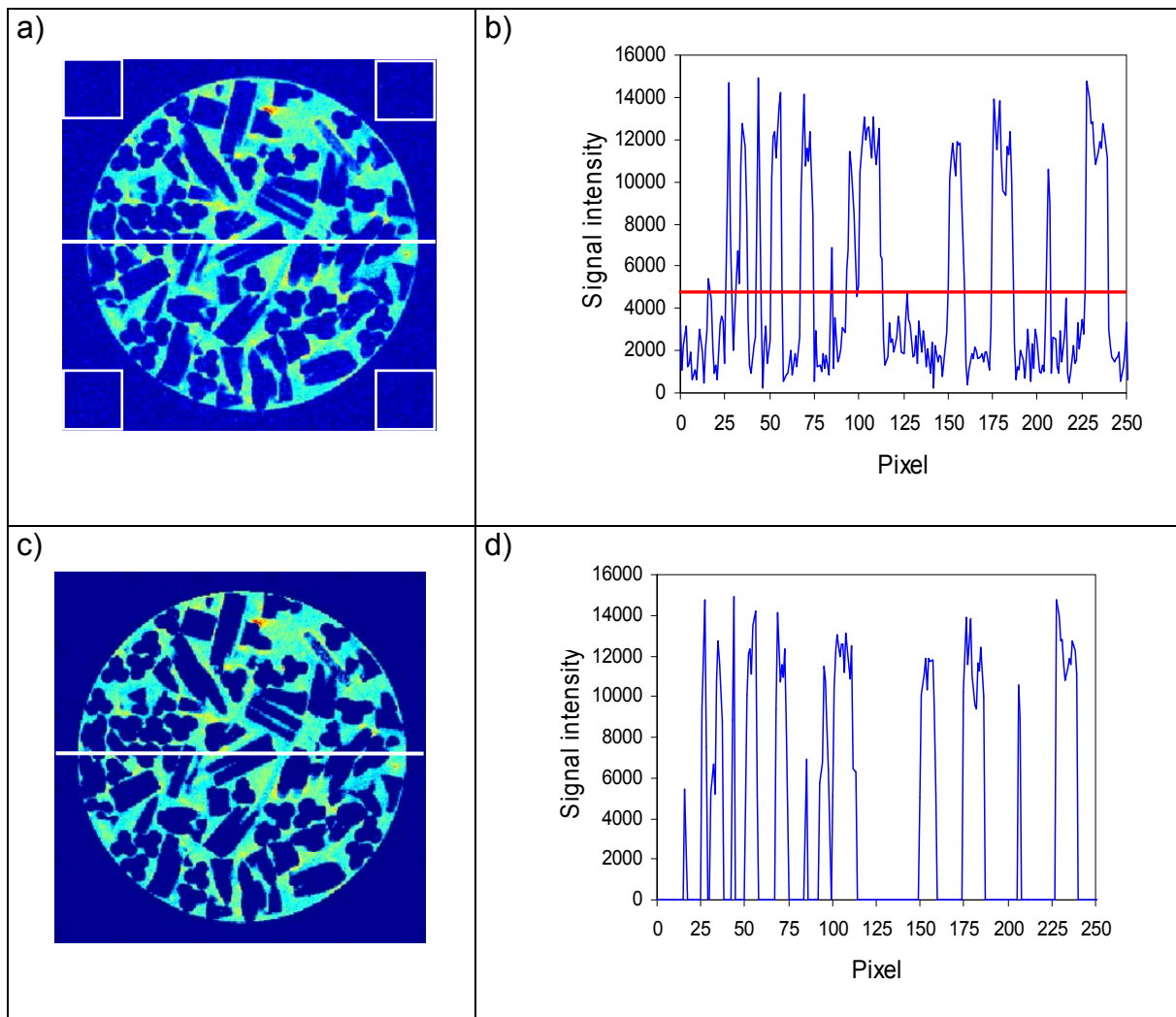
Figure 5.2: 2D-slice a) extracted from a 3D-image of a trilobe packing b) signal intensities before noise elimination along one line marked as a white line across the slice in a). Slice c) and diagram d) represent the results after noise elimination. Solid phase is shown in dark colour.

36

These voxels are fully filled with liquid and situated in voidage areas. Whereas the remaining voxels having intensities below 5000 belong to a second group, that contains partially liquid filled voxels, solid voxels (particles) and voxels lying outside the packed bed. Theoretically, all voxels in the regions outside the packed bed should have zero intensity because they have no spin density. However, it can be clearly seen in Fig. 5.2a that there are signals in the solid matrix. These signals are therefore considered as noise signals and should be eliminated. For further data analysis, a precise estimation of the noise level I_0 is very important, because it significantly affects the measured porosities of the beds. To examine the accuracy of MRI method, the calculated mean porosities of the beds were compared with those determined by the gravitational method. The largest error of results (Tab. A2 in appendix A) obtained by both methods is 1%. In this example, the noise level (I_0 = 5000) is defined as the mean value of voxel intensities placed in 4 small quadrants at corners in Fig. 5.2a, which are marked by white lines. After eliminating the noise signals in Fig. 5.2b, the voxel intensities in the solid matrix (second group) are reduced to zero as shown in Fig. 5.2d. Consequently, a no-noise image is obtained in Fig. 5.2c, where only the interested region of packed bed is displayed.

The noise intensity level can also be determined by a histogram of voxels' intensities values of a 3D-image as illustrated in Fig. 5.3. In the histogram, two peaks are very clearly distinguishable. The first peak centred at the intensity of about 2000 originates either from voxels located in the solid particles or outside of the packed bed. By theory from these voxels no MR signals can derive. This peak therefore is denoted by the "noise peak". The second peak, concentrated around 12500, originates from voxels filled with liquid. Voxels with values between the two peaks can be classified either containing liquid or solid or both. The noise level which discriminates between the object and the background of an image is then determined by choosing the intensity of the global minimum (5000) between the two peaks. In order to simplify the subsequent data analysis, the image's data are transformed to a binary form, in which all voxels have intensities equal or lower than the noise level are set to zero. The other voxels are assigned to one. To examine the accuracy of the MRI method, mean porosities and static liquid saturations obtained by image analysis were compared with those determined by the gravitational method. The largest difference between results obtained by both methods is less than 3%.

However, in some cases the histograms present only one local maximum peak and it is therefore very difficult to distinguish real signals from background noise. Hence, the method of using regional noise intensity in every slice as seen in Fig. 5.2 is preferably applied for determination of the threshold level.
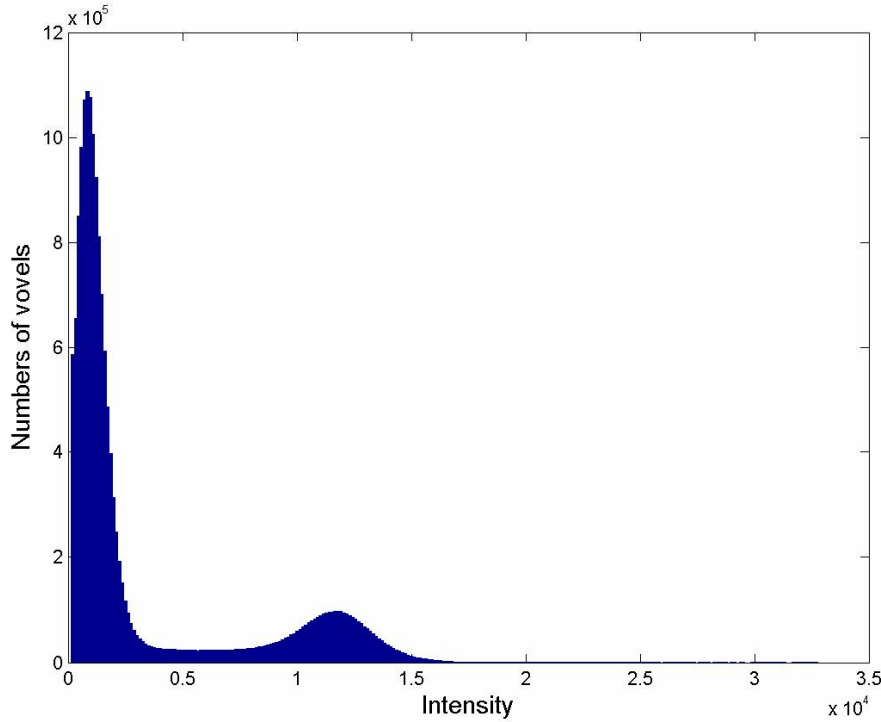
37

Figure 5.3: Histogram of voxels' intensities obtained from a 3D-image dataset

5.1.3   Calculation of porosity

After noise elimination, the local porosity and liquid saturation can be calculated from the voxels in the binary gated image. To determine the porosity first a 3D-image of the packing structure is acquired at zero flow velocity. The packing has been completely filled with liquid and evacuated for at least 6 h in order to remove possibly small air bubbles to be trapped in the liquid. From this image the local porosity distribution of the packing can be calculated. Additionally, it serves as reference picture for the subsequent calculation of liquid saturation and wetting efficiency.

To obtain radial porosity profiles, each of the slices z_i extracted from 3D-images is first divided into small annular segments having each the same surface area as schematically illustrated in Fig. 5.4. Then, the local radial porosity $\varepsilon_{zi,rj}$ of every segment r_j in the slice z_i is defined as a fraction between the voidage volume, $V_{H,zi,rj}$ and total volume, $V_{0,zi,rj}$ of that segment. It is simply calculated as the ratio of the number N_L of liquid filled voxels (grey voxels) and the total number of voxels N_0 in such a small segment (eq. 5.1).

$$\varepsilon_{zi,rj} = \frac{V_{H,zi,rj}}{V_{0,zi,rj}} = \left.\frac{N_L}{N_0}\right|_{zi,rj} \tag{5.1}$$

where z_i is the slice i and r_j the annulus j .

38

The mean radial porosity profile for the whole 3D-image was obtained by averaging the local porosities $\varepsilon_{zi, rj}$ over the total number n of slices z_i according to equation 5.2a. Likewise, the vertical porosity profile is calculated by averaging $\varepsilon_{zi, rj}$ over the total number m of annuli r_j (eq. 5.2b)

$$\varepsilon_r = \frac{V_{H,rj}}{V_{0,rj}} = \frac{1}{n} \cdot \sum_{i=1}^{n} \varepsilon_{zi, rj} \tag{5.2a}$$

$$\varepsilon_z = \frac{V_{H,zi}}{V_{0,zi}} = \frac{1}{m} \sum_{j=1}^{m} \varepsilon_{zi,rj} \tag{5.2b}$$

where *n* is the number of slices and m is the number of annuli.

The overall porosity ε_b of the packing is calculated by averaging all the porosity values ε_r.

$$\varepsilon_b = \frac{V_{H,bed}}{V_0} = \frac{1}{m} \sum_{j=1}^{m} \varepsilon_{rj} = \frac{1}{n} \sum_{i=1}^{n} \varepsilon_{zi} \tag{5.3}$$

where m is the number of annuli.
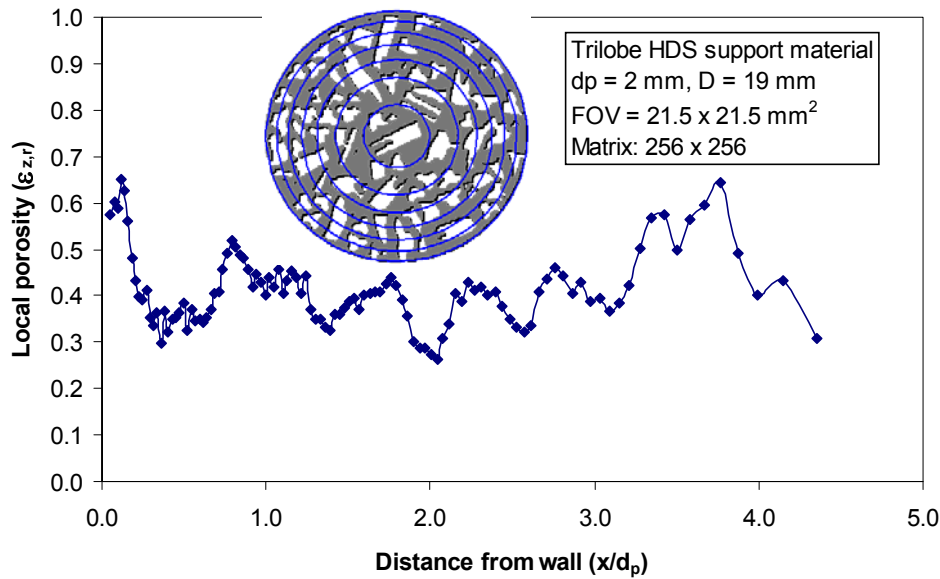
Figure 5.4: Radial porosity profile from a 2D-image. In the binary image, liquid voxels representing voidage area are shown as grey color and solid voxels as white color. The equivalent diameter (d_p) of trilobe particle is 2 mm.

Fig. 5.5 shows typical 2D-slices of 3D-images and the radial distribution of porosity ε_{rj} perpendicular to the axis of the column for the investigated packings of spherical and trilobe particles. The mean porosity profiles are obtained by integrating the calculated values $\varepsilon_{zi, rj}$ over the bed height according to equation 5.2. The matrix size for the acquisition of 3D-images was 256^3 giving an isotropic spatial resolution of 84μm. About 23 voxel lengths equal the average characteristic length of the particles in the investigated packings.
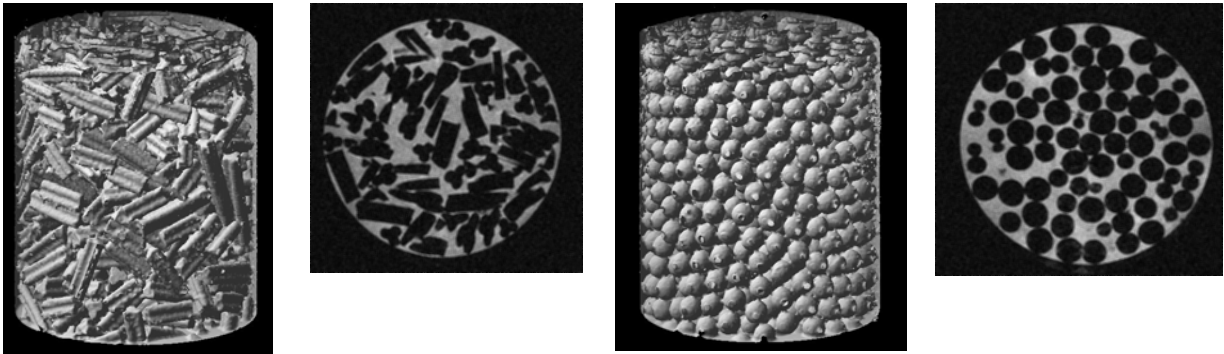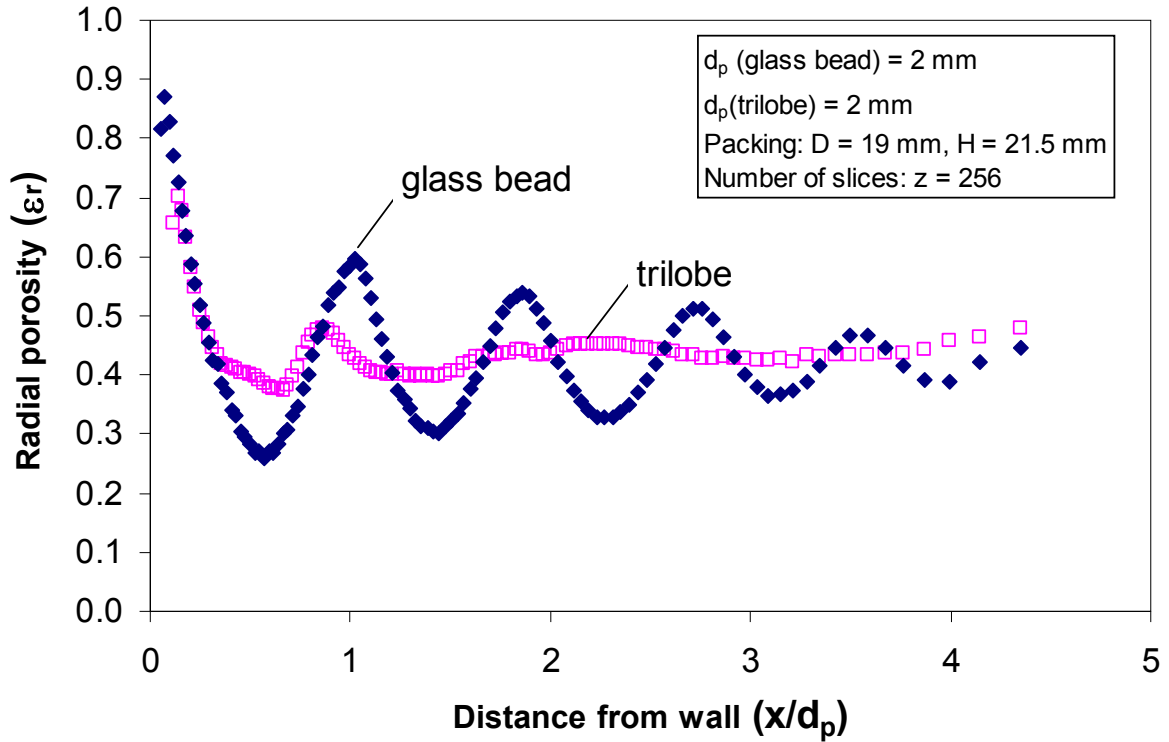
Figure 5.5: Radial distribution of porosity for packings of spherical glass beads and porous catalyst support trilobe particles.

5.1.4 Calculation of liquid saturation and wetting efficiency

Data analysis procedure to quantify liquid saturation and wetting efficiency from data of 2D-images is described by means of Fig. 5.6. To determine the liquid saturation the probe's volume was first imaged under conditions of no flow when the packing was entirely filled with liquid as it is used for porosity determination. Then, another image of the same probe's volume was taken under two phase flow condition. For each slice z_i the liquid containing voxels are counted for the two conditions. The same procedure to determine local porosity as illustrated in Fig. 5.4 can be applied to calculate the local liquid saturation. From the completely filled bed (Fig. 5.6a) the number of void space voxels $N_{V,,zi,rj}$ for every segment r_j of is obtained, whereas Fig. 5.6b gives the number of liquid voxels $N_{L,zi,rj}$ under two phase flow condition. The local liquid saturation $\beta_{zi,rj}$ is consequently determined as the fraction of liquid voxels and

void space voxels as indicated in equation 5.3. Analogue to porosity calculation, the radial profile of mean liquid saturation for the whole 3D-image was obtained by averaging the local saturations $\beta_{zi, rj}$ over the total number n of slices z_i according to equation 5.4a. Similarly, the vertical liquid saturation profile over the bed length is given in equation 5.4b. The overall liquid saturation of the entire bed is also called as the bulk liquid saturation β_b which is obtained by averaging over the number of slices in the bed (eq. 5.5).
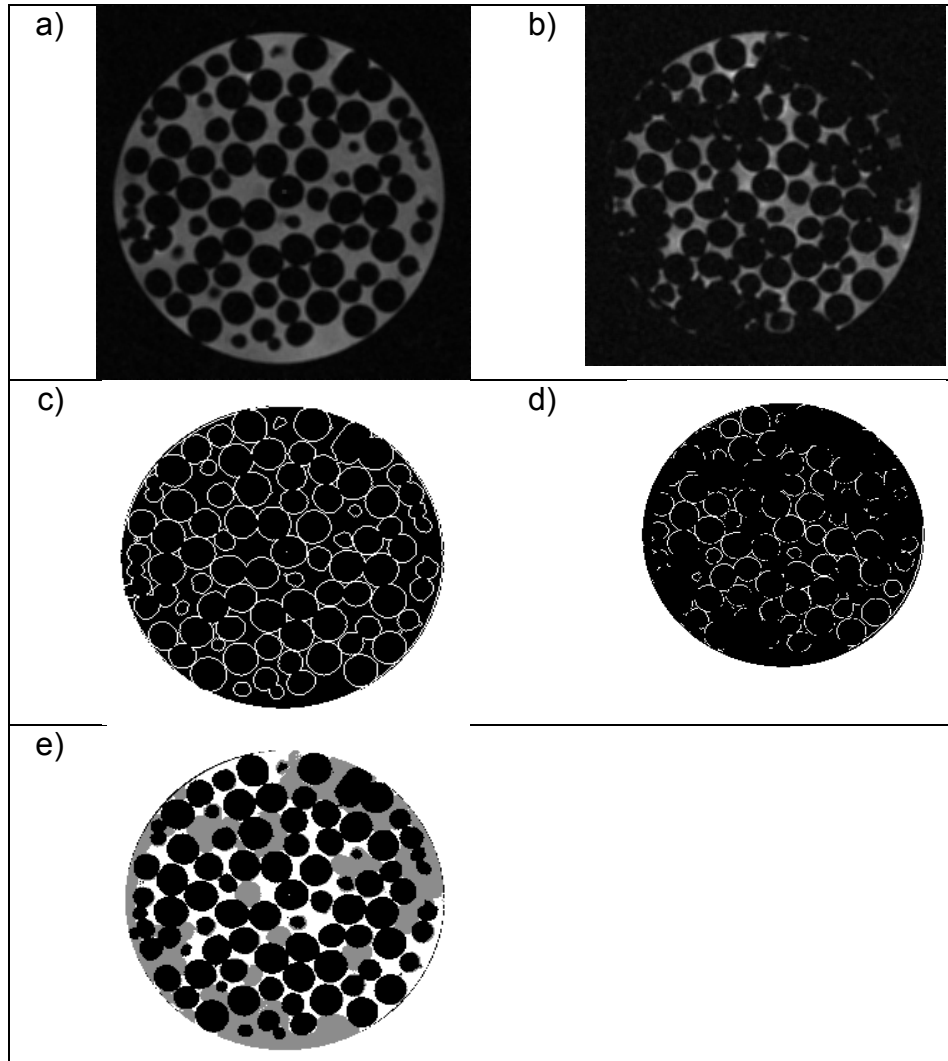

Figure 5.6: Basis for the data analysis procedure; a) reference image for determining the void space acquired at zero flow of water; b) image acquired under trickle flow at u_{0L} = 3.9 mm/s and u_{0G} = 21 mm/s; c) the same slice as a), only voxels containing liquid-solid contact (surface voxels) are identified; d) surface voxels at trickle flow were identified for determining wetting efficiency; e) reconstructed image by subtraction of b) from a), in which phases are distinguished by colors: white: liquid, grey: gas and black: solid.

$$\beta_{zi, rj} = \frac{V_{L, zi, rj}}{\varepsilon_{zi, rj} V_{0, zi, rj}} = \left. \frac{N_{L,}}{N_L + N_G} \right|_{zi, rj} \qquad (5.3)$$

$$\beta_r = \frac{V_{L,rj}}{\varepsilon_{rj} V_{0,rj}} = \frac{1}{n} \cdot \sum_{i=1}^{n} \beta_{zi,\,rj} \qquad (5.4a)$$

$$\beta_z = \frac{V_{L,\,zi}}{\varepsilon_{zi} V_{0,\,zi}} = \frac{1}{m} \sum_{j=1}^{m} \beta_{zi,rj} \qquad (5.4b)$$

$$\beta_b = \frac{V_L}{\varepsilon_b V_0} = \frac{1}{m} \sum_{j=1}^{m} \beta_{rj} = \frac{1}{n} \sum_{i=1}^{n} \beta_{zi} \qquad (5.5)$$

Where n is the number of slices and m the number of rings.

As described in 2.2.2, the external liquid saturation can be divided into a dynamic part $\beta_{b,d}$ and a static part, $\beta_{b,st}$ (eq. 5.6).

$$\beta_b = \frac{V_L}{\varepsilon_b V_0} = \beta_{b,d} + \beta_{b,st} \qquad (5.6)$$

The former is the fraction which flows continuously through the packed bed. The later is the liquid fraction which remains at the catalysts' contact points due to capillary forces. For determination of the static liquid saturation $\beta_{b,st}$, MRI images were taken under conditions, when the dynamic liquid part in the packed bed has completely drained after the gas and liquid flows had stopped. From the measured data of β_b during two phase flow and $\beta_{b,st}$ subsequently determined, $\beta_{b,d}$ is calculated by equation 5.6. The local quantities of liquid saturation are also determined by the same procedures based on the local distributions of the dynamic and static liquid parts.

The wetting efficiency is defined as the fraction of the catalyst particle external area effectively wetted by the flowing liquid. For determining wetting efficiency Fig. 5.6c & 5.6d are used, in which only liquid voxels having contact with solid particles, i.e. *surface voxels* are identified. The fraction of number of surface voxels $N_{SL,\,zi}$ in Fig. 5.6d to those $N_{SL,0,zi}$ in Fig. 5.6c is defined as wetting efficiency, $\eta_{ce,z}$ of slice z_i. Analogue calculation of liquid saturation, the equations for calculation of wetting efficiencies are formulated:

$$\eta_{ce,\,zi,rj} = \frac{A_{cat,L,zi,rj}}{A_{cat,0,zi,rj}} = \left. \frac{N_{SL}}{N_{SL,0}} \right|_{zi,rj} \qquad (5.7)$$
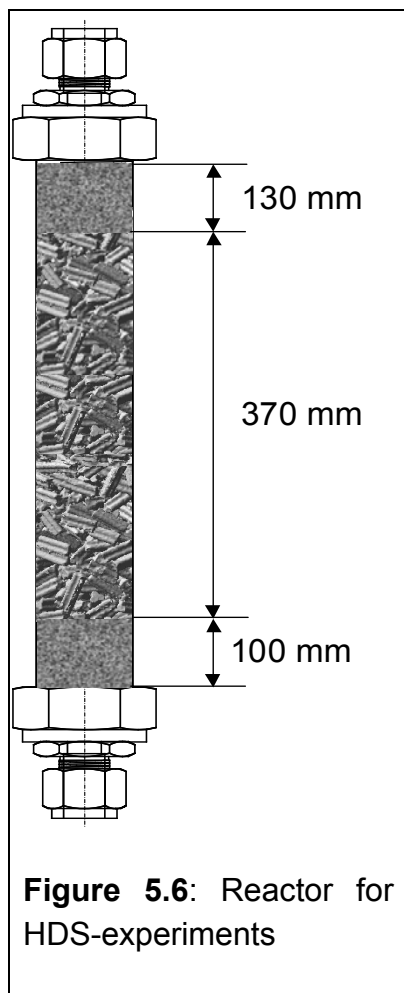
$$\eta_{ce,r} = \frac{1}{n} \cdot \sum_{i=1}^{n} \eta_{ce,\,zi,rj} \qquad (5.8a)$$

$$\eta_{ce,z} = \frac{1}{m} \cdot \sum_{j=1}^{m} \eta_{ce,\,zi,rj} \qquad (5.8b)$$

$$\eta_{ce,b} = \frac{A_{cat,L}}{A_{cat,0}} = \frac{1}{m} \sum_{j=1}^{m} \eta_{ce,\,rj} = \frac{1}{n} \sum_{i=1}^{n} \eta_{ce,\,zi} \qquad (5.9)$$

5.2 HDS-experiments

5.2.1 Experimental setup

130 mm

370 mm

100 mm

Figure 5.6: Reactor for HDS-experiments

HDS-experiments were carried out in a bench scale trickle bed reactor, which has 19 mm inside diameter and 600 mm in total length (Fig. 5.6). The top and the bottom of the reactor were filled with inert SiC-particles of 0.2 mm diameter. The catalyst bed consisted of CRITERION 424 catalyst and had a length of 370 mm. Between the catalyst bed and the SiC-layers, thin layers of glass wool were applied to avoid SiC-particles to migrate into the catalyst bed. The amount of catalyst for the undiluted bed was 90 grams.

A flow sheet of the bench scale plant is shown in Fig. 5.8. Diesel oil from a storage vessel was brought to the reaction pressure with the help of a high-pressure piston pump. Two gas bottles, one with pure hydrogen (H_2) and another with a mixture of hydrogen/hydrogen sulfide (H_2/H_2S) supply the gas flows which were controlled by two Brooks mass flow controllers. Both gas and liquid are mixed and preheated before entering the trickle-bed reactor.

The reactor temperature was maintained at the desired values by using four electric heaters along the reactor tube in order to ensure isothermal operating condition of the reactor. Another heater was installed directly upstream the reactor to preheat the feed. Every heater was equipped with a temperature sensor (thermocouple) in order to control the temperature of the reactor section being locally heated. The whole arrangement is insulated to prevent heat losses. Temperature sensors and heaters are connected to TIC controllers to keep the temperature constant.

After leaving the reactor, the products cooled down by transfering part of their heating energy to the atmosphere through the unisolated tube wall and entered subsequently a high pressure separator, where gases and liquids were separated. A pressure controller maintained the operating pressure downstream. After passing the pressure controller, the gas phase was at ambient pressure. Two flasks containing sodium hydroxide (NaOH) solution were used to neutralize hydrogen sulfide.

The high pressure separator, having a volume of 800 ml, allows to collect liquid products for a time period of approximately 3 to 8 hours (depending on LHSV), therefore it is not required to empty it during an experiment.

Liquid samples were taken during the experiment via a little container bypassing the high pressure separator. Every time a sample was taken the vessel was cleaned twice with acetone, and then was dried with air. Since the liquid samples contained small amounts of absorbed H_2S and H_2, they were stripped with N_2 gas.

The temperature profiles were measured by a movable axial thermocouple located inside the concentric thermo-well. The differences in the measurements between the temperature sensors for the temperature control and the moveable thermocouple are used for manually correcting the TIC inputs to assure that the TIC receive the correct temperature. Typical temperature profiles along the catalyst bed for five operating temperatures and for LHSV of 1 h^{-1} to 4 h^{-1} are shown in Fig. 5.7. Deviations from the desired temperature in the TIC controllers were observed for both ends of the catalyst bed, while the temperature in the middle of the catalyst bed was more stable. The temperature uncertainty was $\pm$ 2K.
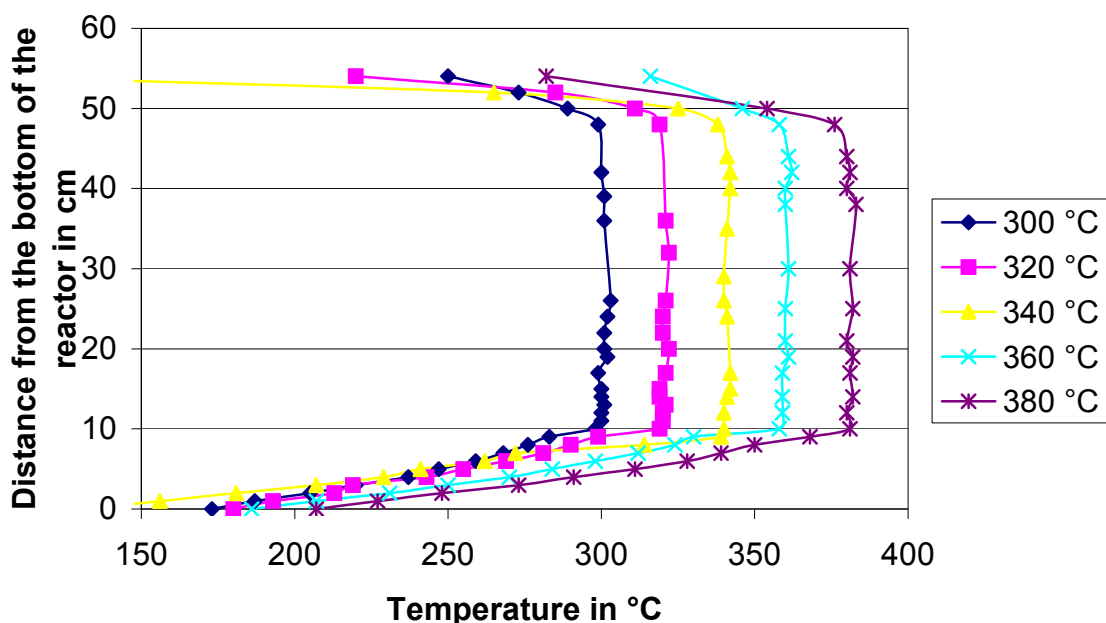

Figure 5.7: Temperature profiles across the reactor measured at different LHSVs

Every experiment lasted from 3 to 5 hours depending on liquid flow (LHSV). This long operation time was established to assure steady-state conditions in the reactor. Before taking the samples, the temperature across the reactor, the pressure, the gas and the liquid flows were checked to see whether the system was at the desired operating conditions.
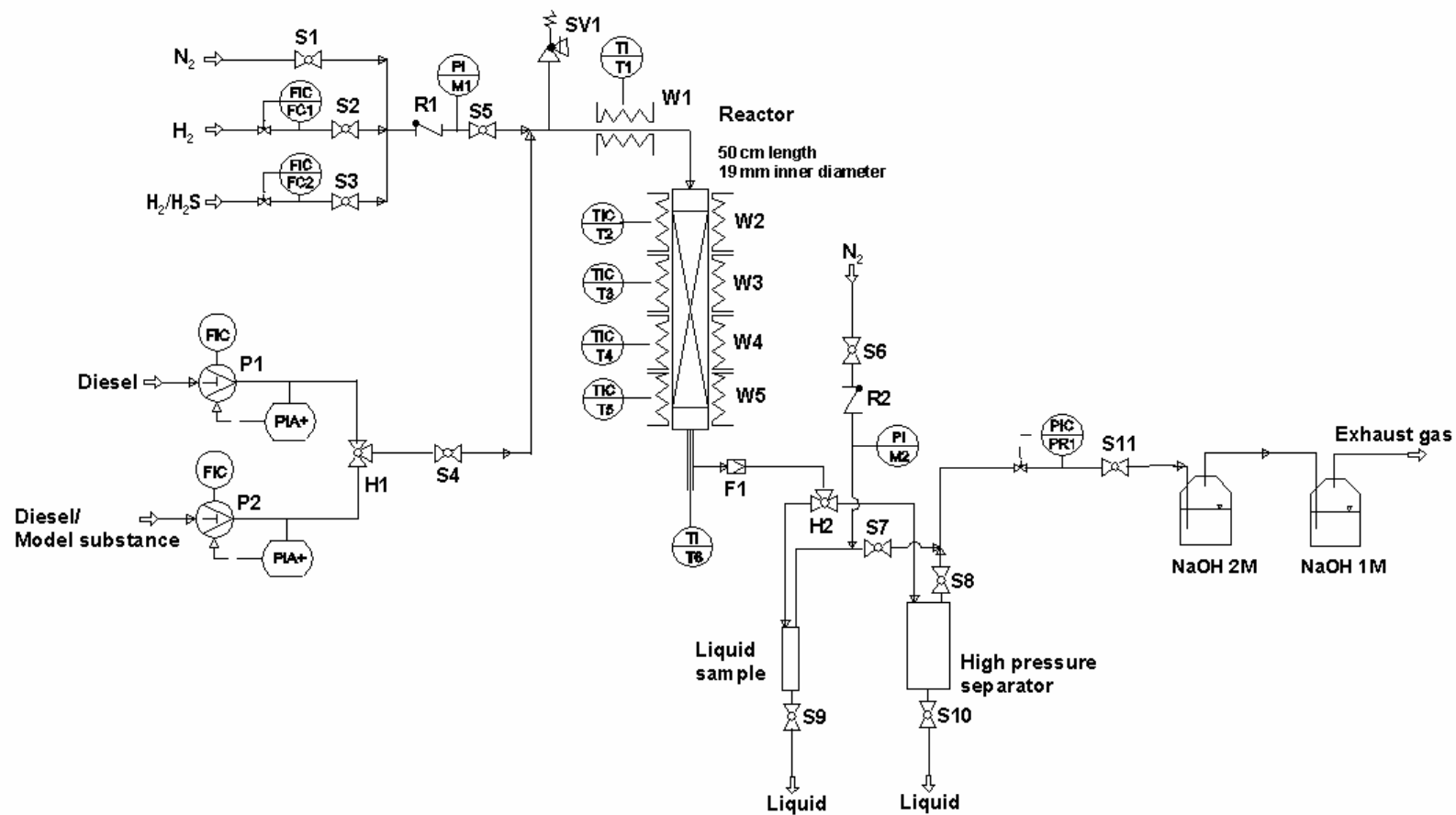
Figure 5.8: Schematic of plant for hydrodesulfurization of gasoils

45

5.2.2 Catalyst

For the catalytic reaction experiments, the catalyst CRITERION 424 was used in the form of trilobe particles. Chemical composition of the catalyst and its physical properties important for reaction and mass transfer are listed in Tab. 5.1. Prior to HDS experiments, the catalyst was presulfided under a pressure of 60 bar by a solution of 4 Vol. % dimethydisulfide (DMDS) in diesel oil at a heating rate of 25°C/h until the desired temperature of 350°C was attained and kept for 20h. After sulfidation, the catalyst was stabilized for 3 days at 40 bar and 340°C, under a hydrogen flow containing 1.4 Vol. % of H_2S.

Composition in the oxidised form (wt%)		Physical properties	
NiO	4	Area in m^2/g	155
MoO_3	19.5	Average diameter in mm	1.6
P_2O_5	8	Average length in mm	5
Al_2O_3	68.5	Bulk density in kg/m^3	820

Table 5.1: Catalyst properties.

The sulfidation procedure is specified in table 5.2 [Ped03]. Every 3 hours a sample was taken from the system and analyzed for sulfur concentration. Fig. 5.9 shows the measured sulfur concentration at the outlet of the reactor against the reaction temperature during the sulfidation time. As can be seen the sulfur concentration decreases slowly at the beginning due to the low temperature (< 100°C). The slope of the concentration's curve is steeper at higher temperature. It indicates that the catalyst's activity increases strongly with the increasing temperature. After 24 hours the catalyst reached its maximum activity, and then the sulfidation process was completed.

p (bar)	LHSV (h^{-1})	$^V\Phi_G/{}^V\Phi_L$-ratio in Nm^3/m^3	$y_{H2S,o}$	Temperature setting
60	3	540	0	Heating to 100 °C for 3 hours;
60	3	0	0	3 hours at 100 °C
60	3	165	0	2 hours from 100 °C to 200 °C; with a rate of 50 °C/h
60	2	165	0	5 hours from 200 °C to 250 °C, with a rate of 10 °C/h
60	2	165	0	5 hours from 250 °C to 350 °C, with a rate 20 °C/h
Stabilisation				
40	0.75	340	0.014	340 °C for 3 days

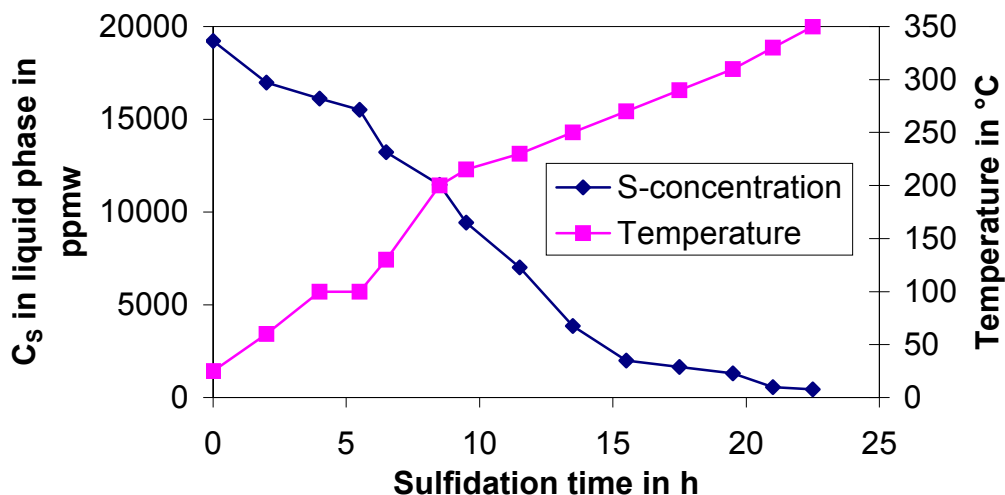**Table 5.2**: Experimental conditions for sulfidation process and stabilisation.

Figure 5.9: Development of the reactor temperature and the residual sulfur concentration in the liquid phase during the sulfidation process

After sulfidation the catalyst must be stabilized under the operating conditions as shown in table 5.2 for 3 days. However, the conversion of sulfur, which is measured periodically during this time, did not change after 2 days. That means the activity of catalyst was stable and thus was ready for the HDS-experiments.

5.2.3 Analytical procedure

The sulfur contents of the feedstock and of the hydrotreated oil samples were determined by an energy dispersive X-Ray fluorescence spectrometer (Oxford Lab X 300). Before measuring, the samples were purged with nitrogen to strip dissolved H_2S. Sulfur compounds were selectively determined with a high resolution gaschromatograph (Varian STAR 3400) equipped with a selective PFPD (pulsed flame photometric detector). The hydrocarbons were detected by a FID (Flame Ionization Detector). Nitrogen compounds were analyzed by gaschromatography (HP 5890 Series II Plus) with NPD (Nitrogen Photometric Detector).

The concentrations of aromatic compounds (mono-, di-, polyaromatics) were determined by HPLC (High Performance Liquid Chromatography) applying ASTM D6591-00 method. Naphthenes were determined from the non-aromatic part of the elution chromatography by ASTM D-2425-93.

5.3 RTD-measurement

The pulse injection method was used for measuring the residence time distribution (RTD) in the same reactor as it was used for hydrodesulfurisation experiments. Fig. 5.10 shows the schematic setup of the apparatus. The experiments were performed

at a temperature of 150°C and at a pressure of 40 bar. Squalane was chosen as tracer substance because it has high boiling temperature (176°C) and its density is close to that of diesel oil. The liquid flow rates were adjusted to LHSV values from 1 h^{-1} to 4 h^{-1}. Hydrogen was replaced by nitrogen as gaseous compound. A small quantity of squalane was rapidly injected to the gas oil stream via the three-way valve. Then, the liquid samples taken at the reactor outlet were analysed by gas chromatography to determine the squalane concentration as a function of time.
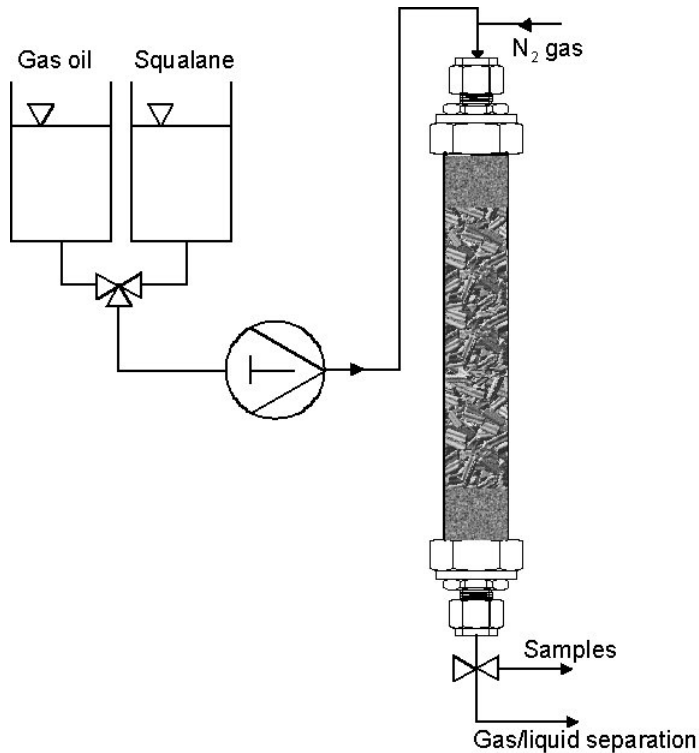

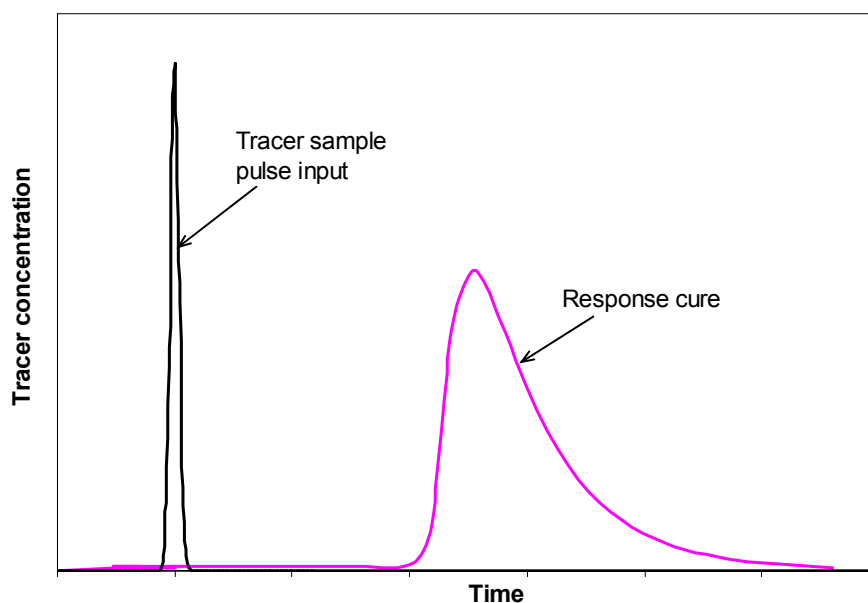**Figure 5.10**: Schematic experiment setup for RTD measurement

Figure 5.11: Qualitative illustration of pulse input and tracer response curve

48

A typical response curve is illustrated in Fig. 5.11. If an ideal impulse of tracer is injected at the inlet of the system at time t=0 and its concentration is measured as a function of time at the outlet, then E(t)dt represents the fraction of the tracer having a residence time in the time interval (t, t+dt) or as otherwise stated $E_i(t)$ is the probability for a tracer element to have a residence time of t+dt.

$$E_i(t) = \frac{C_i(t)}{\int_0^\infty C_i(t)dt}$$

(5.10)

such that:

$$\int_0^\infty E_i(t)dt = 1$$

(5.11)

where: i = 1, 2, ….n being the number of concentration measurements, $C_i(t)$ is tracer concentration and $E_i(t)$ is the residence time distribution function.

The residence time of the tracer in the column is small as compared to the time required for the tracer to diffuse into the catalyst pores. Therefore, it is assumed that the porosity of the catalyst has a negligible effect on the tracer movement in the packed bed. Based on the above considerations, the obtained RTD data were simulated using a two-parameter axial dispersion model with open-open boundary conditions [Lev93]. That means there is no dispersion at both inlet and outlet of the reactor.

$$\frac{\partial \varphi}{\partial \theta} = -\frac{\partial \varphi}{\partial Z} + \frac{1}{Pe}\frac{\partial^2 \varphi}{\partial Z^2}$$

(5.12)

where: φ = C/C_0 – dimensionless tracer concentration, Pe= $u_L L/D_{ax}$ – Peclet number, Z=z/L – dimensionless axial co-ordinate, u_L – liquid phase velocity, D_{ax} – axial dispersion coefficient, θ =t/τ – dimensionless time, τ = L/u_L – theoretical mean residence time, C_0 – initial concentration.

The analytical solution of the above equation for open-open boundary condition was used to evaluate the experimental data in order to find the best-fit value of Pe number [Lev93].

$$E(\theta) = \frac{1}{2}\sqrt{\frac{Pe}{\pi \theta^3}} \exp\left(-Pe\frac{(\theta-1)^2}{4\theta}\right)$$

(5.13)

6 Results and discussion

The first part (chapter 6.1) in this chapter considers mainly the following topics: porosity distribution of packed beds consisting of various particle geometries, the effects of bed porosity, physical properties of fluids and operating conditions (e.g. temperature and pressure) on the phase and velocity distributions. Based on these experimental data, empirical correlations for the porosity distribution, liquid saturation and pressure drop are established. In the second part (Chapter 6.2), the dispersion coefficients based on the results of RTD-measurements at a bench scale reactor are determined. Finally, the third part (Chapter 6.3) presents the results of the HDS experiments in a bench scale reactor over a wide range of reaction temperatures and space velocities.

6.1 Fluid dynamic measurements with MRI

6.1.1 Structure of packed beds

It is known that non-uniform distribution of porosity of randomly packed beds has a significant effect on local fluid velocity and thereby contributes to the deviations from the ideal plug flow. This phenomenon is remarkedly relevant for laboratory reactors because of their small tube-to-particle diameter ratios (D/d_p). In regions very close to the wall, the higher voidage tends to give rise to a higher velocity, which causes bypass flow and consequently lowers the overall reaction conversion. Special attention, therefore, has been paid on the change in voidage near the wall [Vor83, Bey97]. These authors discuss extensively the velocity profiles of single phase flow in porous systems. With the development of high performance computers and advances in numerical technique, chemical engineers have started exploiting the power of computational fluid dynamics tools (CFD) applied to chemical engineering. Published research on CFD simulation the fluid dynamics of multiphase reactors have shown that bed structure (i.e., porosity distribution) strongly influences on local fluid velocities [Yin02; Jia01, Ran02], and ,hence, subsequently influences on reactor conversion. The CFD model of Gunjal and Ranade [Gun07] predicted that the difference of HDS conversion, considering uniform porosity distribution in the bed, was about 15% higher than in the case of where non-uniform bed porosity was considered. Experimental data of porosity distribution are thus crucial important for accurate simulating the fluid flow in porous systems. Much of published work, however, has been focused on spherical particles but little information is available on other forms of packings, which are widely used in the chemical industry. With the advantage of MRI technique, it is possible to access fully 3-dimensional bed structures. Therefore, one purpose of this work is to investigate systematically the

50

local and global porosity distributions in different random packed beds by analysing 3D-images.

a) Packed beds of spheres

The change in voidage of randomly packed beds of spheres has been the subject of many experimental studies using both destructive and non-destructive measuring techniques [Ben62, Rid68, Niu96, Gie98, Sha01, Bur04]. In summary, all published studies have indicated that the porosity within packed beds of spheres represents a damped oscillatory variation, which decreases with distance from the walls of the packed beds. In particular, the porosity very close to the wall is remarkably higher than in other regions. This gives rise to the so-called "wall effect" in flow pattern and transfer of heat and mass in packed beds. Since 1960s, many researchers have attempted to develop empirical correlations for the prediction of radial porosity profiles based on experimental data available in the literature. Equations which are used to compare with data of MRI-measurements in this study are presented in appendix A. They can be classified into two main groups. The investigators of the first group [Mar78, Coh81, Gie98] apply two equations to predict the radial porosity distribution. In the region near the wall within a distance of about 0.5 sphere diameter, the porosity variation can be approximated by a polynom function, while the oscillatory variation in the inner zone is determined by a damped cosine function. The authors of the other group [Mue91; Rot96] use only one equation to determine the radial porosity distribution. Mueller [Mue91] used a Bessel function with 3 parameters which are fitted to literature data [Rob58, Ben62, Rid68]. Based on optical experiments with LDA-technique, Rottschäfer [Rot96] proposed an equation which contains a series of Fourier functions with 4 fitted parameters.

The quality of the equations for predicting the radial porosity shown in Tab. 6.1, appendix A is statistically evaluated by using experimental MRI data for packed beds of glass beads having a wide range of tube-to-particle ratios (D/d_p) from 7 to 14. For example, Fig. 6.1 shows the local porosity from a set of experimental data for $D/d_p = 9.5$ along with curves calculated with equations from appendix A. In general, all the models, except the model of Mueller, predict quite accurately the change of porosity in the region from the wall to 0.5 sphere diameter. However, in the oscillatory region, the curves calculated according to Giese [Gie98], Martin [Mar78], Mueller [Mue91] and Rottschäfer differ relatively in their phases and amplitudes from the MRI data. It can be seen that the equation of Cohen & Metzner [Coh81] does not estimate the phase in the bulk region correctly.

It is found that each equation can estimate accurately the porosity distribution for a limited number of MRI data sets as indicated in Tab. 6.1. This is not surprising, since most equations were developed by fitting to experimental data measured in specific validity domains. Therefore, it is needed to modify the existing equations or to develop a new correlation in order to increase the accuracy in predicting the porosity profiles over a wider range of D/d_p-ratios. In this context, a modified correlation

[Bur04] as described in Tab. 6.2 is developed to give a better fit for the whole range of MRI database. The first part of this correlation (eq. 6.1a) is identical with Martin's equation, which describes the parabolic change of porosity in the near-wall region. The domain of this equation, however, is slightly different from Martin's equation ($0 < x/d_p < 0.55$). The second part (eq. 6.1b) of the equation containing 5 empirical constants is derived from Giese's equation for predicting the damped oscillatory porosity in the bulk region. Fig. 6.2 shows a good agreement between experimental data for $D/d_p = 14.25$ and predicted values from equation 6.1b. It is also clearly seen in this figure that differences in porosities of different D/d_p-ratios appear at the local peaks. The smaller the D/d_p-ratio, the higher is the porosity at the peak. Due to image artefacts at areas very close to the wall caused by magnetic inhomogenities during the MRI-measurements, the local porosities at the wall are not correctly quantified.

Models	D/d_p	AARE (%)				σ (%)			
		7.125	9.5	11.4	14.25	7.125	9.5	11.4	14.25
Martin (A.1)		13	11	8.7	11	10	7.7	5.7	9
Giese (A.3)		12	10	7.8	9.7	6.7	6.1	6	8.7
Cohen & Metzner (A.2)		24	19	17	18	15	12.5	10	12
Mueller (A.4)		11	10	10	8.3	13	8	8.5	7
Rottschäfer (A.6)		8.4	8	6	7.2	5.6	5.6	4.5	6.2
Van Buren (Tab. 6.2)		5.5	5.7	6.4	7.3	4	4.2	5.4	6.6

Table 6.1: Statistical evaluation of equations from literature based on MRI-data

The statistical analysis of the selected models including the new model of van Buren [Bur04] is summarized in Tab. 6.1. It shows how good the models' predictions are in terms of accuracy and broadness. Among the selected models, Rottschäfer's model yields the best statistical numbers with average absolute relative errors (AARE) below 8.4% and standard deviations (σ) below 6.2% for the whole range of MRI data. The other literature models can be ranked relating to their predictions' quality in the following order: Mueller, Martin, Giese and Cohen & Metzner. As a whole, the new equation (Tab. 6.2) is an improvement in predicting porosities for the whole range of MRI data.

$$\varepsilon\left(\frac{x}{d_p}\right) = \begin{cases} \varepsilon_{min} + (1 - \varepsilon_{min})\left(\frac{x}{Td_p} - 1\right)^2 & \text{für} \quad \frac{x}{d_p} \leq T \quad (6.1a) \\[3mm] \varepsilon_\infty + A\exp\left(B\frac{x}{d_p}\right)\cos\left[2\pi\left(C\frac{x}{d_p}\right) + D\right] & \text{für} \quad \frac{x}{d_p} > T \quad (6.1b) \end{cases}$$

$where:$

$A = 0.26 \;\; ; \;\; B = -0.32 \;\; ; \;\; C = 1.12 \;\; ; \;\; D = -0.14; \;\; T = 0.55$

$\varepsilon_{min} = 0.23 \;\; ; \;\; \varepsilon_\infty = 0.375 + 0.34\dfrac{d_p}{D} \;\; according \;\; to \; Jeschar \, [Jes64]$

Table 6.2: Modified correlation and fitting parameters derived from MRI measurements [Bur04].

Since the porosity distribution in packed beds is random in nature, it is useful to characterize such randomness of the system by applying a statistical methodology. In this study, two propability density functions, namely normal and lognormal distribution functions (eq. 6.2 and eq. 6.3, respectively) were found to desribe such random distribution of porosity. In general, the spatial porosity distribution within a packed bed depends mainly on the D/d_p-ratio. It is shown in Fig. 6.3 that at a high D/d_p-ratio (D/d_p = 14.25), porosity has a uniformed normal distribution, while the porosities at smaller D/d_p-ratios exhibit lognormal distributions and have unsymmetrical curves due to the influence of the so-called "wall effect".

$$P(\varepsilon) = \frac{A}{\sigma\sqrt{\dfrac{\pi}{2}}} e^{-2\frac{(\varepsilon - \varepsilon_b)^2}{\sigma^2}} \tag{6.2}$$

$$P(\varepsilon) = \frac{A}{\sigma\varepsilon\sqrt{2\pi}} e^{-\frac{\ln\left(\frac{\varepsilon}{\varepsilon_b}\right)^2}{2\sigma^2}} \tag{6.3}$$

Parameter A in both equations is found almost equal (A=0.01±0.001) by fitting to the whole range of MRI data.
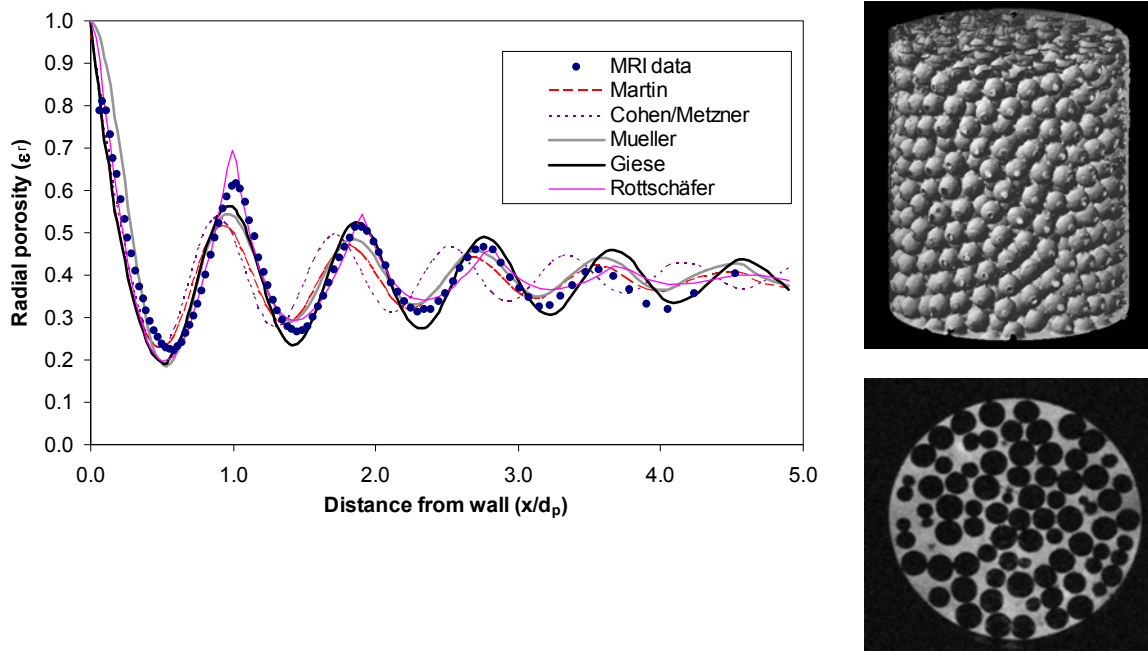
Figure 6.1: Radial porosity distribution in a packed bed of glass beads with $d_p = 2$ mm, $D/d_p = 9.5$. The overall porosity of the packed bed is 0.42. Points are average local porosities evaluated from the 3D-image according to eqs. 5.1 & 5.2. Curves represent values predicted from empirical equations.
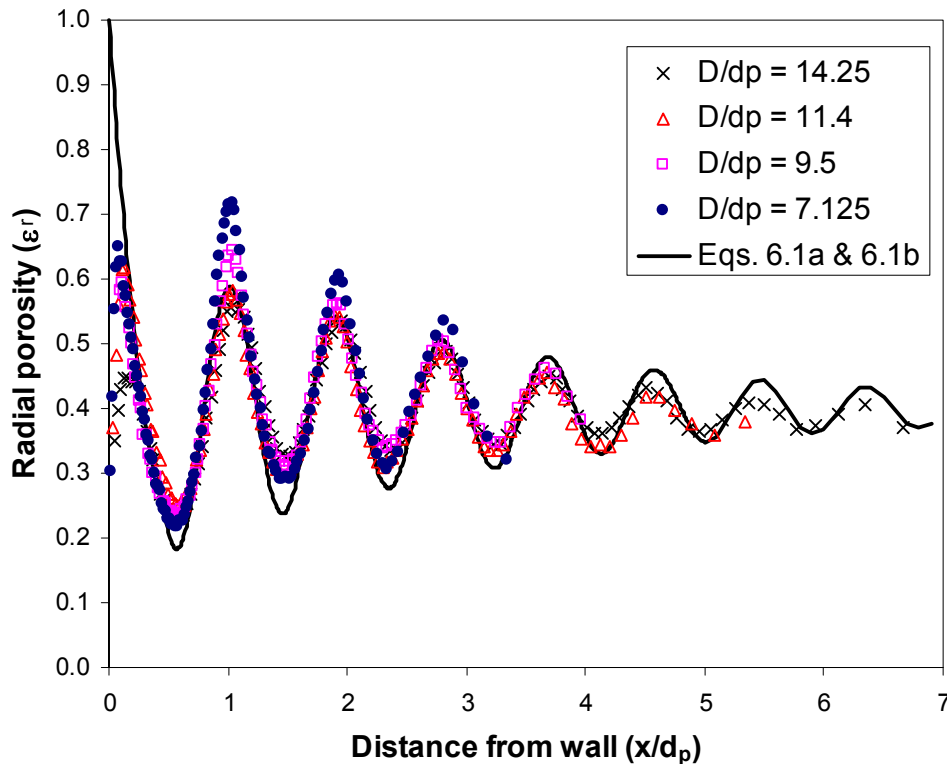

Figure 6.2: Porosity profiles for packed beds of different D/d_p ratios. Solid line represents the prediction for $D/d_p = 14.25$.
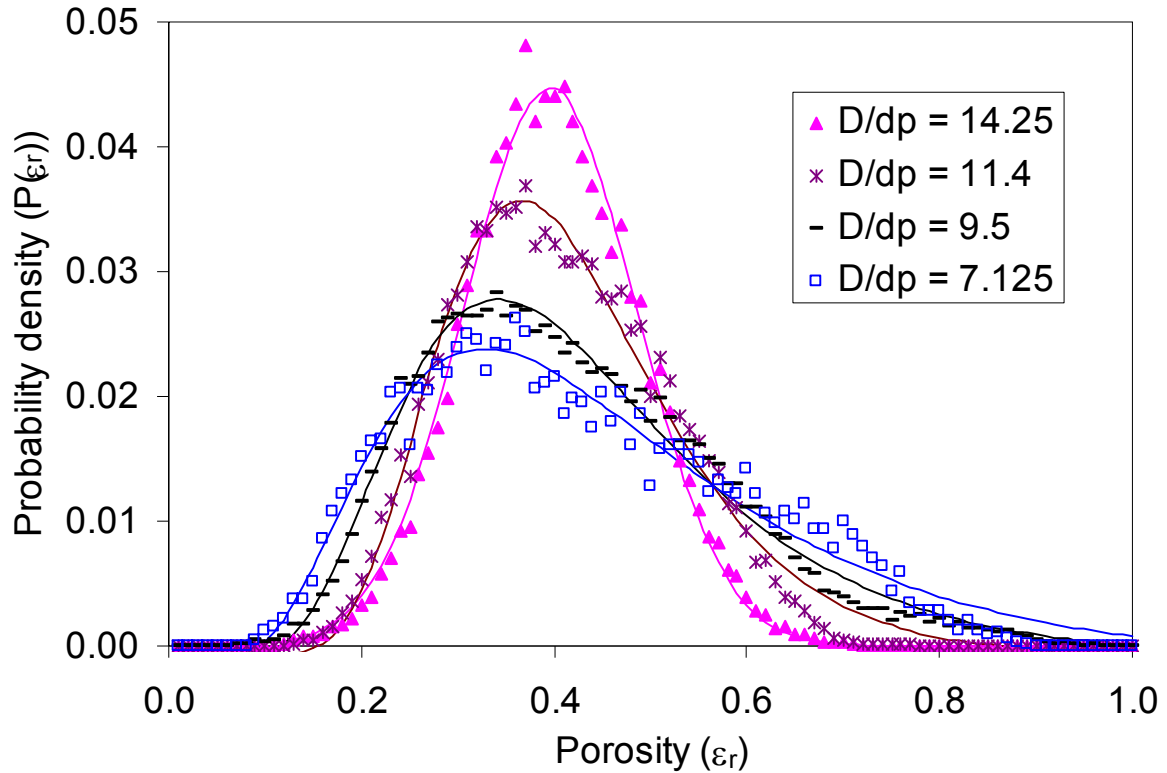
Figure 6.3: Probability density distribution profile of porosity for packings of spheres. Fitted data are presented by curves. Experimental data for D/d_p = 14.25, 11.4, 7.125 are from van Buren [Bur04].

The statistical results are summarized in Tab. 6.3, where ε_b is the measured mean porosity of the packing calculated from 3D-images, σ the fitted standard deviation and AARE the average absolute relative error of the prediction corresponding to the appropriate distribution function listed in the last line of Tab. 6.3. It can be seen that the standard deviations decrease with increasing D/d_p-ratio. This indicates that porosity is more uniform in packed beds with higher D/d_p-ratio than in smaller ones.

D/d_p	14.25	11.4	9.5	7.125
Mean porosity (ε_b)	0.4	0.405	0.42	0.43
Standard deviation (σ)	0.18	0.31	0.41	0.51
AARE (%)	9.5	13	13	17
Distribution function	normal	lognormal	lognormal	lognormal

Table 6.3: Statistical data of spatial porosity distribution of the packings of spheres

b) Packed beds of non-spherical particles

The radial porosity distributions for packed beds of non-spherical particles are shown in Fig. 6.4a. It can be clearly seen that the oscillatory variation of porosity in radial direction decreases gradually from cylindrical particles to raschig rings corresponding to their increasing geometrical complexity. Especially, no significant oscillation is

observed for the trilobe particles due to their high asymmetry and the large D/d_p-ratio of the packing. The radial porosity profiles for the packings of raschig rings were predicted by the correlation of Rottschäfer (eq. 6.4), where the parameters ε_w, c_{max}, c_1, c_2 were obtained by fitting to MRI experimental data.

$$\varepsilon(x_{Fo}) = c_3 \left(c_1 + \sum_{a=1}^{2} \frac{\cos(ax_{Fo})(-1)^a}{a^2} \right) e^{c_2 x_{Fo}} + \varepsilon_b \qquad (6.4)$$

where

$$x_{Fo} = \pi \left(1 + \frac{1}{c_{max}} \frac{2x}{d_p} \right)$$

$$c_3 = \frac{\varepsilon_w - \varepsilon_b}{\left(c_1 - \cos \pi + \frac{\cos 2\pi}{4} \right) e^{c_2 \pi}}$$

for raschig rings 5 mm x 5 mm x 0.5 mm :

$\varepsilon_b = 0.71$; $\varepsilon_w = 0.6$; $c_{max} = 1$; $c_1 = -0.005$; $c_2 = -0.05$

for raschig rings 3 mm x 3 mm x 0.6 mm :

$\varepsilon_b = 0.55$; $\varepsilon_w = 0.45$; $c_{max} = 0.95$; $c_1 = -0.005$; $c_2 = -0.05$

$$\varepsilon_r = 0.8 - (0.8 - \varepsilon_b) \left\{ 1 - e^{\left(-A \frac{x^2}{d_p^2} \right)} \right\} \qquad where \quad A = 10.6 \qquad (6.5)$$

A = 0.45 (0.26) ; B = -0.8 (-0.32) ; C = 1 (1.12) ; D = -0.3 (-0.14) ; T = 0.8 (0.55) ; ε_{min} = 0.23 (0.23)

Table 6.4: Fitting parameters of eq. 6.1a & 6.1b for the packing of cylindrical particles. Values in parentheses are for packings of spheres

Because raschig rings have inner hollow spaces, they exhibit high average bulk porosities ε_b = 0.71 and ε_b = 0.55 for the dimensions of 5 mm x 5 mm x 0.5 mm and of 3 mm x 3 mm x 0.6 mm, respectively. Unlike the pointwise contacts of spherical particles to the wall, non-spherical particles have line contacts, which result in an average porosity at the wall ε_w in all cases below 1. The maximal porosities at the wall for trilobes and for cylindrical particles are approximately about 0.8. Because the oscillatory behaviour of porosity for the packing of cylindrical particles is not much different from that found for packings of spheres, the new equation (eq. 6.1a & 6.1b) can also be applied to predict the porosity profile. The parameters, however, must be adjusted for an optimal fit to experimental data for cylindrical particles as shown in Tab. 6.4. As a matter of fact, the high values of the radial amplitude A, the damping factor B and the oscillatory factor C for the packing of cylindrical particles reduce the oscillations more quickly as compared with packings of spheres. For the packing of trilobes, the radial porosity distribution appears to be uniform in the bulk region. Thus, it can be described by a simple correlation with an exponential function (eq. 6.5),

which consists of only one constant (A = 10.6). All correlations associated with their experimental data result in an AARE within 5%.
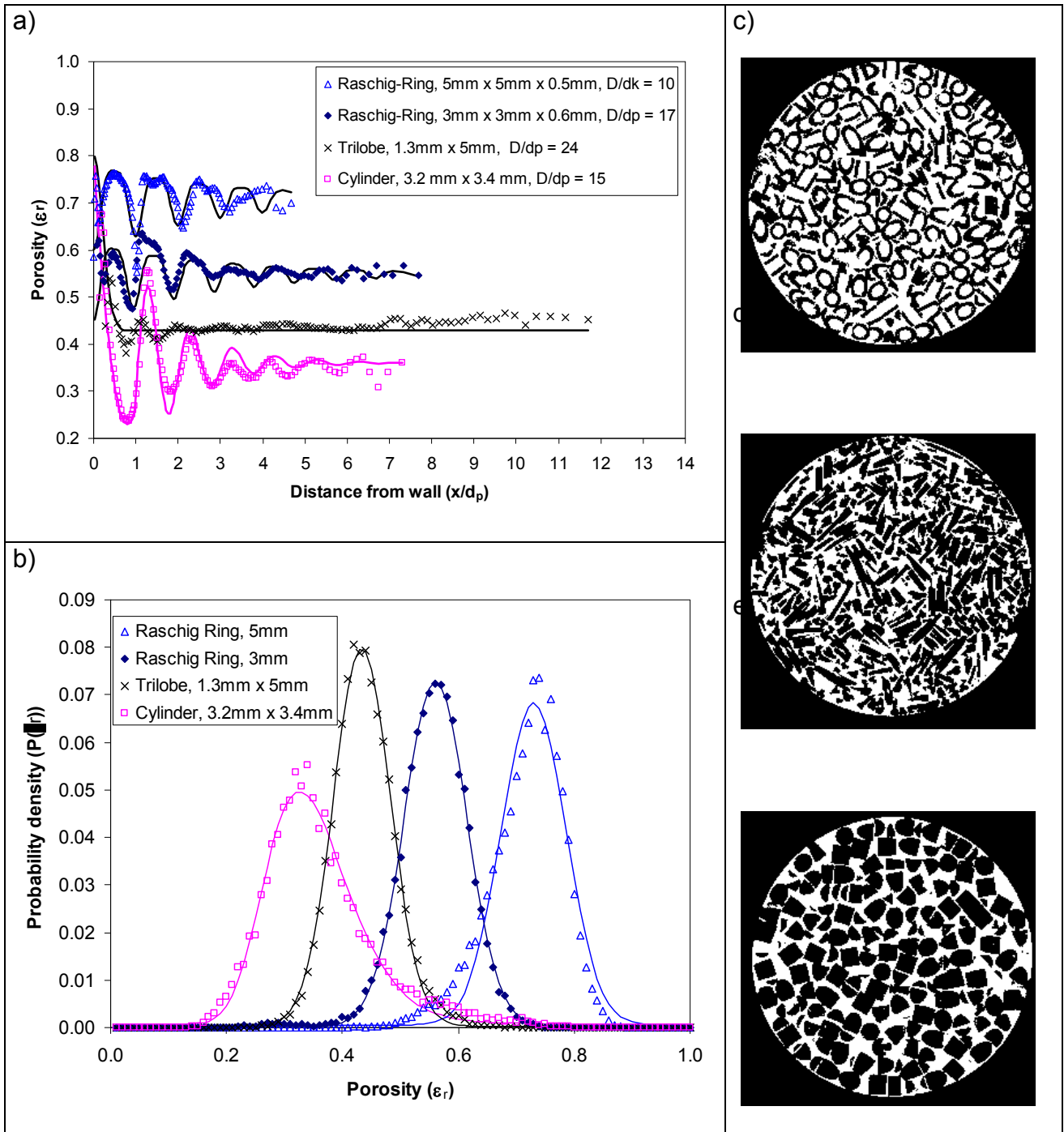

Figure 6.4: a) Radial and b) spatial porosity distributions of packed beds of raschig rings, trilobe and cylindrical particles. Fitted data are shown as solid lines. 2D-slices c), d) and e) extracted from 3D-images of packings of raschig rings, trilobes and cylindrical particles, respectively

57

	Trilobe			Cylinder	Raschig rings	
D/d_p	24	11.2	9.5	15.6	16.7	10
Mean porosity (ε_b)	0.42	0.42	0.43	0.36	0.56	0.73
AARE (%)	13	14	14	13	5.4	16
Standard deviation (σ)	0.098	0.166	0.185	0.216	0.108	0.112
Distribution function	normal	normal	normal	normal	normal	normal

Table 6.5: Statistical data of spatial porosity distribution of the packings of raschig rings, trilobe and cylindrical particles

Although the radial porosity distributions were not uniform for the packings investigated, the probability distributions of the porosity followed a normal distribution pattern (Fig. 6.4b). As seen in Tab. 6.5, the standard deviation has a close relationship to the particle shape and D/d_p-ratio. As expected, the packing of trilobe particles has the smallest standard deviation due its large D/d_p-ratio and complex particle geometry, while the packing of cylindrical particles exhibits roughly the same order of standard deviation as the packing of spheres. The effect of D/d_p-ratio on the porosity distribution is clearly illustrated for the cases of the packings of trilobe particles and raschig rings. They indicate that standard deviation decreases with increasing D/d_p-ratio, which is equivalent to a more uniform distribution of porosity in the packings.

c) Vertical porosity distribution

An example of the longitudinal porosity distribution is illustrated in Fig. 6.5. Here the averaged porosities of cross sections (2D-slices) corresponding to their vertical positions in 3D-images of different packings are plotted. The analysis of all measured packings indicates that the variation of porosity over the bed height appears to be randomly, no matter what D/d_p-ratios the packings have. As shown in Tab. 6.6, the average variation around the mean values ranges from 1.6 % to 3.7 % for the investigated packings.

	Raschig ring 5 mm	Raschig ring 3 mm	Sphere 2 mm	Trilobe 2 mm	Cylinder 3.2 mm
ε_b	0.72	0.56	0.43	0.43	0.36
AARE (%)	1.6	1.6	3.7	2.9	3.4

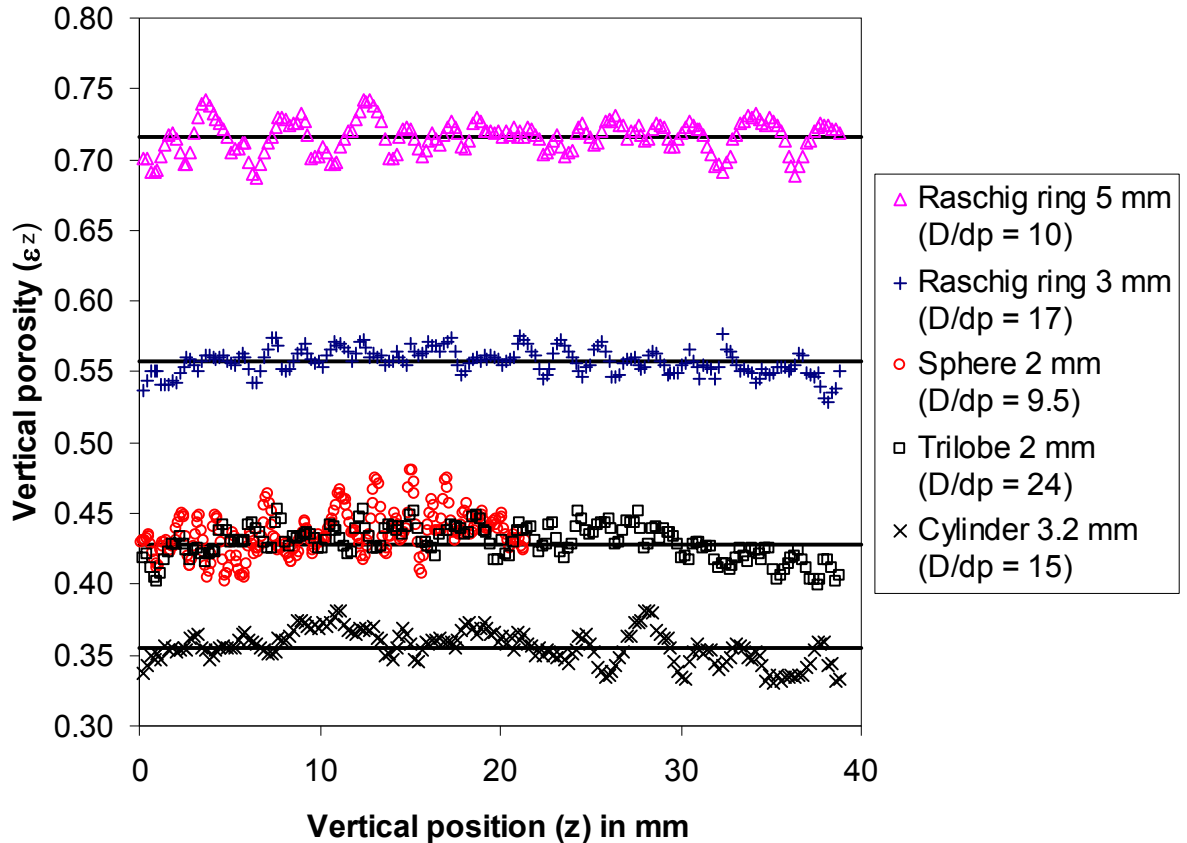**Table 6.6**: Mean porosities of packed beds and their longitudinal variations

Figure 6.5: Vertical porosity distribution of different packings. Lines are average porosities.

6.1.2 Measurements of velocity in packed beds and CFD-simulation

6.1.2.1 Measurements of velocity in packed beds

As discussed in section 6.1.1, many experimental studies and numerical simulations in literature lead to the conclusion that the flow distribution in the packed bed is a function of local bed porosities. In order to examine the relationship between bed structure and flow pattern, measurements of single phase flow of water in a packed bed of spheres were carried out. The bed has an internal diameter of 19 mm, which was filled with glass beads of 2 mm diameter. Fig. 6.6b shows a velocity encoded image acquired for a slice inside the packed bed perpendicular to the axis of the flow column. In this cross sectional area, each pixel intensity corresponds to a quantitative measurement of the z-component of the fluid velocity u_z parallel to the flow direction. As seen in Fig. 6.6a local velocity profiles measured at different superficial velocities u_{0L} (Re$_L$ = 0.24-1.18) follow the same pattern as the porosity profile, except in the region near the centre of the packing where a local velocity maximum is found at the location of minimal porosity. This behaviour is not yet clarified. The highest velocities, which are 2 – 3.4 times as large as the liquid superficial velocities, can be found

close to the wall. Also negative velocities were observed near the spheres' surfaces, where the flow increased along the main flow direction. The occurrence of negative velocities might be explained by the effects of reversed flows and recirculations. Further investigation is required to understand the nature of negative velocities associated with local flow and structure distribution functions. This could be achieved by a combination of MRI measurements and solutions of the Navier Stokes equations using CFD simulation of three dimensional velocity distribution in a packed bed.

The same results of local flow pattern in packed beds were also reported from other experimental studies applying MRI-technique [Hei04, Ren03, Sed97, Kut96, Sue03]. As a consequence of the inhomogeneous flow in laboratory reactors with small tube-to-particle ratios (D/d$_p$), deviations from ideal plug flow must be considered.

From the local velocity data in the image slice, the volume flow rate through the cross section can be calculated from:

$$^{V}\Phi_{L} = \sum_{i} u_{z,i} n_{i} a_{0}$$ (6.6)

where u$_{z, i}$ is the measured velocity parallel to the flow direction, n$_i$ is the number of pixels containing u$_{z,i}$ in the slice and a$_0$ is the area of a pixel.

Fig. 6.7 shows the fraction of volume flow ($^{V}\Phi_L/^{V}\Phi_{L,0}$) as a function of the fraction of the void space (V$_H$/V$_{H,bed}$) based on the measured data in Fig. 6.6a. For a perfect homogeneous flow pattern where the pores' system in the packed bed has the same flow rate a straight line from (0, 0) to (100, 100) would be observed. In this case, it is clearly recognized that a polynomial trend in the measured data set exists. That means a significant heterogeneity in liquid flow in the packed bed. As the curve approaches 100% at the void fraction of 85%, about 15% of void space is occupied by stagnant fluid (having zero velocity) staying at the surfaces of particles and around contact points between adjacent particles. The results suggest that simulations of packed beds with low tube-to-particle ratios cannot be simplified in a one-dimensional model.

The sum of the velocity component in each pixel of the axial velocity image multiplied by the area of that pixel is the volumetric flow rate, which is given by eq. 6.6. Volumetric flow rates calculated in this way are compared to flow rates measured at the pump in the parity plot, Fig. 6.8. The result shows that flow rate values calculated from the velocity image are within 10% of the values measured at the pump.
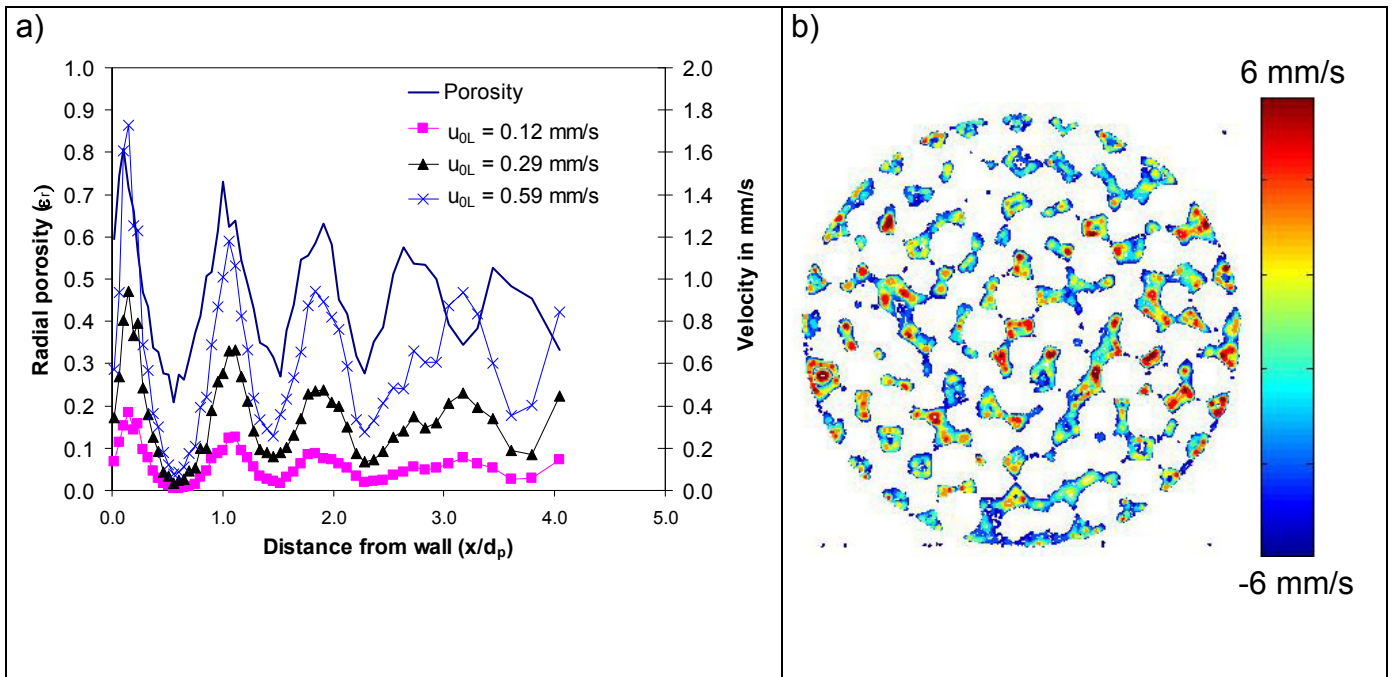
Figure 6.6: a) Porosity and velocity profiles of a packing of 2 mm glass beads in a 19 mm column, b) the velocity encoded image with the resolution 84 μm x 84 μm, superficial velocity of water is 0.29 mm/s. Solid phase is shown as white colour inside the slice.
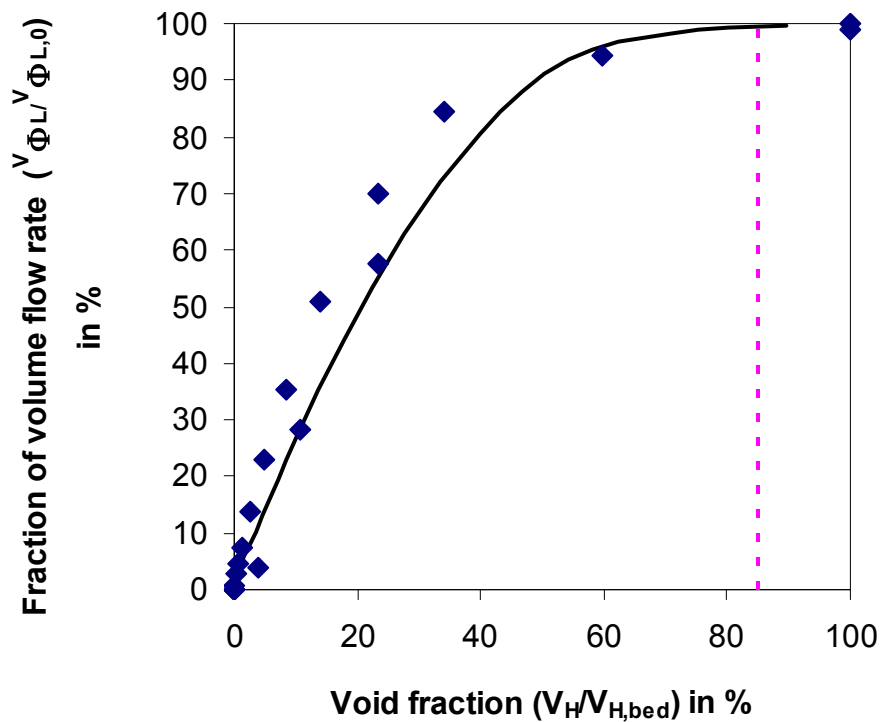

Figure 6.7: Water flow rate as a function of the void volume in the packed bed of spheres. The trend of the measured data is shown as solid line. Total liquid flow passes through approximately 85% of void area as indicated by dotted line.
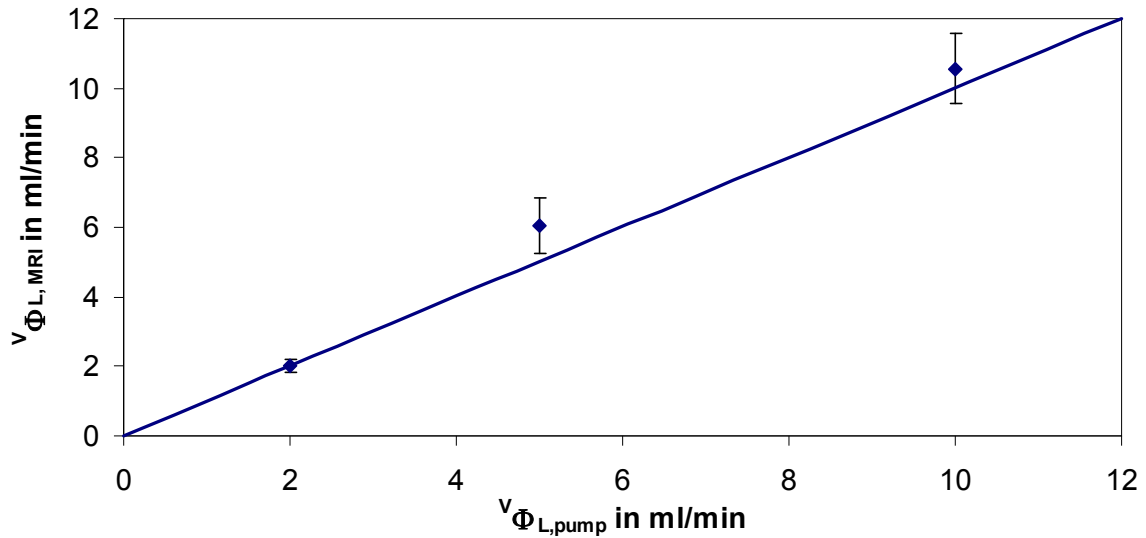
Figure 6.8: Comparison of volumetric flow rates obtained from 3 images of the axial velocities in the packing of spheres and flow rate measured at the pump (parity plot).

6.1.2.2 CFD simulation

Computational fluid dynamics is a well-established tool for several areas of chemical engineering. However, for fixed bed reactors, geometric complexity has so far prevented detailed modelling of their hydrodynamics. In most cases, a packed bed of solid particles can be modelled as an isotropic or anisotropic porous media. CFD based models, applied to simulate flow in trickle bed reactors, have used a statistical description of the porosity structure in the flow model [Jia02, Gun03; Arr04]. The authors used a porosity model partitioning the 3D-packed bed into small sections and to each section a porosity distribution was assigned. Depending on the section size chosen for partition, the section porosity values follow a certain probability density function, which has already been discussed in chapter 6.1.1.

This work, however, attempts to use the geometrical data of packed beds obtained from MRI-measurements to generate real bed geometries in a CFD program (Fluent 6.0 from Fluent. Inc., USA) and to simulate the single phase flow. The major objective of this study is to combine experimental and computational techniques in order to examine how local flow hydrodynamics are affected by the bed structure in subparticle scale. The detailed information about the fluid dynamics around particles in the bed (local scale) can then be calculated to global values of lumped parameters (bed scale) and is compared with measured data from MRI experiments.

The first step of this work is to implement detailed geometrical information of randomly packed beds obtained from MRI measurements in the CFD simulation model. Usually, the built-in tools of commercial CFD pre-processors are employed to create a representative geometry model and to generate an appropriate grid for the simulation. However, these tools are not successfully applied for the complex bed

geometries with a large number of packing elements in the bed. It is, therefore, necessary to develop an appropriate advanced geometry modelling tool for implementation of 3D MRI-data. It must be mentioned here that geometry modelling and subsequent grid generation are time-consuming processes which account for more than 60% of the total time of a CFD project. In this work, two approaches were developed to import the geometry information of 3D-images for simulation. The first approach is applied for packed beds of spheres and the second for packed beds of particles of other shapes, such as trilobes, raschig rings, cylinders. The MRI-data were first binary gated to yield a data set consisting of numerical values of 1 representing the solid phase and zero for the void places in the packed bed. For packed beds of spheres, the middle points of every spheres in every slice extracted from 3D-images were determined as shown in Fig. 6.9 a) by using a specific algorithm. To do this, the solid phase in the binary image was first filtered in such a way that only voxels at the surfaces of spheres remained. Then, the distances between every two neighbour surface voxels were measured. Only the distances which equaled to the sphere diameter (in this case d_p = 2.0 mm) were chosen to determine the middle points of the corresponding spheres. Their coordinates and radii were then used as input data for a geometry modelling tool (in this case Gambit 2.0) to reconstruct a full 3D packed bed. This approach, however, has a disadvantage. Some spheres in the bed contact each other, that causes poor quality grids leading to numerical divergence. To overcome this problem, a simple algorithm was developed to detect the contact points in the bed. Here a small gap between the neighbour spheres at every contact point should be introduced by carefully shifting the positions of the respective spheres. For packed beds of non-spherical particles, the second approach can be employed by using the available geometry modelling tool (Gambit) to import directly geometry data of a binary slice into the structured grids. An example of this approach is illustrated in Fig. 6.9 b). This method is simple, but requires a large number of computational cells. Due to computer memory restriction, the length of packed beds of non-spherical particles (trilobe particles) used for 3D-simulation is limited to 5 mm.

After a geometry model has been created, it is necessary to generate appropriate grids over the solution domain (i.e. particle surfaces and void areas) for numerical simulation. Unstructured grids were applied for packed beds of spheres. A finer grid should be used in the regions where strong variations are expected to occur, i. e. at the near wall region, particles' surfaces, small gaps between particles. For packings of non-spherical particles, the structured grids were already created by importing geometry data from MRI-images. They also needed to be refined in the vicinity of the particles in order to ensure numerical stability. An advantage of structured grids is that solvers are generally faster for their algebraic equation system than for unstructured grids.
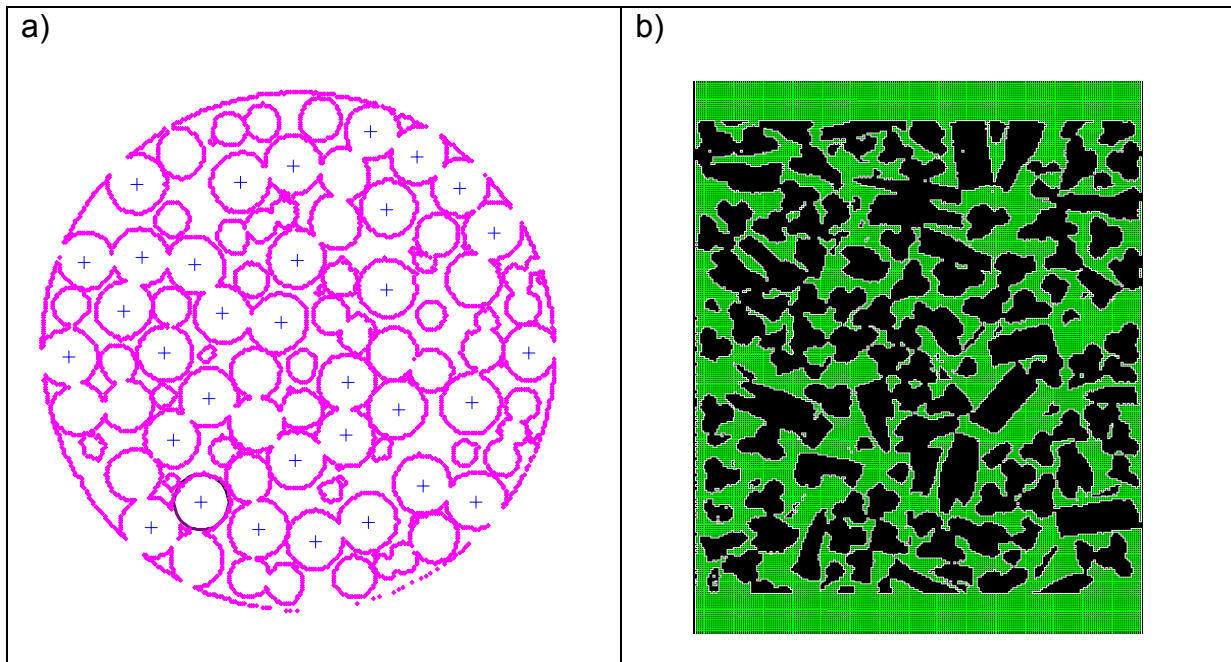
Figure 6.9: a) Middle points (+) of spheres of 2 mm in a cross section extracted from a 3D-image of a packing of 19 mm. b) geometry model generated from a 2D vertical slice of a packing of trilobes with 256 x 256 grid structure. Pixel resolution is 89μm x 89μm. Solid phase is shown as black colour.

When a sufficiently accurate mesh has been generated, numerical simulation can be performed. The commercial package Fluent 6.0 was used to solve the Navier – Stokes equations for conversation of mass and momentum. The basic equations and the background of the balances are stated in Fluent handbook [Flu03].

The capability of the CFD simulation to predict flow profiles can be demonstrated by performing the simulation of the single phase flow in a representative geometry of a 3D-bed of spheres (D = 46.5 mm, d_p = 6 mm) extracted from the full MRI data set. Because the computer memory is restricted, a packing containing only 100 spheres were built in the CFD model. The resulting unstructured mesh contained about 800000 computational cells and required approximately 10 minutes of CPU time on PC Intel Pentium M Processor 1.6 GHz for a solution of laminar flow.

A selection of the axial velocities u_z in a cross sectional area is shown in Fig. 6.10b. It is interesting to note that the maximum in the average velocity does not coincide with the maximum in the porosity, but at about 0.1 particle radii. This is due to a no-slip condition at the wall for the simulation. As a whole, the radial velocity distribution follows the same pattern of porosity distribution (Fig. 6.10a), which is qualitatively comparable with the experimental data (Fig. 6.6a). Because the available experimental velocity data were gathered for a different packing of spheres (D = 19 mm, d_p = 2 mm), this CFD model cannot be sufficiently validated yet. It can, however, be concluded that CFD simulations produce qualitatively the same features of flow pattern observed by MRI. The results would contribute a step forward in understanding the detailed local hydrodynamics in complex packed bed reactors.
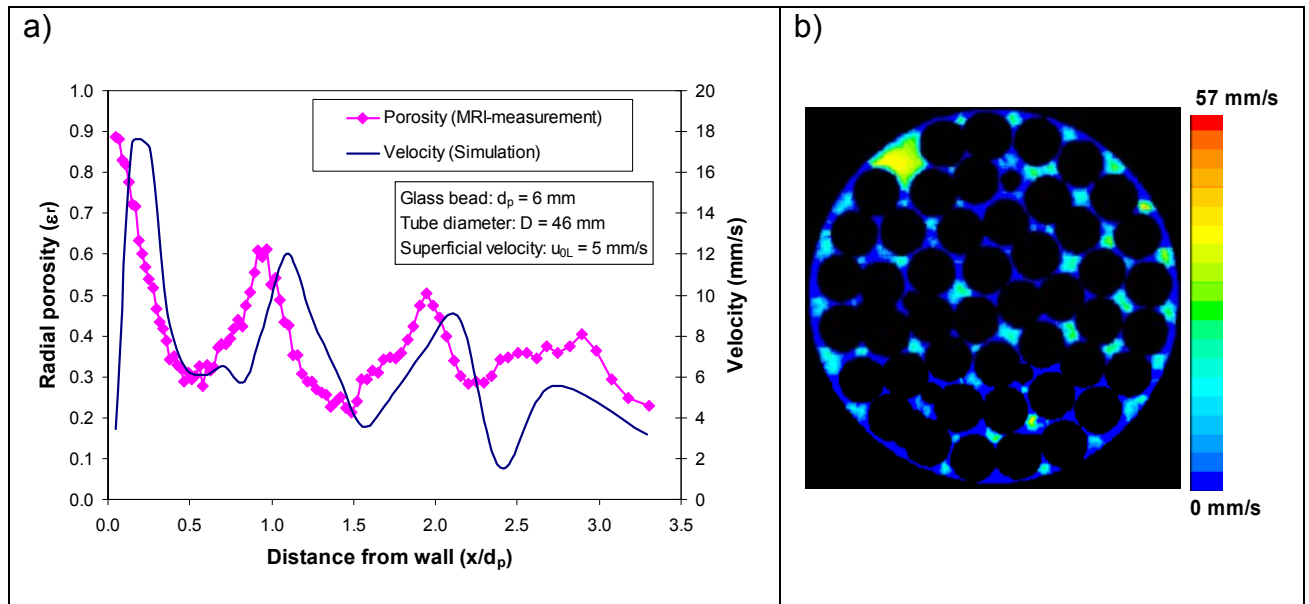
Figure 6.10: a) Fluent 3D-simulation of single phase flow of water in a packing of spheres, u_{0L} = 5 mm/s. Radial porosity, ε_r, distribution was calculated from data of a slice extracted from a 3D-image. Radial average of u_z-velocity is calculated from simulation data b) Distribution of u_z-velocity component parallel to the flow direction in a cross section. The packing was reconstructed in Fluent by using the geometrical data from MRI-image. The packing has a diameter of 46.5 mm filled with glass beads of 6 mm.

Because most of previous CFD studies have paid attention only on packed beds of spherical particles, it is worthwhile to study how CFD model can be applied for non-spherical particles relevant to practical use in industry. An attempt is made here. A test case of the 3D simulation of single phase water flow at superficial velocity u_{0L} = 5 mm/s in a packed bed of trilobes is demonstrated in the following Fig. 6.11. The geometry model reflects the actual packing structure of 30 slices extracted from a MRI 3D-image of a packing of trilobes (d_p = 2 mm). Each slice consists of a 119 x 128 x 1 matrix, giving cells with spatial resolution of 175 μm x 175 μm x 175 μm. In order to generate meaningful results and numerical stability, the structured grids should be refined to obtain an optimal mesh density. After refining the mesh, the whole computational domain (i.e. the bed including inlet and outlet regions) consisted of approximately 2150000 computational cells and required about 45 min of run-time for a solution of laminar flow.

Fig. 6.12a shows radial profiles of measured porosity of xy-slice (Fig. 6.11a) and simulated velocities at different superficial velocities. It is clearly seen that the high velocity zones do not match with the high voidage regions as they would be expected in the case of simulation for the packing of spherical particles (Fig. 6.11a). This could be explained by the geometrical difference between of spherical and trilobe particles and their arrangement in the packings. In general, the spheres form an ordered packing than that of trilobes. This results in a higher complexity of pore systems, which create small channels (rivulets), in packing of trilobes than that in packing of

spheres. The existence of complex channelling flow in the packing is therefore responsible for the local velocity variations through the cross section shown in Fig. 6.11a.

It is interesting to see that the locations of high and low velocities do not change with increasing liquid superficial velocities. A quantitative evaluation of the radial velocity distribution in Fig. 6.12a indicates that the velocity profile for u_{0L}= 0.5 mm/s after multiplying by 10 is almost identical to the velocity profile for u_{0L} = 5 mm/s. It can be concluded that the local velocities proportionally increase with the increasing liquid flow rates, and therefore the flow pattern does not significantly change in the range of simulated superficial velocities. The same flow behaviour can also be observed from MRI-experimental measurements for the packing of spheres (Fig. 6.6a).

In order to quantify how the overall porosity and velocity profiles change over the whole bed, the average values of radial porosities and velocities from 30 slices of the packing were calculated. Although the overall porosity profile (except the wall region) tends to homogenously distribute (Fig. 6.12b), the fluctuation of radial averages of velocities remains high. This implies that the channelling effect is still dominant within the whole bed.
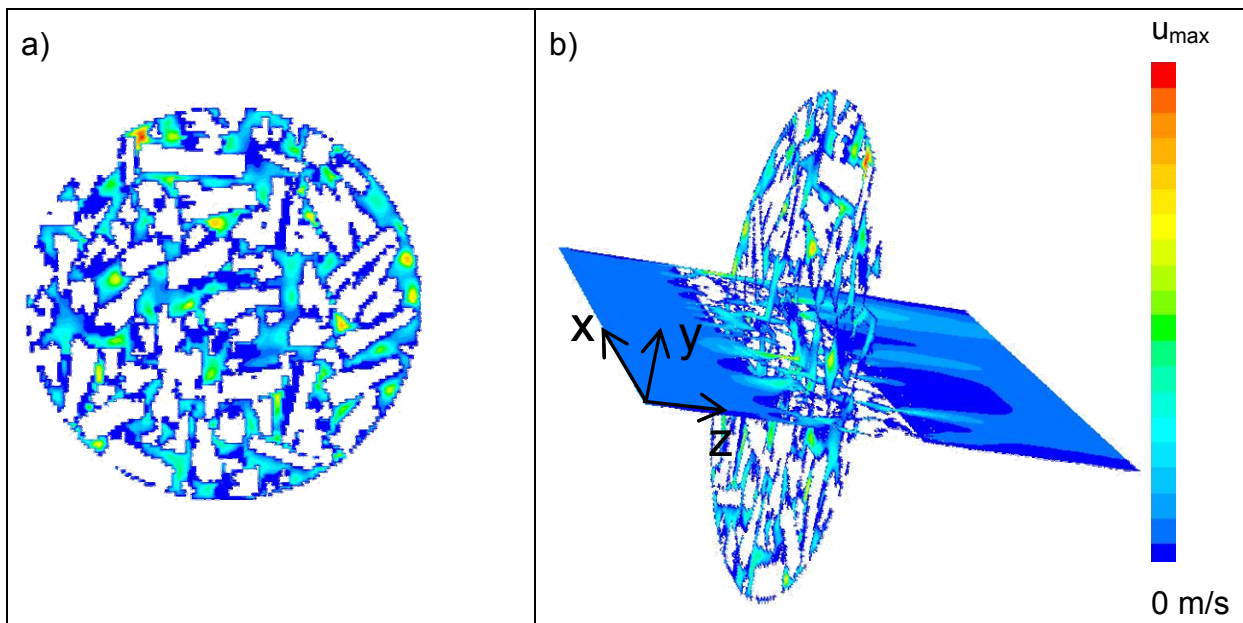

Figure 6.11: Simulation of water flow at u_{0L} = 5 mm/s in a 3D-packed bed of trilobe particles (d_p = 2 mm). Axial velocity distribution is displaced in a) a cross section (xy-slice) in the middle of the packed bed perpendicular to the flow direction (z-axis) and in b) two orthogonal slices, where xz-slice is parallel to the flow direction. The packed bed has a length of 5 mm consisting of 30 horizontal slices extracted from a 3D-image. The scaling velocity is indicated by the colour bar. Maximum velocity, u_{max} is 68 mm/s.

Figure 6.12: a) Radial porosity profile in xy-slice calculated from MRI-data and radial average of locally axial velocities obtained from Fluent® 3D-simulation of the single phase flow of water b) Comparison of variations of radial porosity profile and velocity profile in one slice and in the whole catalyst bed
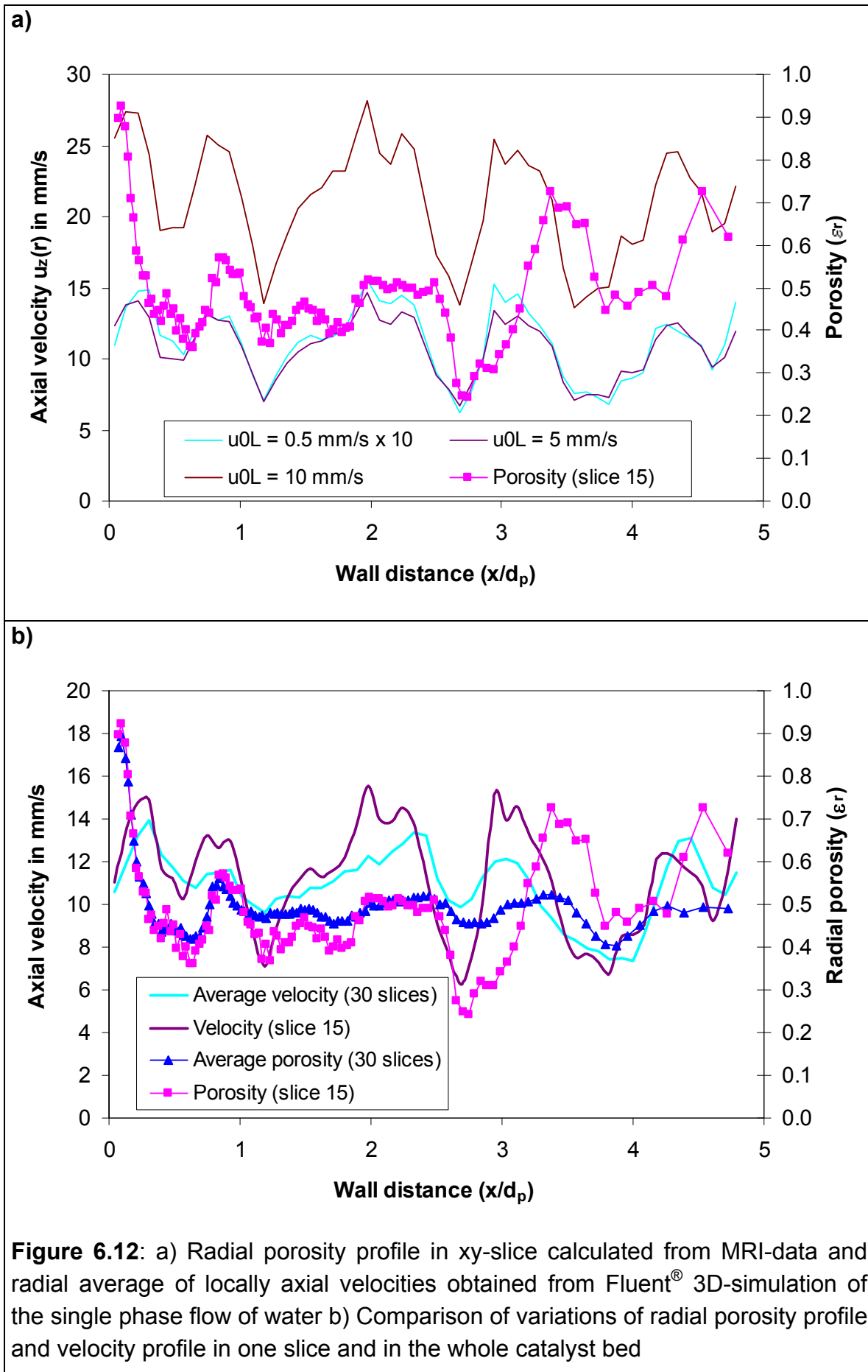
6.1.3 Measurements of liquid saturation and wetting efficiency

As mentioned in chapter 5.1, the gas-liquid distribution in packed beds during two-phase flow experiments was mostly probed in 3D images, that provide sufficient information to evaluate the hydrodynamic behaviour quantitatively. The results presented in this section are based on MRI measurements for gas/liquid distribution in packed beds of spheres and trilobes under atmospheric conditions and at elevated temperatures and pressures. All the acquired 3D-images of the packed beds were taken with typical matrixes of 128 x 128 x 128 or 256 x 256 x 256 data points, which yield isotropic volume element (voxel) resolution of 168^3 μm^3 or 89^3 μm^3, respectively for the field of view of 21.5 x 21.5 x 21.5 cm^3.

6.1.3.1 Static liquid saturation

For static liquid measurement, the packings were first flooded in order to remove all small air bubbles trapped in the void areas. The liquid was then allowed to drain for at least 5 hours, so that only liquid remaining at contact points and at surfaces of particles was present in the packings. The 3D-images of the packings, acquired at such conditions, were then analysed to determine the static liquid saturation. Fig. 6.13a shows the radial distribution of porosity and static liquid saturation of two packings of spheres and trilobes, respectively. It can be seen that the variation of both static liquid saturation and porosity for the packing of spheres is stronger than that for the packing of trilobes. Except the region close to the centre of the packing, the curve of $\beta_{st,r}$ exhibits local maxima at positions, where the porosities have minimal values. On contrary to $\beta_{st,r}$, the static liquid holdup ($h_{st,r}$) profiles are similar to that of porosity profiles (Fig. 6.13b). The average values of static liquid holdup for both packings, however, are as small as 1/10 of those of porosity. Because $\beta_{st,r}$ is proportional to static liquid holdup and inversely proportional to porosity according to eq. 2.4, the influence of porosity's variation on $\beta_{st,r}$ is therefore stronger than that of static liquid holdup. This means that the curve of $\beta_{st,r}$ follows the opposite trend as compared with porosity's curve (Fig. 6.13a).

In comparison between two packings, it is clear that both ε_r and $\beta_{st,r}$ values of the packing of trilobes are more uniformly distributed than that of packing of spheres. The average values of $\beta_{st,b}$ for the whole bed are of 0.09 for packing of spheres, and of 0.1 for packing of trilobes.
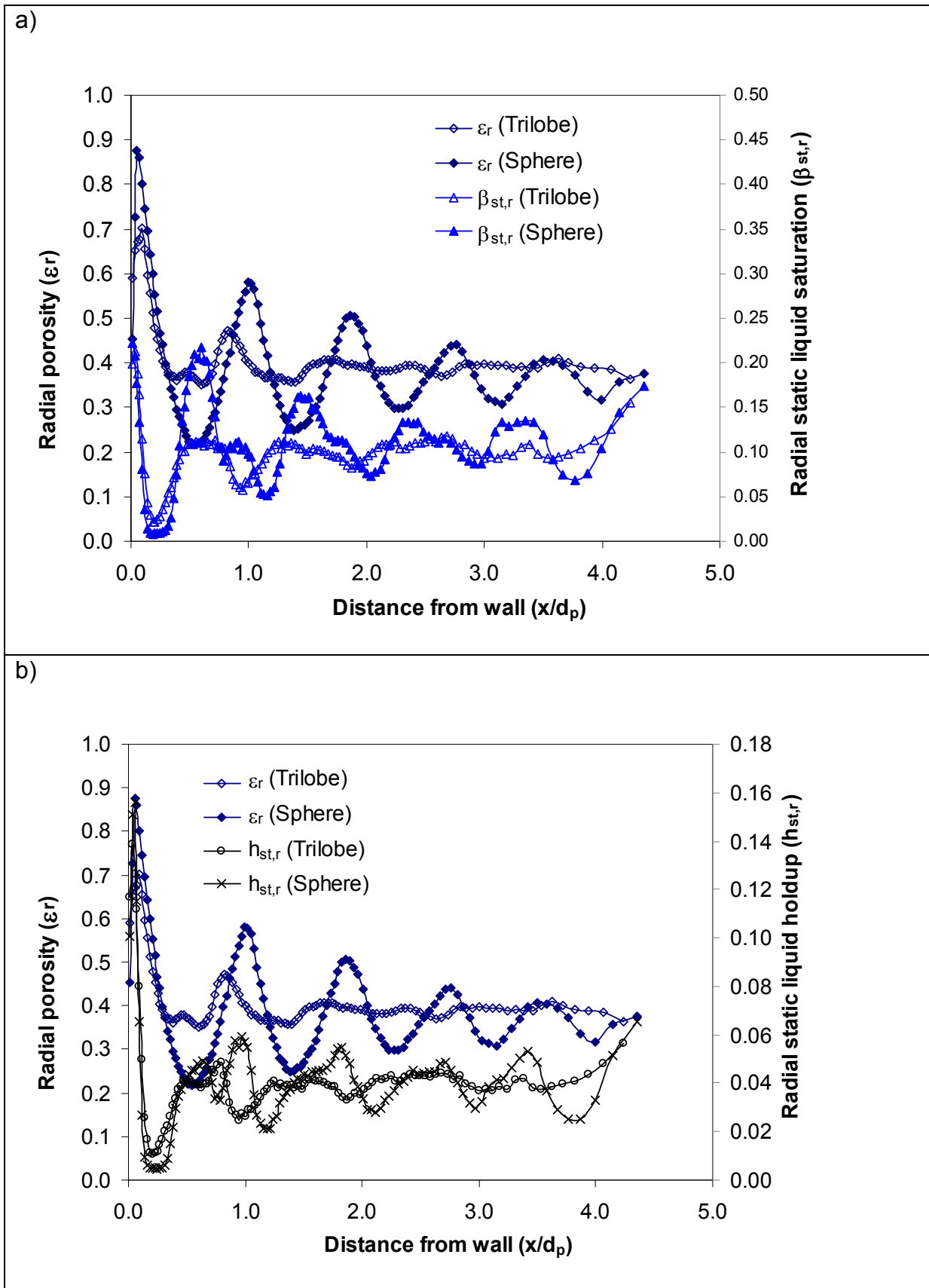
Figure 6.13: a) Radial distribution of porosity and static liquid saturation b) Radial distribution of porosity and static liquid holdup calculated from 3D-images of two packings of spheres and trilobes, respectively. Both packings have the same inner diameter D = 19 cm, and consist of particles with d_p = 2 mm.

Contrary to radial distribution of porosity and static liquid saturation, the variation of these values and wetting efficiency in longitudinal direction (z) is almost randomly distributed (Fig. 6.14). In order to estimate how the porosity distribution affects the variation of static liquid saturation along the bed, the correlation of Turner [Tur59] (eq. 6.7) was used to calculate β_{st} values as illustrated by a solid curve in Fig. 6.14. This empirical correlation establishes the relationship between the $\beta_{b,st}$ and the Bo number, which represents the ratio of the gravitational and the capillary forces. However, the correlation does not give a good fit of the experimental data. The mean relative deviation between the experimental and the correlated values vary from $\pm$ 1% to $\pm$ 55%. It is evident that a high non-uniformity in liquid distribution occurs in the bed. Moreover, the effect of this non-uniformity could be quantified by comparing the values of standard deviation of porosity, static liquid saturation and wetting efficiency. In this case, the standard deviation of β_{st} and η_{ce} is of 18%, more pronounced than those of porosity distribution (5%)

$$\beta_{b,st} = \frac{1}{\varepsilon_b \left(\dfrac{1}{0.035} + \dfrac{Bo}{0.707} \right)} \quad with \quad Bo = \frac{\rho_L g d_p^2}{\sigma} \tag{6.7}$$
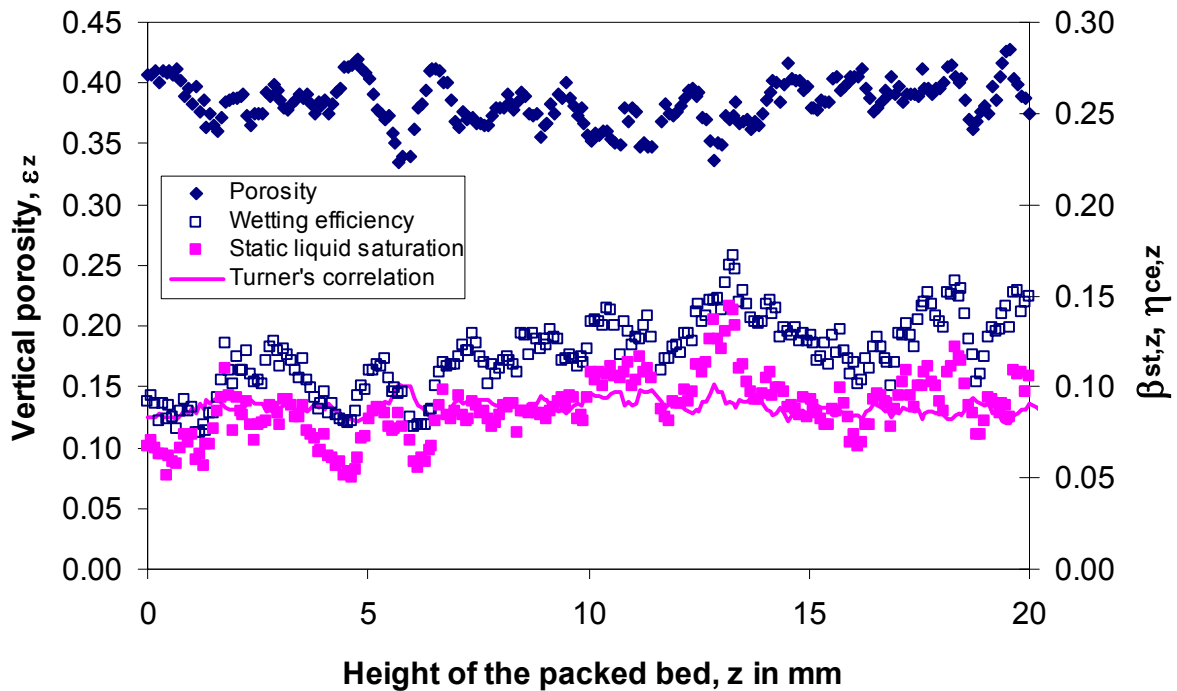

Figure 6.14: Vertical distribution of porosity and static liquid saturation calculated from a 3D-image of the packing of trilobes (D = 19 mm, d_p = 2mm). Voxel resolution is 89^3 μm^3. Solid line represents static liquid saturation values, which are calculated according to Turner's correlation [Tur59].

The mean values of static liquid saturation $\beta_{b,st}$ was obtained by averaging the local values of β_{st} in the whole bed. The $\beta_{b,st}$ values presented in Tab. 6.7 for different packing properties and gas/liquid systems are plotted in Fig. 6.15 as functions of the Bond number.

G/L-system	Packing	d_p (mm)	T (°C)	ρ (g/cm^3)	σ (mN/m)	ϕ	μ (Pa.s)	$\beta_{b,st}$
Air/ PEG 5%	Trilobe	2	25	1.01	65.0	0.61	0.00127	0.088
Air/ PEG 50%	Trilobe	2	25	1.07	60.0	0.61	0.00867	0.096
Air/ Water	Trilobe	2	25	1.00	71.95	0.61	0.00089	0.096
Air / Diesel	Trilobe	2	25	0.86	26.9	0.61	0.00378	0.089
Air / Diesel	Trilobe	2	25	0.86	26.9	0.61	0.00378	0.085
Air/ PEG 50%	Trilobe	2	25	1.07	60.0	0.61	0.00867	0.084
Air/ Water	Sphere	2	25	1.00	71.95	1.00	0.00089	0.085
Air/ Diesel	Sphere	2	110	0.86	20.6	1.00	0.00103	0.081
Air /Diesel	Sphere	2	25	0.86	26.9	1.00	0.00378	0.072
Air /Diesel	Sphere	2	25	0.86	26.9	1.00	0.00378	0.075
Air /Diesel	Sphere	2	25	0.86	20.6	1.00	0.00103	0.076

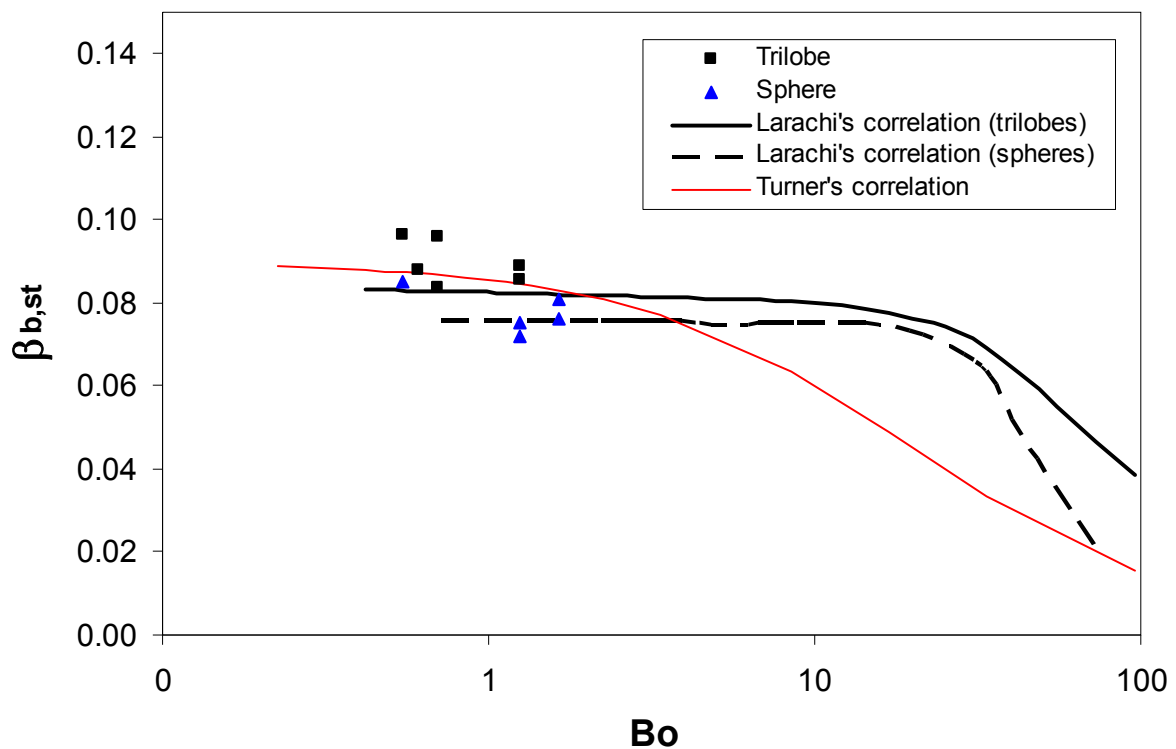**Table 6.7**: Experimental data for measurements of static liquid saturation

Figure 6.15: static liquid saturation $\beta_{b,st}$ as functions of Bond number. Comparison between experimental data with those calculated by correlations

These experimental data were then used to compare them with those calculated by the correlations proposed by Turner [Tur59] (eq. 6.7) and Larachi [Arr03]. Larachi's correlation combines artificial neural networks and dimensional analysis to fit a large amount of published data for $\beta_{b,st}$ in the literature. It takes into account the non-spherical effects via the sphericity factor (ϕ), which effects mainly the difference between the two curves of the packings of spheres and trilobes, respectively (Fig. 6.15). It can be seen that, up to a Bo number of ca. 2, which falls almost in the range of the measurements, two correlations give a good fit to experimental data. The $\beta_{b,st}$ values of packing of trilobes are slightly higher than that of packing of sphere. However the differences among them are not significant.

6.1.3.2 Dynamic liquid saturation and wetting efficiency

a) Local distribution of dynamic liquid saturation

Due to limitation of conventional measurement techniques such as tracer and draining methods, in most models reported in the literature hydrodynamic parameters of trickle beds like bulk liquid saturation β_b and bulk wetting efficieny $\eta_{b,ce}$ are predicted from lumpy, full scale experimental data. Since the MRI technique can provide full 3D-images of the liquid phase distribution in the packed beds, it is capable to quantify the hydrodynamic parameters in both local and bed scales.

Typical examples of radial distribution of dynamic liquid saturation are shown in Fig. 6.16a and Fig. 6.16b for two packed beds of spheres and trilobes, respectively. The experiments were carried out with water and air at different liquid superficial velocities but with a constant superficial gas velocity of 21 mm/s during trickle flow regime at atmospheric condition. It is visually observed in Fig 6.16c and Fig 6.16d that the gas and liquid phases in both packed beds were not homogeneously distributed. By applying the data analysis described in chapter 5.1.4 to these images the radial distribution of dynamic liquid saturation was determined.

As seen in Fig. 6.16a, the $\beta_{d,r}$ values for the packing of spheres increase continuously towards the center of the bed. A similar trend is also observed for the packing of trilobes (Fig. 6.16b), except the relative high β_d values near the wall. It is like in the case of static liquid saturation (Fig. 6.13), radial distribution of liquid phase is a strong function of porosity. Due to the highly oscillatory variation of porosities in radial direction for the packing of spheres, the change of its $\beta_{d,r}$ values is locally higher than that for the packing of trilobes. The strong increases of liquid saturation profiles towards center of the bed for both packings indicate that the distribution of local liquid volume inside the bed is increasingly inhomogeneous at high liquid flow rates.
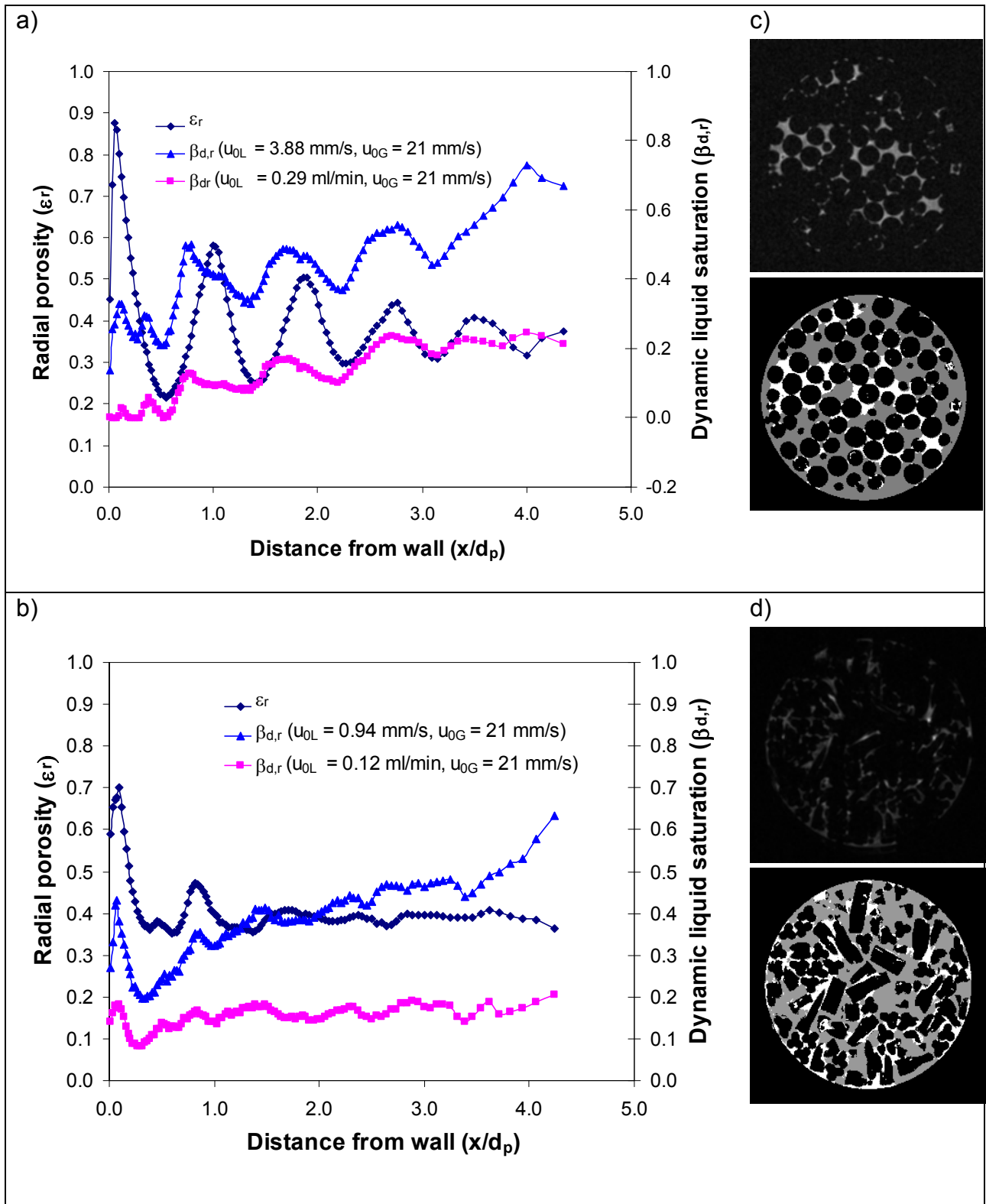
Figure 6.16: Radial distribution of dynamic liquid saturation and porosity in packings of a) spheres and of b) trilobes. c) and d) 2D-images extracted from 3D data sets were taken during water/air trickle flow at liquid superficial velocities of 0.29 mm/s for the packing of spheres and 0.12 mm/s for the packing of trilobes. Gas superficial velocity was set constant u_{0G} = 21 mm/s for all experiments. In-plane pixel resolution is 89 μm x 89 μm.

The inhomogeneity in liquid distribution gives the evidence for "channelling" of flow occurring within the beds, in which liquid flows dominantly in distinctively paths through the bed, so-called rivulets. Sederman and Gladden [Sed01] applied MRI measurements for gas-liquid distribution and developed an image analysis algorithm to characterize the pore system and the liquid rivulets within the beds. They found that the liquid saturation and number of the rivulets increase with liquid flow rate during the trickle flow regime. When liquid velocity reaches the critical value, at which the transition between trickle and pulse flow regimes occur, additional liquid flow no longer contributes to the formation of new rivulets but is taken up in increasing the size of existing rivulets.

Fig. 6.17 shows an example of vertical distribution of porosity and dynamic liquid saturation for a packed bed of spheres. Based on the these measured $\beta_{d,b}$ values, the averaged liquid velocities through cross sectional areas of the packed beds at stationary flow condition could be calculated using the following equation.

$$u_{L,z} = \frac{{}^{V}\Phi_{L}}{A_{0}\varepsilon_{z}\beta_{d,z}} = \frac{u_{0L}}{\varepsilon_{z}\beta_{d,z}} \qquad (6.8)$$
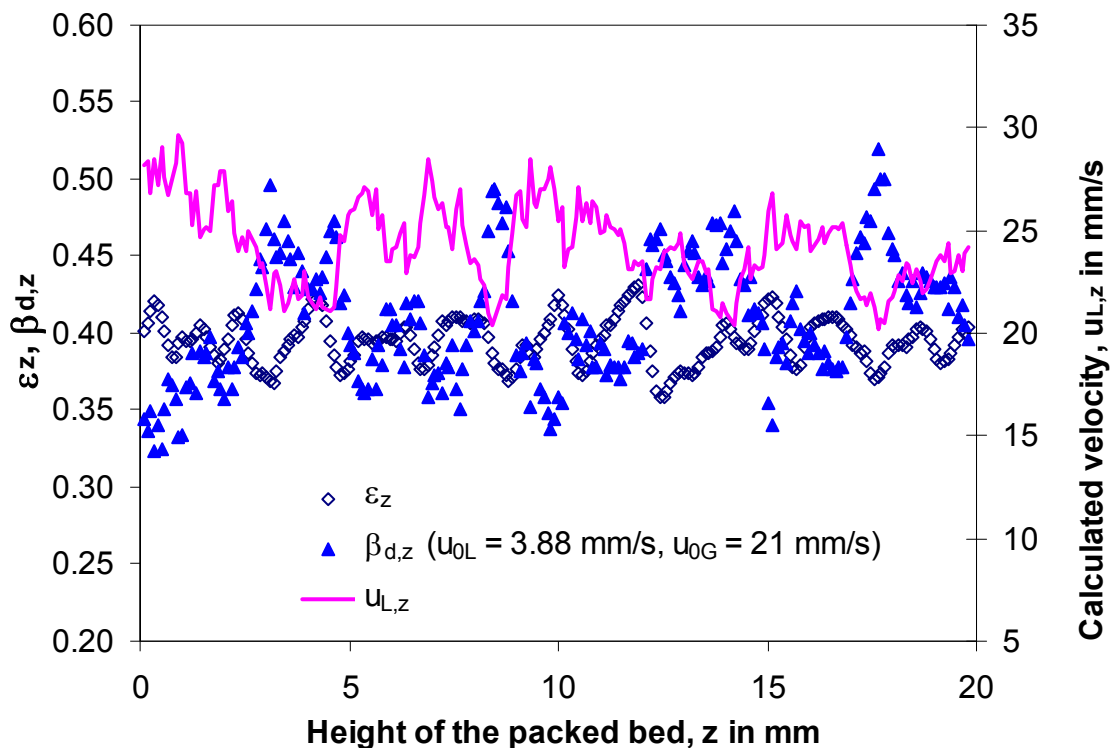
Figure 6.17: Vertical distribution of dynamic liquid saturation, $\beta_{d,z}$ and vertical porosity, ε_{z} in a packing of spheres (D = 19 mm, d_{p} = 2 mm). Experiments with water/air system were carried out at atmospheric condition.

The results are illustrated as a solid line in Fig. 6.17. It should be mentioned that some attempts in this study have been made to map the velocity distribution in the packed beds during two phase flow, but without success. The velocity images

acquired during two-phase flow in the packed bed have in most cases a very low signal to noise ratio, that makes the subsequent analysis of the obtained raw data very difficult. Therefore, no quantitative relationship between velocity and structure can be established. Future work will have to be focussed on developing MRI methods that allow to visualize the flow pattern under two phase flow conditions. The obtained information will be valuable to understand the complex hydrodynamics of multiphase flow systems.

The heterogeneities of bed porosity and dynamic liquid saturation can be quantified by means of statistical parameters (i. e. mean relative deviations) for the whole packed beds as presented in Tab. 6.8. Although the mean relative deviations of ε_b and $\beta_{b,d}$ values for the two packed beds in the longitudinal direction have the same order of magnitude, these values in radial direction for the packed bed of spheres are significantly higher than those for the packed bed of trilobes due to the effect of the radial porosity distribution.

Packing	u_{0L} (mm/s)	$\beta_{b,d}$	ε_b	mean relative deviation (%)	
				radial	vertical
Trilobe			0.41	10.6	3.8
Sphere			0.39	25.2	3.1
Trilobe	0.94	0.37		19.6	8.0
	0.12	0.15		12.9	13.7
Sphere	3.88	0.41		22.2	8.1
	0.29	0.11		54.0	18.2

Table 6.8: Mean values of porosities and dynamic liquid saturations for packed beds of trilobes and spheres. Relative deviation is given by $\sigma = \frac{1}{n} \sum \left(\left| x - \bar{x} \right| / \bar{x} \right) \times 100$ in %.
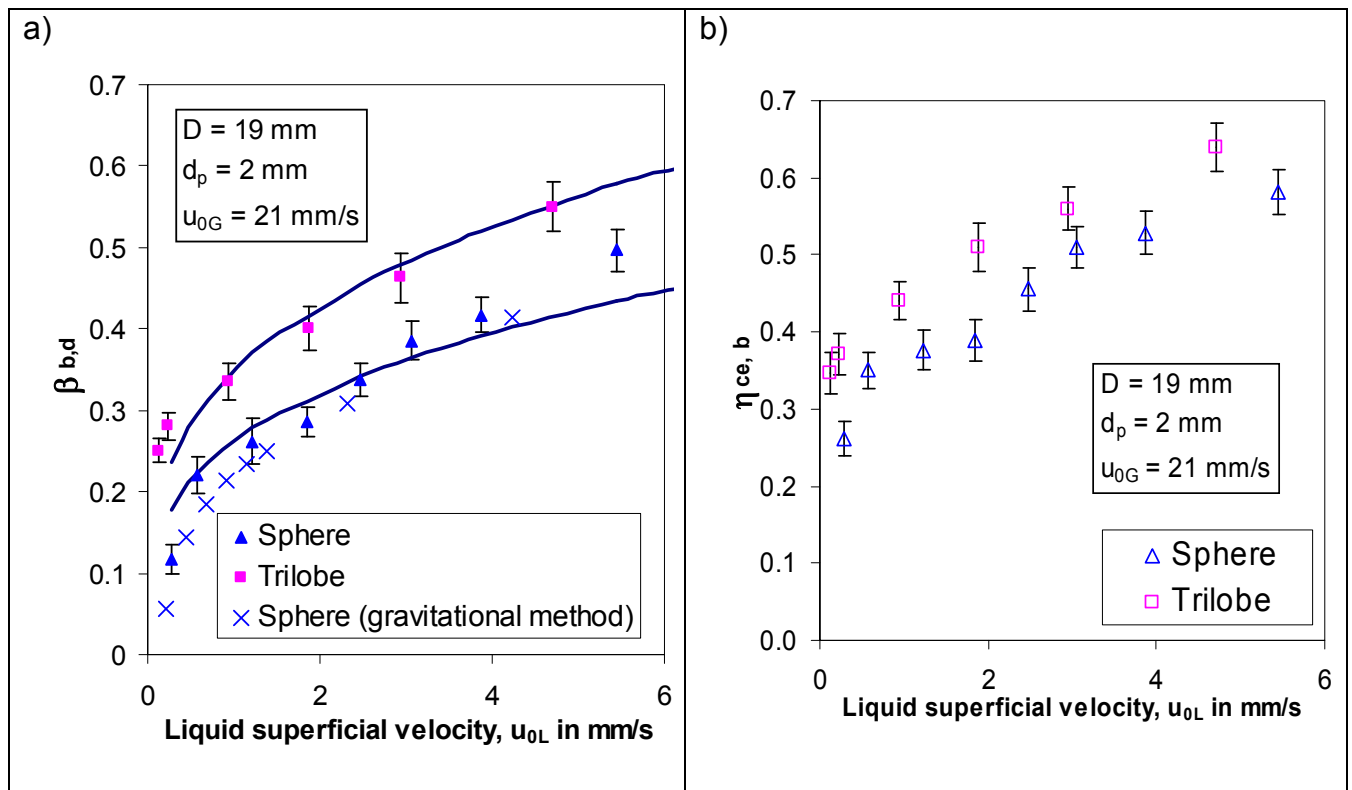
b) Bulk dynamic liquid distribution and wetting efficiency

Figure 6.18: a) Bulk dynamic liquid saturation and b) bulk wetting efficiency as function of liquid superficial velocities measured at atmospheric condition with air/water for packed beds of spheres and trilobes. The bars indicate the mean deviations of the bulk values determined from 3D-images.

The global hydrodynamic quantities (i.e. bulk liquid saturation and wetting efficiency) were obtained by simply averaging their local values over the whole beds (eqs. 5.5 & 5.9). For measurements under atmospheric condition for the two packed beds Fig. 6.18a and Fig. 6.18b show that $\beta_{b,d}$ and $\eta_{ce,b}$ increase with increasing liquid superficial velocity. The $\beta_{b,d}$ values of the packing of spheres obtained by MRI-experiments are in good agreement with those determined by gravitational method, which is considered to be a validation of MRI experimental and image analysis methodologies employed.

d) Measurements under elevated temperature and pressure

Since industrial trickle bed reactors are operated at high pressures and temperatures, knowledge on possible effects of temperature and pressure on the fluid dynamic behaviour of two phase flow is necessary. One of the main objectives of this study, therefore, is to investigate the liquid distribution in the cocurrent gas/liquid trickle bed reactor at elevated temperatures and pressures. However, in order to prevent any damage happening to MRI hardware at high temperature, the in-situ measurements were limited to a maximal temperature of 150°C. The gas-liquid system used in experiments was nitrogen-diesel.
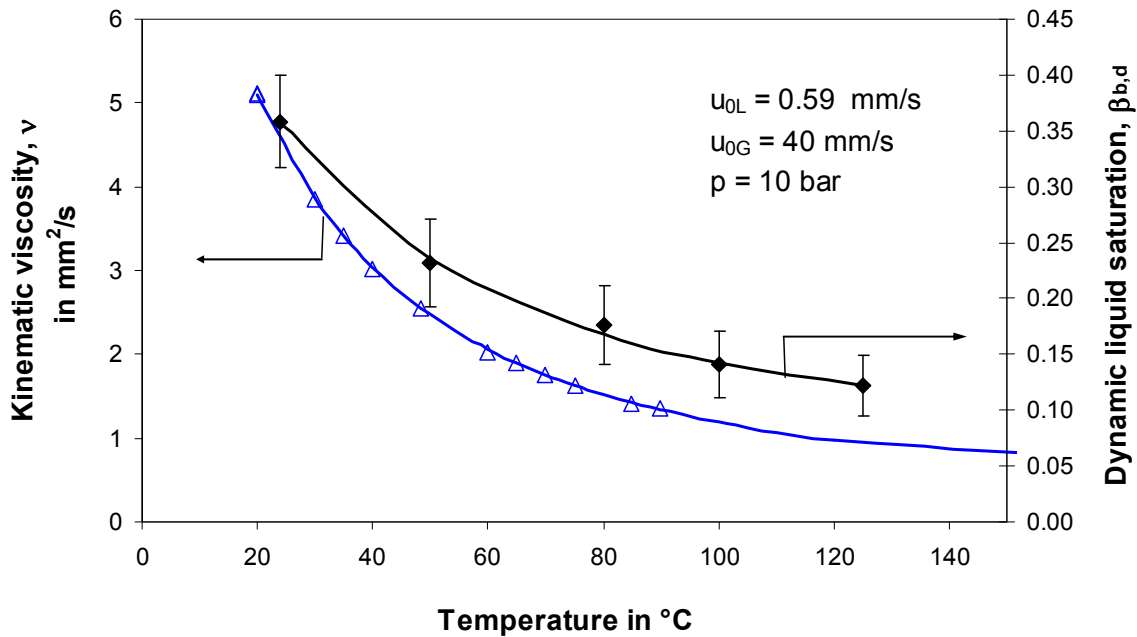
Figure 6.19: Effect of diesel viscosity on the gas-liquid distribution in a packed bed of spheres. MRI-Measurements took place in the range of temperatures from 24°C to 125°C at constant liquid and gas flow rates of 10ml/min and 500 Nml/min, respectively, and at a pressure of 10 bars. Liquid saturation values are obtained by analysing the data of 2D-images (Fig. 6.20) extracted from 3D-images. The bars indicate the standard deviations in the $\beta_{b,d}$-values.
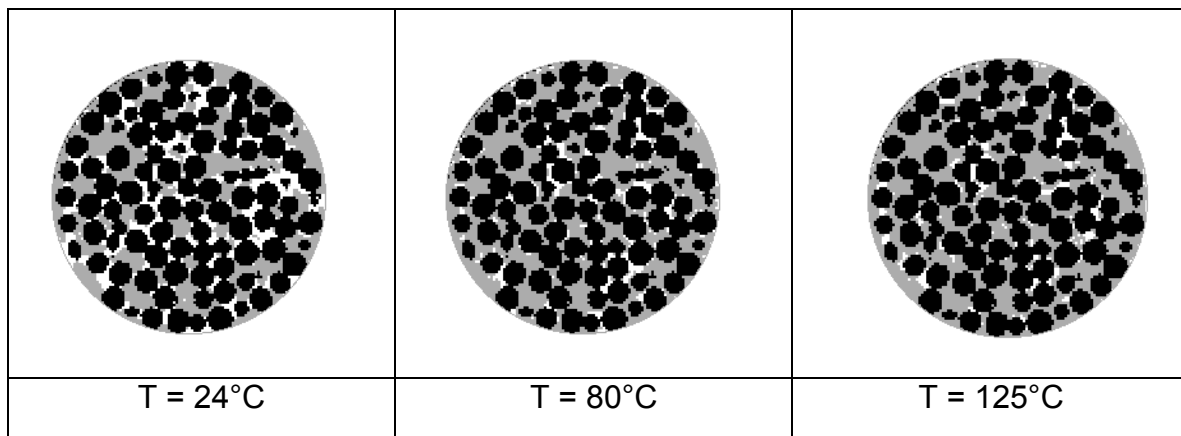

| T = 24°C | T = 80°C | T = 125°C |

Figure 6.20: 2D-slices were obtained from the measurements during two-phase flow at different temperatures in a packed bed of spheres. In-plane spatial resolution is 168 μm x 168 μm x 168 μm. Different phases are distinguished by colors: black (solid phase), white (liquid phase) and grey (gas phase).

It is clearly recognized from the MRI-images in Fig. 6.19 that the liquid saturation reduces gradually as the experimental temperature increases. The influence of the operating temperature on the liquid distribution in the packed bed can be explained by means of the resistance force in relation to the gravitational force. For two-phase flow through packed beds, the resistance force caused by the viscous stress τ_{LS} acting on the solid/liquid interface is proportional to viscosity. From the experimental data, the viscosity of diesel drops significantly when temperature increases according

to the Ubbelohde-Walter equation 6.9 [Man01]. The gravitational force depends on liquid density which is practically not affected by temperature. As a consequence, with increasing temperature, the ratio of gravitational force and viscous force becomes higher which causes a gradual reduction of the liquid saturation in the packed bed as seen in Fig.6.19.

$$\lg\lg(\nu + C) = K - m.\lg T \quad \text{where } C = 0.6 \text{ mm}^2/\text{s}, \tag{6.9}$$
$$K = 11.1 \lg\lg(\text{mm}^2/\text{s}) \text{ and } m = 4.53 \lg\lg(\text{mm}^2/\lg(K))$$
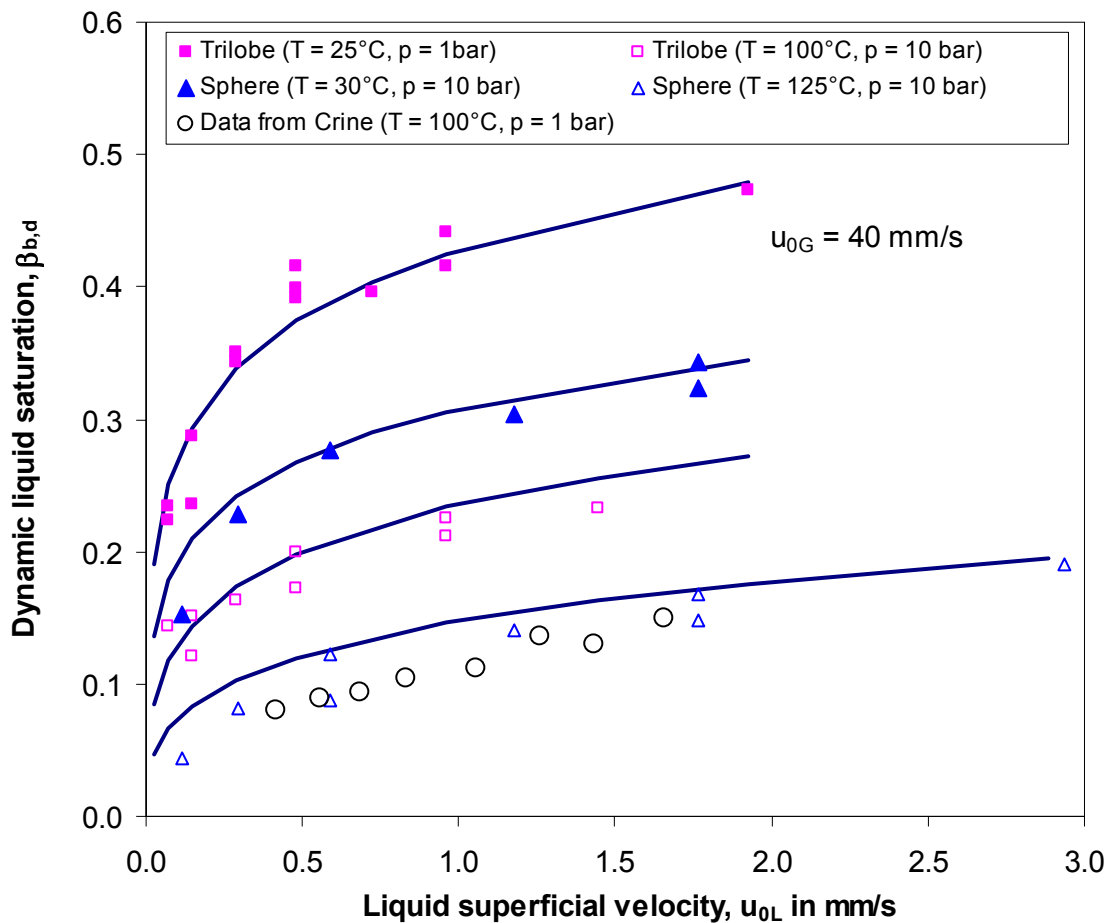
Figure 6.21: Correlation between liquid saturation and liquid superficial velocity in the trickle flow regime operated at atmospheric condition and at elevated temperature and pressure. Lines are calculated with equation 6.10. Experimental results from Crine et al. [Cri81] were measured during the hydrogenation of α-methylstyrene at T =100°C, p = 1 bar in a trickle bed reactor (D = 40 cm) containing Pd/γ-Al$_2$O$_3$ pellets (d_p = 3 mm).

The measurement results for packed beds of glass beads and trilobes performed at ambient condition (T = 25°C and p = 1atm) and at elevated temperature and pressure (T = 125°C, p = 10 bar) are plotted in Fig. 6.21. It can be clearly seen that $\beta_{b,d}$ values measured at elevated temperature and pressure are much lower in

comparison to those measured at atmospheric conditions. The results for the packed bed of spheres are similar to experimental data measured at actual operating conditions by Crine et al. [Cri81].

The measured dynamic liquid saturation for both packings could be correlated with a power law function of dimensionless numbers (eq. 6.10), where Re_L and Ga_L are the Reynolds and Galileo numbers of the liquid, respectively.

$$\beta_{b,d} = 5.5 \, Re_L^{0.35} \left[Ga_L \left(1 + \frac{\Delta p}{L \rho_L g} \right) \right]^{-0.43} \psi^{0.65} \qquad (6.10)$$

The correction term $\psi = a_v d_p / \varepsilon_b$ accounts for the effect of the packing properties and is adopted from the literature [Spe77]. The exponents for Re_L and Ga_L in this correlation agree well with the data of Wammes [Wam91]. However, the pre-factor of 5.5 is greater than that of 3.68 given by Wammes' correlation. Actually the packings used in MRI and Wammes' experiments are different so that no definite conclusion can be inferred from these comparisons. Analysis of the residuals indicates that the standard error of the fitted values is about 10% of the experimental data.

Wetting efficiency can be directly determined from the measured images by using the same method as for determining liquid saturation (eqs. 5.7 – 5.9). However, the quantitative evaluation is highly sensitive to spatial resolution of MRI-data due to much more voxels of partial filling with liquid situated at the interfaces between solid/liquid phases [Bal96]. Therefore, the data sets of this experiment having high spatial resolution of voxels (168 μm) are not suitable for the quantitative determination of wetting efficiency.

6.1.4 Pressure drop measurements

Pressure drop arises over the bed due to friction at interfaces between phases. The relationship between pressure drop and interaction forces is given by the overall force balances in gas and liquid phases given by eqs. 2.2 and 2.3. According to a classical approach based on Ergun equation [Erg52], the energy loss in the packed beds due to the friction forces can be treated as sum of laminar flow and of turbulent flow dominated energy losses which relate to the flow velocity, fluid density and viscosity of each phase. As illustrated in Fig. 6.22 the pressure drop decreases strongly with increasing temperature at a given pressure and fluid flow rates. This effect can be explained by means of the reduction of the liquid saturation and the resisting viscous component of drag forces due to the decrease of liquid viscosity when temperature increases.
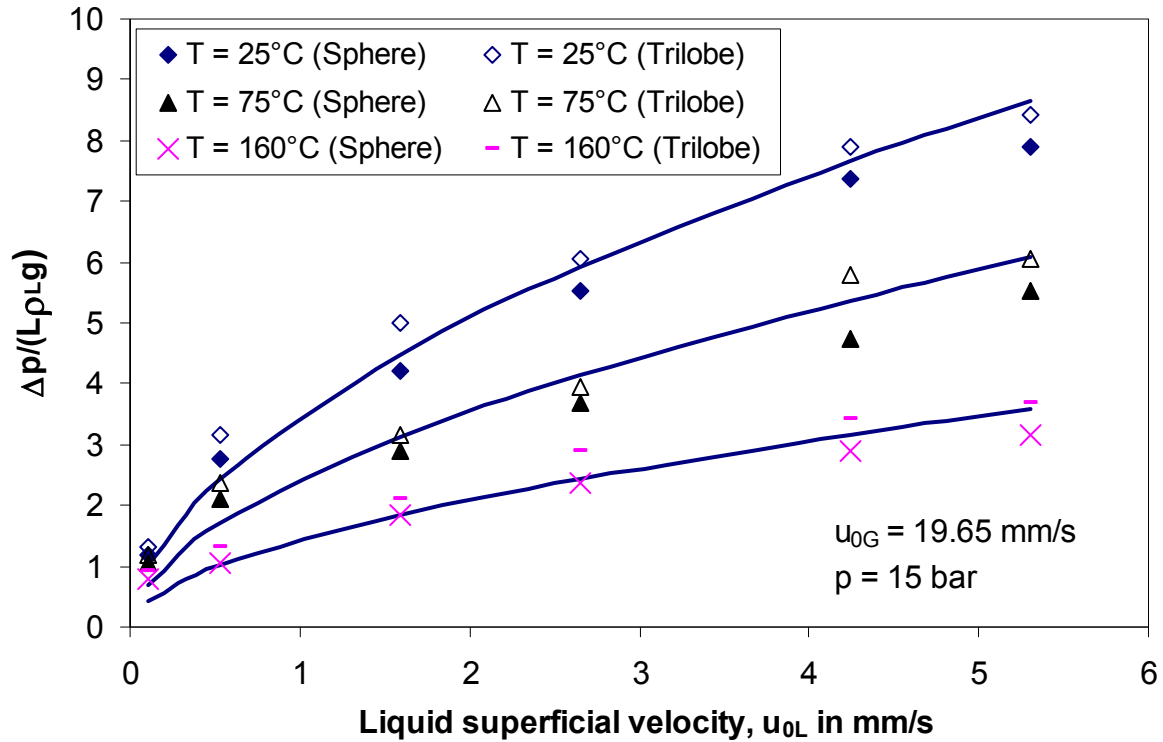
Figure 6.22: Pressure drop as function of liquid velocity with the influences of temperature. Solid lines represent the calculated values from equation 6.11.

$$\frac{\Delta p}{L\rho_L g} = 2.05 \, \mathrm{Re}_L^{0.55} \, \mathrm{Re}_G^{0.11} \qquad\qquad (6.11)$$

It is also observed that the packed bed of trilobe particles exhibits higher pressure drops than the packed bed of spheres for all measurements, although their overall bed porosities are almost the same. The reason for this might be the higher surface/volume ratio of trilobe particles in comparison with spherical particles [Sie98b, Mac04].

6.2   RTD-measurements

Measured data points shown in Fig. 6.23 for space velocities, LHSV from 1h[-1] to 4 h^{-1}, clearly indicate that the lower liquid flow rate gives the broader resident time distribution. This implies that the dispersion and channelling effects due to non-uniformity of liquid velocity profiles in the catalyst bed become more significantly with decreasing liquid flow rate. Therefore, the examination of deviations from plug flow reactors is especially important at low space velocities for deep HDS where extremely high conversion is aimed at. The analytical expression of the $E(\theta)$ response curve (eq. 5.13) in Chapter 5.1 for the so-called 'open-open' boundary condition was used to evaluate the experimental data in order to obtain the best-fit value of Pe number [Lev93]. In Fig. 6.23, the agreement between the measured and

the fitted RTDs for LHSV= 1h^{-1} and LHSV = 4h^{-1} is quite good. Whereas the fitting of measured data for the cases of LHSV = 2h^{-1} and LHSV = 3h^{-1} resulted in optimal Pe numbers with a correlation coefficient R^2 = 0.97.
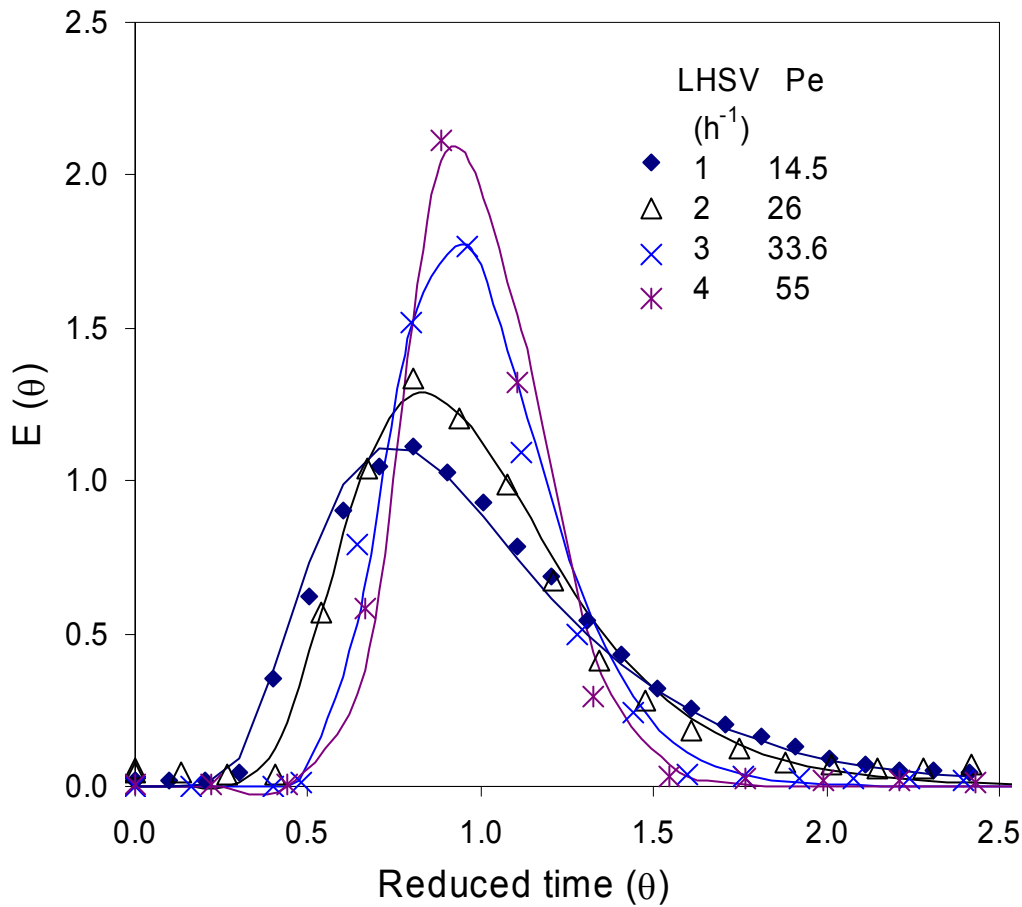
Figure 6.23: RTD experiments with squalane tracer at reactor temperature T = 150°C and pressure p = 40 bar. Solid lines represent fitted data.

In Tab. 6.9 the results of liquid saturation and axial dispersion obtained from MRI- and RTD-experiments are summarized. The dynamic liquid saturation data were obtained from the MRI experimental results shown in Fig. 6.21.

LHSV (h^{-1})	$^V\Phi_L$ (ml/min)	$\beta_{b,d}$ from MRI-measurements	Pe	D_{ax} (m^2/s)	R^2
1	1.7	0.17	14.5	8.5x10^{-5}	0.99
2	3.5	0.19	26	5.57x10^{-5}	0.97
3	5.2	0.21	33	5.37x10^{-5}	0.97
4	6.9	0.23	55	3.8x10^{-5}	0.99

Table 6.9: Results of MRI- and RTD-experiments

6.3 HDS-experiments

The properties of the gas oil used in this study as shown in Tab. 6.10 were analyzed using the standards ASTM D2887 and IP391, respectively.

	Syrian Oural gas oil
S (ppmw)	4612
N (ppmw)	112
Total aromatics (wt %)	28
Naphthenes (wt %)	19
IBP (0.5 vol. %) (°C)	204
50 vol. % (°C)	312
FBP (99:5 vol. %) (°C)	367
Density (kg/m^3)	851

Table 6.10: Properties of feedstock

As described in the experimental section (chapter 5.2), the HDS measurements were carried out in a bench scale reactor in a wide range of temperatures and space velocities (LHSV). The following figures (Fig. 6.24a and b) show the conversions of sulfur in diesel oil with their experimental uncertainties. It can be seen in these figures that increase of temperature as well as decrease of space velocity have a strong effect on the conversion of sulfur compounds, while other process parameter are kept constant. These results indicate that in order to meet the sulfur specification of 10 ppmw for deep hydrodesulfurization the reaction temperature should be increased to more than 360°C and simultaneously the space velocity is decreased to below 1h^{-1}.

For deep hydrodesulfurization, the removal of very difficult sulfur compounds, which exist dominantly in lowered sulfur level diesel, follows the hydrogenation route and is affected by thermodynamic equilibrium. The limit temperature at about 380°C is generally reported by many researchers [Ped03, Cho02, Che04]. Because this study aims at investigating the influence of fluid dynamic non-idealities on the hydrodesulfurization, the equilibrium effect of temperature on hydrogenation reaction is not taken into account. For this reason, the experimental temperature was limited to 380°C, at which the level of HDS conversion reached 94% at LHSV = 2 h^{-1} (Fig. 6.24 a). Moreover, in industrial application, increasing reaction temperature reduces the life cycle of catalyst and hence new investment is required for catalyst change. Since the increase in temperature is limited, an effective solution certainly needs additional catalyst's volume or reduced LHSV's values in order to achieve higher conversion.
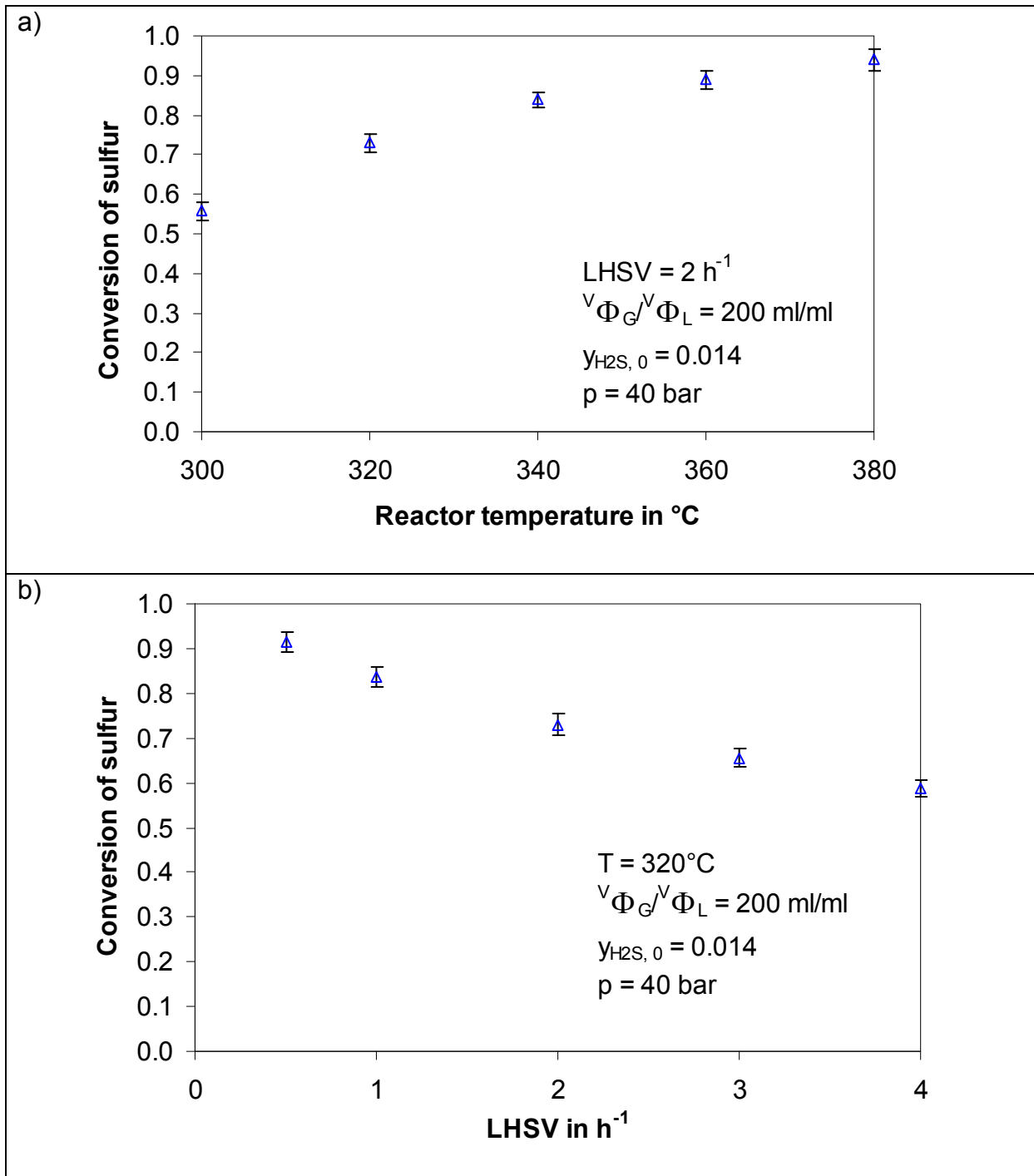
Figure **6.24**: HDS results influenced by a) temperature and b) LHSV

7 Mathematical modelling

In chapter 2, several aspects of fluid dynamic and mass transfer phenomena were presented that may deteriorate the performances in hydroprocessing laboratory reactors. In this context, a number of experiments were realized in present work first to quantify the fluid dynamics and second to evaluate the interaction with the HDS reaction. The experimental HDS results were presented in chapter 6.

The aim of this chapter is to develop a numerical model that integrates the fluid dynamic parameters and the gas-liquid mass transfer in order to give indications how far these parameters may influence the global reaction rate. Because a pseudohomogenous model cannot account for the gas-liquid mass transfer and the axial dispersion in the liquid phase, a multiphase model was developed. In this model the following characteristics are accounted for:

- the HDS reaction kinetics

- the gas-liquid mass transfer

- the liquid saturation

- the axial dispersion in the liquid phase

It should be remarked that it was not the scope of this work to develop a detailed kinetic model for the HDS operation. In previous work, Pedernera [Ped03] investigated the desulfurization of diesel oil in an isothermal trickle bed reactor and developed a two phase reactor model considering both mass transfer and chemical reaction. This study extends the model used by Pedernera, which includes the effect of hydrodynamics on HDS reaction.

7.1 Reaction term

The components that are accounted for in the model are the gas oil, the sulfur compounds, hydrogen and hydrogen sulfide. Because of different sulfur compounds present in the gas oil feedstock, it is necessary to define a generalized expression for the HDS reaction:

$$2H_2 + XS \rightarrow YH_2 + H_2S \tag{7.1}$$

XS: pseudocomponent with sulfur; YH_2: sulfur-free pseudocomponent.

A sulfur compound reacts with two hydrogen molecules to yield one molecule of hydrogen sulfide. It is assumed that the hydrodesulfurization is an irreversible reaction. In addition, many studies have shown that HDS-reaction is inhibited by the presence of H_2S. Thus, taking into account all this information, the Langmuir-Hinshelwood type expression is applied in the model for the HDS rate of reaction. In this case, the kinetic rate depends on the concentration of reactants in the liquid phase.

$$r_{XS} = -k_0 \exp\left(-\frac{E}{RT}\right)\frac{C_{XS,L}^{n_1} C_{H_2,L}^{n_2}}{(1+K_{ad}C_{H_2S,L})^2} = k\frac{C_{XS,L}^{n_1} C_{H_2,L}^{n_2}}{(1+K_{ad}C_{H_2S,L})^2} \tag{7.2}$$

where r_{XS} is the rate of reaction per unit of catalyst mass.

7.2   Model hypothesis

A mathematical model has been developed to describe the HDS-process in an isothermal bench scale reactor that operates at steady state. In order to simplify the model, the following assumptions are made:

1. Gas and liquid superficial velocities are constant throughout the reactor length.

2. Radial gradients of concentration across the reactor cross section are not considered.

3. Evaporation of gas oil occurs instantaneously only at the entrance of the reactor. Fig. 7.1 shows the vapor-liquid equilibrium obtained with the commercial process simulator Aspen Plus. Percentage of diesel oil in vapour phase was calculated as the amount of diesel vaporized divided by the amount of liquid diesel oil before mixing with hydrogen. It can be clearly seen that the vaporized fraction of liquid feed was quite small (< 2 %) at a temperature of 300 °C and reached nearly 20 % at a temperature of 380 °C.
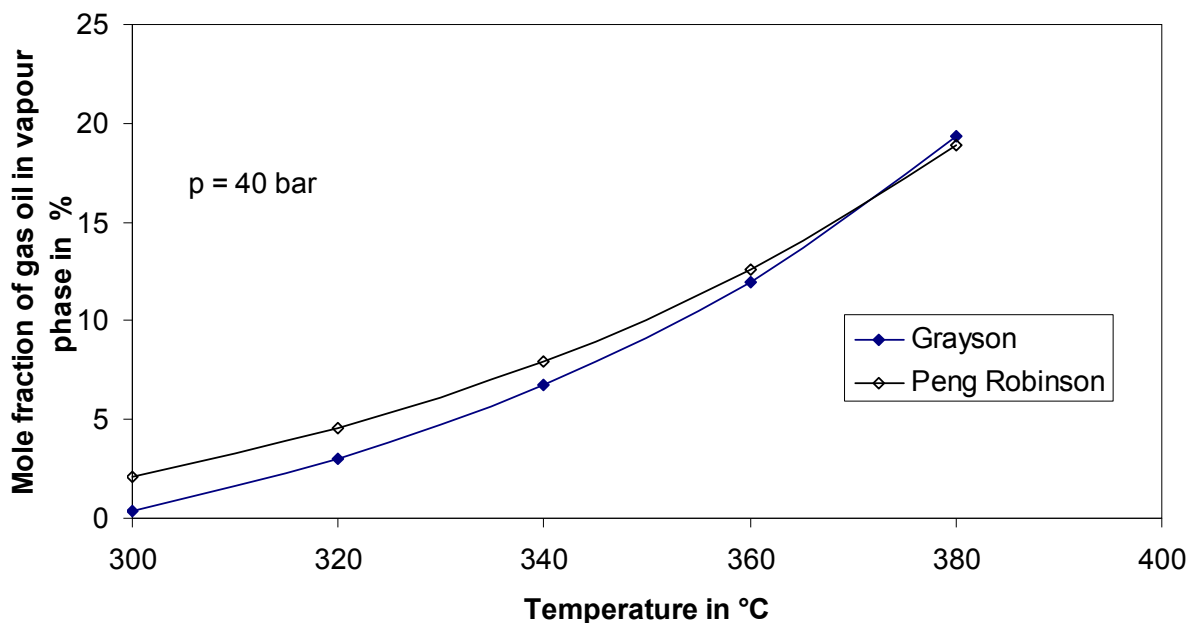
Figure 7.1: Results of flash calculation for the vapour-liquid thermodynamic equilibrium of diesel oil using Peng-Robinson and Grayson equations of state, respectively.

4. Hydrogen and gas oil are supposed to be in equilibrium before entering the catalytic bed. This assumption seems to be justified since the hydrogen and the feed are in contact in the lines and in the preheating zone before entering the reactor. The length of the line is about 0.5 m. Moreover, the fluids have to flow through the zone of inert SiC-particles before entering the catalytic zone, where intensive mixing should take place.

85

5. The gas side of gas-liquid mass transfer resistance is supposed to be negligible [Kor96]. The gas-liquid mass transfer coefficient values are chosen according to the correlation of Larachi [Lar03].

6. Since the liquid distribution in the near wall region of packings of trilobe particles is not significantly different from that in the central region (Fig. 6.16b), the impacts of wall effect and the back mixing phenomena are lumped in an axial dispersion coefficient for the liquid phase.

7. The pressure drop in the reactor is neglected. During the experiments only a slight pressure drop of 200 mbar to 350 mbar at a pressure of 40 bar was observed in the range of LHSV from 1 h^{-1} to 4 h^{-1} at the operating temperature and pressure (see Fig. 6.22).

7.3   Model equations

According to the above assumptions, the kinetic modelling is based on the two-film theory as shown in Fig. 7.2b. The reactants must first be transferred from the gas phase to liquid phase and then to the solid catalyst surface. The internal pores of the catalyst are supposed to be entirely filled with liquid [Kor96].
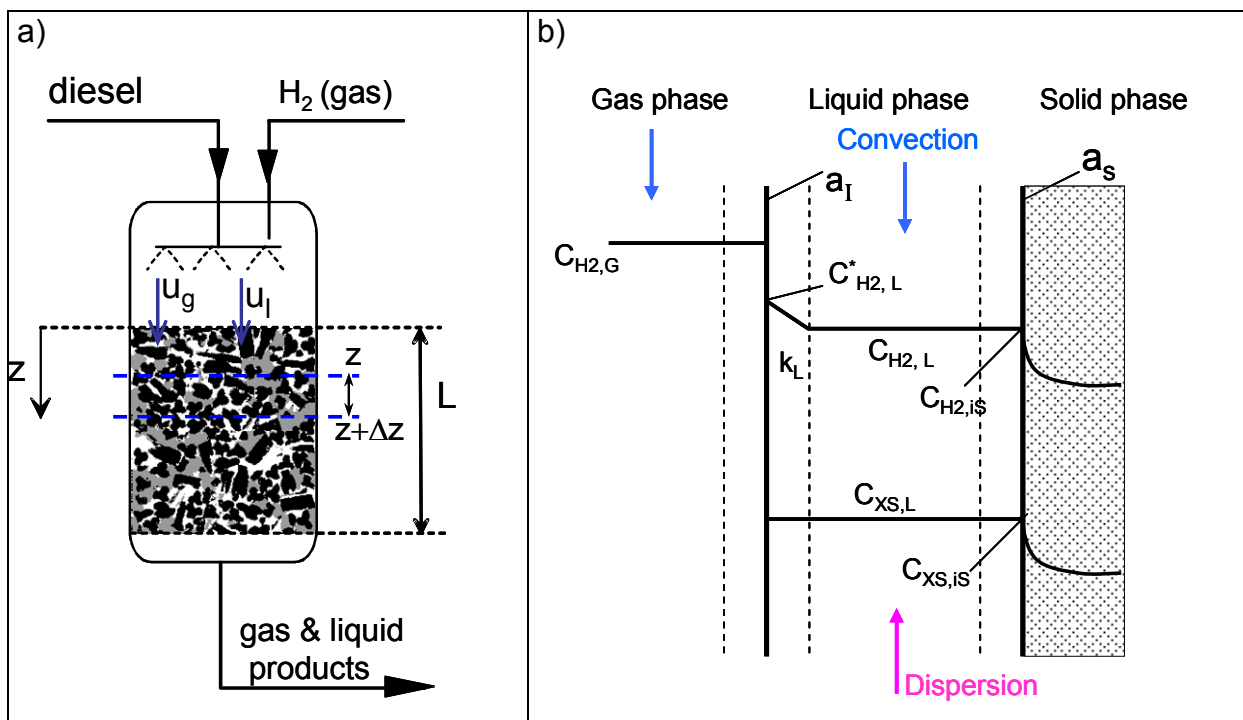

Figure 7.2: a) Schematic of the trickle bed reactor for the modelling b) Reactant concentration profiles in three phases

At the steady state condition, it is assumed that the mass transfer rate between the liquid phase and the surface of catalyst is identical with the reaction rate. Since the HDS reaction rate is slow, the concentrations of the reactants at the catalyst surfaces

are considered the same as in the bulk liquid [Ped03]. Therefore, in the simulation program the solid phase is not accounted for a separate phase.

The model is based on steady state mass balances of hydrogen, hydrogen sulfide and sulfur compound in the gas and liquid phases. For the gas phase, previous investigations indicated marginal importance of axial mixing. Referring to the differential volume of thickness Δz at any position z in the reactor (Fig. 7.2a), the species balance equations for gas phase are the following:

Hydrogen:

$$C_{H_2,G}\big|_z u_G \varepsilon_b (1-\beta_b)A - C_{H_2,G}\big|_{z+\Delta z} u_G \varepsilon_b (1-\beta_b)A - k_L a_1 \left(\frac{C_{H_2,G}}{H_{H_2}} - C_{H_2,L} \right) A\Delta z = 0 \tag{7.3}$$

Hydrogen sulfide:

$$C_{H_2S,G}\big|_z u_G \varepsilon_b (1-\beta_b)A - C_{H_2S,G}\big|_{z+\Delta z} u_G \varepsilon_b (1-\beta_b)A - k_L a_1 \left(\frac{C_{H_2S,G}}{H_{H_2S}} - C_{H_2S,L} \right) A\Delta z = 0 \tag{7.4}$$

Dividing both sides of the above equations by $A\Delta z$ and limiting $\Delta z \to 0$ results in:

$$u_G \varepsilon_b (1-\beta_b)dC_{H_2,G} + k_L a_1 \left(\frac{C_{H_2,G}}{H_{H_2}} - C_{H_2,L} \right) dz = 0 \tag{7.5}$$

$$u_G \varepsilon_b (1-\beta_b)dC_{H_2S,G} + k_L a_1 \left(\frac{C_{H_2S,G}}{H_{H_2S}} - C_{H_2S,L} \right) dz = 0 \tag{7.6}$$

The mass balances in the liquid phase in the inner of the reactor are more complex due to the chemical reaction and due to axial dispersion. The mass balance equation for sulfur compounds can be written as follows:

$$C_{XS,L}\big|_z u_L \varepsilon_b \beta_{b,d} A - D_{ax} A \varepsilon_b \beta_{b,d} \frac{dC_{XS,L}}{dz}\bigg|_z - C_{XS,L}\big|_{z+\Delta z} u_L \varepsilon_b \beta_{b,d} A + D_{ax} A \varepsilon_b \beta_{b,d} \frac{dC_{XS,L}}{dz}\bigg|_{z+\Delta z} + r_{XS}\rho_b A\Delta z = 0 \tag{7.7}$$

Dividing the both sides by $A\Delta z$ and limiting $\Delta z \to 0$ results in:

$$D_{ax}\varepsilon\beta_{b,d} \frac{d^2 C_{XS,L}}{dz^2} - u_L \varepsilon_b \beta_{b,d} \frac{dC_{XS,L}}{dz} + r_{XS}\rho_b = 0 \tag{7.8}$$

For the gaseous compounds in the liquid phase, the gas-liquid mass transfer must be taken into consideration. Similarly to sulfur compounds, the differential mass balance equations for hydrogen and hydrogensulfide are as follows:

87

Hydrogen:

$$D_{ax}\varepsilon_b\beta_{b,d}\frac{d^2C_{H_2,L}}{dz^2} - u_L\varepsilon_b\beta_{b,d}\frac{dC_{H_2,L}}{dz} + k_La_1\left(C^*_{H_2,L} - C_{H_2,L}\right) + 2\cdot r_{XS}\rho_b = 0 \qquad (7.9)$$

Hydrogen sulfide:

$$D_{ax}\varepsilon_b\beta_{b,d}\frac{d^2C_{H_2S,L}}{dz^2} - u_L\varepsilon_b\beta_{b,d}\frac{dC_{H_2S,L}}{dz} + k_La_1\left(C^*_{H_2S,L} - C_{H_2S,L}\right) - r_{XS}\rho_b = 0 \qquad (7.10)$$

The boundary conditions for the two first order differential equations (7.5) and (7.6), at z = 0 are given as:

$$\begin{aligned} u_G(z) &= u_{G0} \\ C_{H_2,G}(z=0) &= C_{H_2,G0} \\ C_{H_2S,G}(z=0) &= C_{H_2S,G0} \end{aligned} \qquad (7.11)$$

The axial dispersion terms result in second order differential equations (7.8) – (7.10) for the liquid phase and consequently two boundary conditions are necessary. In the case of a piston-dispersion model as used here the boundary conditions of Danckwerts [Dan53] are generally applied. Their physical meaning is that axial dispersion neither occurs in the inlet section nor in the outlet section. These boundary conditions can be expressed as:

$$z = 0: \qquad u_LC_{i,L} = u_LC_{i,L}\big|_{z=0^+} - D_{ax}\varepsilon_b\beta_{b,d}\frac{dC_{i,L}}{dz} \qquad (7.12)$$

$$z = L: \qquad \frac{dC_{i,L}}{dz} = 0$$

where $C_{i,L}$ is the liquid phase concentrations of H_2, H_2S and sulfur compounds.

7.4   Numerical method

The set of the above differential equations (7.3 to 7.8) is transformed into dimensionless forms that will facilitate the computer programming and also the results' interpretation. This task will be done by introducing following dimensionless parameters:

$$P_1 = \frac{C_{H_2,G}}{C_{H_2,G0}}; \quad P_2 = \frac{C_{H_2S,G}}{C_{H_2S,G0}}; \quad \varphi_1 = \frac{C_{XS,L}}{C_{XS,L0}}; \quad \varphi_2 = \frac{C_{H_2,L}}{C_{H_2,L0}}; \qquad (7.13)$$

$$\varphi_3 = \frac{C_{H_2S,L}}{C_{H_2S,L0}}; \quad Z = \frac{z}{L}; \quad Pe = \frac{u_LL}{D_{ax}}$$

Gas phase mass balance:

Hydrogen:

$$\frac{dP_1}{dZ} + \alpha_1\left(P_1 - \varphi_2\right) = 0 \tag{7.14}$$

Hydrogen sulfide:

$$\frac{dP_2}{dZ} + \alpha_2\left(P_2 - \varphi_3\right) = 0 \tag{7.15}$$

Liquid phase:

Sulfur compounds:

$$\frac{d^2\varphi_1}{dZ^2} - Pe\frac{d\varphi_1}{dZ} - R_1\frac{\varphi_1^{n1}\varphi_2^{n2}}{\left(1 + k_{ad}C_{H_2S,L0}\varphi_3\right)^2} = 0 \tag{7.16}$$

Hydrogen

$$\frac{d^2\varphi_2}{dZ^2} - Pe\frac{d\varphi_2}{dZ} + R_2\left(1 - \varphi_2\right) - R_3\frac{\varphi_1^{n1}\varphi_2^{n2}}{\left(1 + k_{ad}C_{H_2S,L0}\varphi_3\right)^2} = 0 \tag{7.17}$$

Hydrogen sulfide

$$\frac{d^2\varphi_3}{dZ^2} - Pe\frac{d\varphi_3}{dZ} + R_2\left(1 - \varphi_3\right) - R_4\frac{\varphi_1^{n1}\varphi_2^{n2}}{\left(1 + k_{ad}C_{H_2S,L0}\varphi_3\right)^2} = 0 \tag{7.18}$$

Where α_1, α_2, R_1, R_2, R_3 and R_4 are constants:

$$\alpha_1 = \frac{k_L a_1 L}{u_G \varepsilon_b (1 - \beta_b) H_{H2}} ; \quad \alpha_2 = \frac{k_L a_1 L}{u_G \varepsilon_b (1 - \beta_b) H_{H2S}} ; \tag{7.19}$$

$$R_1 = \frac{kL^2 C_{XS,L0}^{n1-1} C_{H2,L0}^{n2} \rho_b}{D_{ax}\varepsilon_b\beta_{b,d}} ; \quad R_2 = \frac{k_L a_1 L^2}{D_{ax}\varepsilon_b\beta_{b,d}} ;$$

$$R_3 = \frac{2kL^2 C_{XS,L0}^{n1} C_{H2,L0}^{n2-1}\rho_b}{D_{ax}\varepsilon_b\beta_{b,d}} ; \quad R_4 = \frac{kL^2 C_{XS,L0}^{n1} C_{H2,L0}^{n2}\rho_b}{D_{ax}\varepsilon_b\beta_{b,d} C_{H2S,L0}}$$

7.5   Simulation program

To obtain an approximate numerical solution to this one-dimensional boundary value problem, the method of the central finite difference scheme was used for discretization the differential equations (7.14) to (7.18) into a set of algebraic equations. The well-known Newton method was applied to solve the nonlinear algebraic equations. A detailed description of the discretization scheme is found in appendix B. These matrix equations were then implemented in the computing software Matlab 6.5 (MATLAB$^{®}$ of The MathWorks, Inc.).

7.6   Simulation results

Kinetic parameters were determined from the experimental data by using an optimization program, which is integrated in the HDS-model. The none-regression procedure based on Marquardt's algorithm [Mar63] is used to minimize the sum of square errors (SSE) between experimental concentration of sulfur in product ($C_{experiment, i}$) and those calculated by the model ($C_{simulation, i}$).

$$SSE = \sum_{i=1}^{no\ experiments}(C_{simulation,i} - C_{experiment,i})^2 \qquad (7.20)$$

The reaction rate parameters such as constant k_0, activation energy E, order of reaction regarding sulfur compound n_1 and hydrogen n_2 had to be determined for the kinetic expression (eq. 7.2). The value of the adsorption coefficient K_{ad} is assumed constant in the range of reaction temperatures [Kor96, Ped03]. The determined parameters with their confidence intervals are tabulated in Tab. 7.2.

Reaction rate constants	Value	Lower limit	Upper limit
k_0 $((m^3)^{n1+n2}(kmol)^{1-n1-n2}kg^{-1}s^{-1})$	2114	2020	2208
E (J/mol)	82682	82224	83140
n_1	1.8	1.67	1.93
n_2	0.45	0.41	0.49
K_{ad} (m^3/mol)	1.3×10^{-3}		

Table 7.2: Reaction rate and adsorption constants
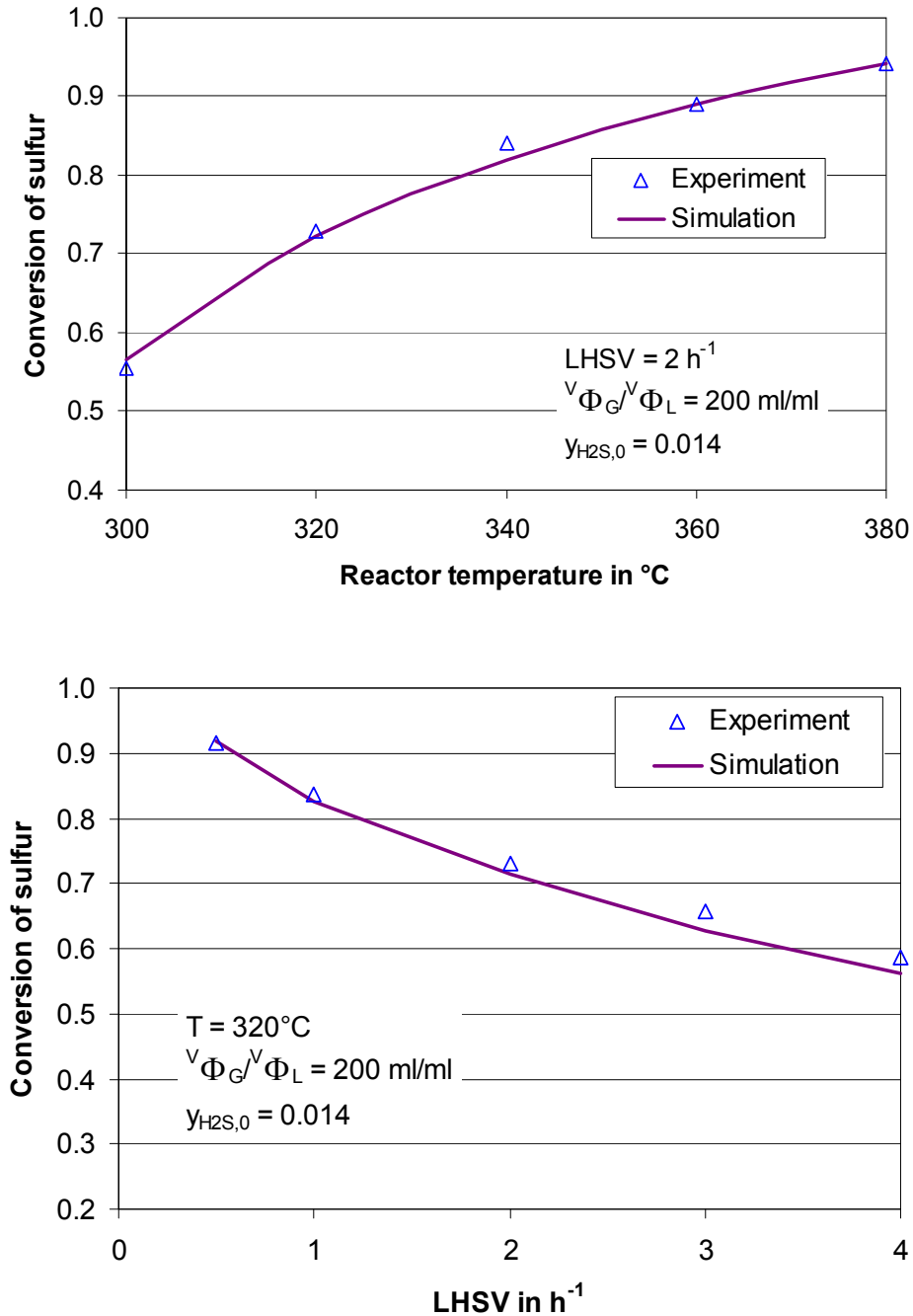
Figure 7.3: Comparison between experimental and simulated overall conversion of sulfur in the product

Fig 7.3 shows a comparison between experimental and calculated overall conversion of sulfur as functions of reaction temperature and LHSV. The model calculates accurately experimental data obtained at different reaction temperatures. However, in the case of high space velocities (LHSV = 3 h^{-1} to 4h^{-1}) the model underestimates the conversions compared with experimental results. But these values still fall within the range of measurement accuracy (5% deviation from experimental data).

Having rather good agreement between simulation and experimental results for the overall conversion, an attempt was made to illustrate the profiles of sulfur and

hydrogen in the oil along the reactor length (Fig. 7.4). Obviously, the concentration of sulfur decreases continuously with the advance of HDS reaction through the reactor. The curve of dissolved hydrogen might be explained as follows: In the first section of the reactor the concentrations of both organic sulfur and dissolved hydrogen are high. Consequently the reaction rates are high, too. The hydrogen dissolved in the liquid phase is consumed by the reaction faster than that being replaced from the gaseous phase. In the later section of the catalytic bed the sulfur content is lower resulting in a lower reaction rate. In this case the gas-liquid transfer is sufficiently high to deliver enough hydrogen from the gas into the liquid phase for the reaction. The influence of the gas-liquid mass transfer on the conversions of sulfur and hydrogen at the first stage of reactor was also reported in the work of Pedernera [Ped03].
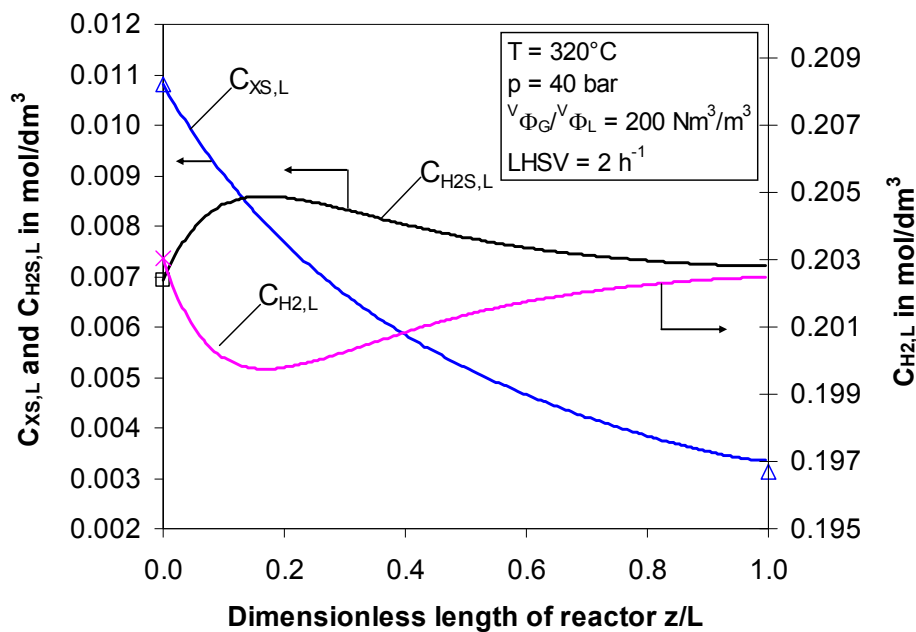
Figure 7.4: Profiles of sulphur and hydrogen concentrations in liquid phase along the reactor axis. Measured data at z/L = 0 and z/L = 1 are represented as symbols.

In a sensitivity analysis the influence of axial dispersion and gas-liquid mass transfer on the conversion of sulfur was studied. First, the term "ideal PFR" means here that neither axial dispersion nor gas-liquid mass transfer limitations were considered, i. e. D_{ax} was set to zero and $k_L a_I$ was assumed infinite ("ideal PFR" in Fig. 7.5). Then, the values for axial dispersion in Tab. 6.9 were reintroduced, while $k_L a_I$ was kept infinite.

The simulation results in Fig. 7.5 show that the influence of both phenomena for axial dispersion and mass transfer increases with the increasing conversion. For lower conversion degrees axial dispersion is likely to cause a smaller deviation from plug flow than mass transfer resistance. But with increasing conversion degrees the axial dispersion effect increases faster and attains the deviation caused by mass transfer resistance at conversion degree of 74%. For higher conversions, especially at deep desulfurization level (>95%), the dispersion effect is dominant over the mass transfer

resistance. It is estimated that a deviation from plug flow of up to 70% for 99% sulfur conversion. Therefore, the influence of axial dispersion on reaction kinetics must be taken into account when data a high conversion levels are used.
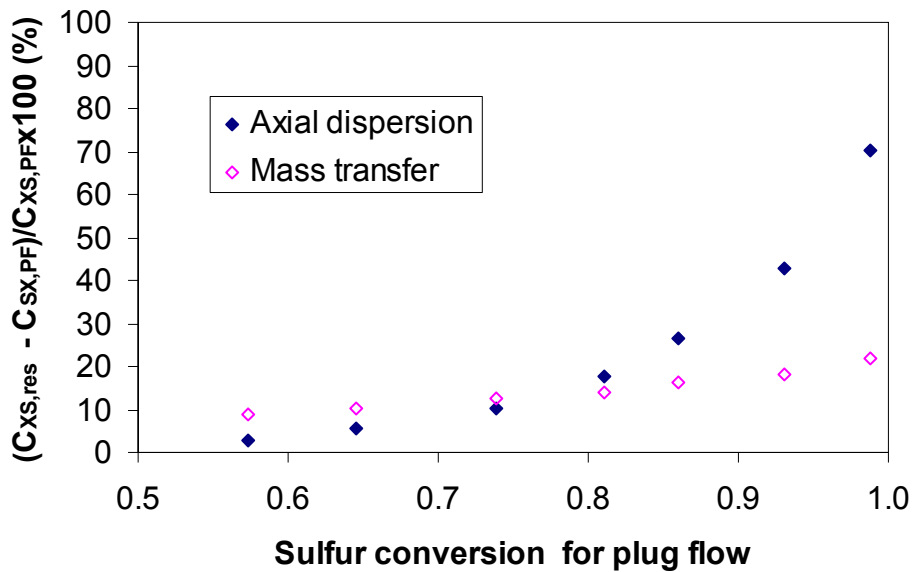
Figure 7.5: Relative difference concerning the residual sulfur concentration at the reactor outlet (1) between the ideal reactor and the reactor with axial dispersion and (2) between the ideal reactor and the reactor with gas-liquid mass transfer resistance. Ideal reactor means plug flow reactor without the influence of axial dispersion and gas-liquid mass transfer.
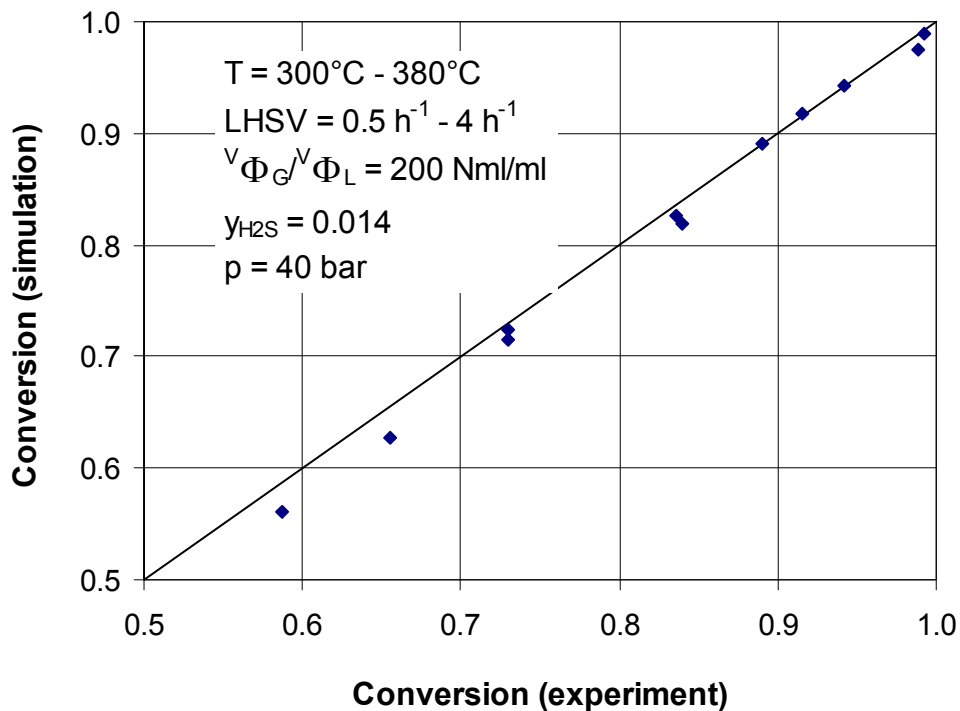

Figure 7.6: Parity plot of sulfur conversion between experiments and simulations

93

A comparison between the experimental and the simulation values over the whole range of operating parameters is given in Fig. 7.6. The difference between experiment and simulation is high at low conversion degrees which relates to the operating conditions at high space velocities (LHSV > 2 h^{-1}) and low temperatures (T < 320 °C). However, a good agreement between simulated values and experimental data is obtained for high conversion degrees, where the influence of fluid dynamics on the reactor performance is much significant than that for low conversion degrees. The model is therefore capable to apply for deep hydrodesulfurization mode of operation in bench scale reactors and is consequently helpful for scale up/scale down purposes.

8 Conclusions and perspectives

This work demonstrates the ability of MRI-technique to visualize structure, liquid distribution and flow texture in packed beds of different forms of particles. The following conclusions regarding fluid dynamic aspects of multiphase system can be drawn:

- Based on a broad range of 3D-images of different packings, the influence of the D/d_p-ratio and the geometry of particles on the non-uniformities of both radial and global porosity distributions are quantitatively evaluated. The results show that the oscillatory behaviour of radial porosity profiles smooths gradually from packings of spheres, cylindrical particles to raschig-rings and trilobes corresponding to the increasing asymmetry of the particles. Similarly, for the same D/d_p-ratio, packings containing particles of more complex geometry have a more uniformly spatial porosity distribution proved by its smaller statistical standard deviation. In general, the spatial porosity distribution for packings of spheres is Gaussian for D/d_p-ratio > 14, while other packings show already a Gaussian distribution for D/d_p-ratio > 10. Due to the "wall effect", global porosity distribution for packings having small D/d_p-ratios follows a lognormal distribution pattern.

- Examination of various literature correlations for estimating radial porosity profiles in packed beds leads to the conclusion that none can represent satisfactorily the whole set of data measured by MRI for different D/d_p-ratioes. Thus, a modified equation was developed by combining Martin's and Giese's equations. As a result, the prediction of radial porosity profiles in packings of spheres and cylindrical particles was significantly improved. In the case of raschig rings, the model of Rottschäfer was successfully applied to calculate radial porosities.

- Velocity distributions of single phase flow through a packed bed of glass beads were investigated in detail. The radial velocity profiles follow an

oscillatory pattern which is similar to the porosity profiles. A 3D CFD-simulation which was performed by generating a geometrical matrix based on the MRI data of a packed bed of glass beads also shows a strong influence of the bed structure on the velocity distribution. However, the flow pattern was not significantly changed in the range of flow rates applied in both experiments and simulations.

- 3D image visualisation of gas-liquid distribution during the trickle flow provides the complete description of fluid dynamic behaviour in terms of local packing properties and relation between local and bed level phenomena. Local liquid distribution and wetting efficiency is strongly affected by bed structure and liquid velocity. At low liquid flow rates, the radial liquid distribution and wall flow are closely related to the local packing structure (e. g. porosity profile). However, the liquid saturation tends to increase in the packing's central region with increasing liquid flow rates due to the channeling flow occuring within the packed beds. The experimental results at both atmospheric condition and at elevated temperature and pressure confirmed that liquid saturation and wetting efficiency are strongly affected by temperature due to the reduction of liquid viscosity. The estimated global liquid saturation is comparable with observations of Crine [Cri81].

The combination of MRI-experiments and catalytic experiments in a bench scale reactor were used to study the influence of fluid dynamics of flowing liquid on the hydrotreating reaction in laboratory reactors. A two-phase reactor model for a bench scale reactor was developed which accounts for the HDS reaction, the axial dispersion in the liquid phase and the gas/liquid mass transfer resistance. The residence time distribution (RTD) measurements were employed to determine the axial dispersion coefficient of a two phase flow in trickle bed reactors at elevated temperatures and pressures. The results confirmed that there exists significant axial dispersion and low liquid saturation at typical hydrotreating conditions in bench scale reactors. Therefore, a scale-up of laboratory plant data to an industrial trickle bed reactor must consider the effects of fluid dynamics on the hydrotreating performance, especially for the case of high conversion degrees (e.g. deep HDS). In the range of normal conversion degrees and due to the fact that the superficial liquid velocity in a large scale reactor is much higher than in laboratory plants, complete catalyst wetting can be expected and deviation from ideal plug flow might be negligible.

MRI has proved to be a reliable method to investigate the distributions of gas/liquid in packed beds for the trickle flow regime. Future work will focus on investigations of dispersion and liquid velocity distribution during two phase flow in order to understand the mixing processes in packed beds. Furthermore, the experiments at elevated temperature and pressure could be improved by choosing appropriate materials and by optimizing the construction of the apparatus.

References

[Arr03]   A. O. Arroyo, F. Larachi, I. Iliuta, Method for inferring contact angle and for correlating static liquid hold-up in packed beds. Chemical Engineering Science, 58 (2003), 2385-2855

[Arr04]   A. O. Arroyo, Contribution to the modelling of packed bed reactors under plugging conditions in single and two phase trickle flow. Ph. D. thesis, Université Laval Québec (2004).

[Bab03]   I. V. Babich, J. A. Moulijn, Science and technology of novel processes for deep desulfurization of oil refinery streams: a review. Fuel 82 (2003), Nr. 6, 607-631

[Bal96]   C. A. Baldwin, A. J. Sederman, M. D. Mantle, P. Alexander, L. F. Gladden, Determination and Characterization of the Structure of a Pore Space from 3D Volume Images. Journal of colloid and interface science, 181 (1996), Nr. 1, 79-92

[Ben62]   R. F. Benenati, C. B. Brosilow, Void fraction distribution in beds of spheres. AIChE Journal 8 (1962), 359-361

[Bey97]   O. Bey, G. Eigenberger, Fluid flow through catalyst filled tubes. Chemical Engineering Science 52 (1997), Nr. 8, 1365-1376

[Bin00]   F. E. Bingham, E. Chan, Improved reactor internals for Syncrude's HGO hydrotreaters, NPRA annual meeting, 2000

[Blu00]   B. Blümich, NMR imaging of materials. Clarendon press, Oxford (2000)

[Boe01]   J. G. Boelhouwer, Nonsteady operation of trickle-bed reactors – Hydrodynamics, mass and heat transfer, Ph. D. thesis, University Eindhoven, (2001).

[Bur04]   V. van Buren, Modellierung der Tropfenabscheidung im Anfahrbereich von Schüttschichtfiltern auf Basis von MRI-Untersuchungen, Ph. D. thesis, Universität Karlsruhe (2004)

[Bur90]   A. Burghardt, A. S. Kolodzief, M. Jaroszynski, Experimental studies of liquid-solid wetting efficiency in trickle bed cocurrent reactors, Chemical Engineering and Processing 28 (1990), 35-49

[Cal91]   P. T. Callaghan, Principles of Nuclear Magnetic Resonance. Microscopy. Clarendon Press, Oxford, (1991).

[Che04]   J. Chen, H. Yang, Z. Ring, HDS kinetics study of dibenzothiophenic compounds in LCO. Catalysis today 98 (2004), Nr. 1-2, 227-233

[Cho02]   R. Chowdhury, E. Pedemera, R. Reimert, Trickle-Bed Reactor Model for Desulfurization and Dearomatization of Diesel. AIChE journal 48 (2002), Nr. 1, 126-135

[Coh81]   Y. Cohen, A. B. Metzner, Wall effects in laminar flow of fluids through packed beds. AIChE Journal. 27 (1981), Nr. 5, 705-715

[Cou01]   L. Coulier, Hydrotreating model catalyst: from characterization to kinetics, Ph. D. Thesis, University Eindhoven, (2001).

[Cri81]   M. Crine, P. Marchot, Measuring dynamic liquid holdup in trickle bed reactors under actual operating conditions. Chem. Eng. Comm. 8 (1981), 365-371

[EIA10]   Annual energy review, http://www.eia.doe.gov/aer/

[Dan53]   P. V. Danckwerts, Continuous Flow Systems. Distribution of Residence Times. Chemical Engineering Science, 2 (1953), 1-13

[Dgm02]   Information from Tagung der DGMK-Bezirksgruppe Ruhr, 07.05.2002

[Dud02]   M. P. Dudukovic, F. Larachi, P. L. Mills, Multiphase catalytic reactors: a perspective on current knowledge and future trends. Catalysis Review 44 (2002), Nr. 1, 123-246

[Dud77]   M. P. Dudukovic, Catalyst effectiveness factor and contacting efficiency in trickle bed reactor, AIChE journal 23 (1977), Nr. 6, 940-944

[Fin04]   U. Fink, F. Hajduk, M. Yoneyama, Catalyst demand reflects diverse drivers – Regulatory mandates for cleaner fuels, fewer emissions and purer pharmaceuticals are among the forces driving market demand and new technology development. Chemical Engineering 111 (2004), Nr. 7, 17-19

[Flu03]   Fluent 6.1 user's guide, volume 2 (2003)

[Fro90]   G. F. Froment; K. B. Bischoff, Chemical reactor analysis and design, 1990, 2. ed. – New York : Wiley

[Gia92]   A. Gianetto, V. Specchia, Trickle bed reactors: state of the art and perspectives. Chemical Engineering Science 47 (1992), 3197-3213

[Gie88]   H. Gierman, Design of laboratory hydrotreating reactors. Scaling down of trickle bed reactors, Applied Catalysis, 43(1988), 277-286

[Gie98]   M. Giese, Strömung in porösen Medien unter Berücksichtigung effektiver Viskositäten, Ph. D. thesis, Technische Universität München (1998)

[Gla96]   L. F. Gladden, P. Alexander, Applications of nuclear magnetic resonance imaging in process engineering. Measurement Science and Technology 7 (1996), 423-435

[Gun03]   P. R. Gunjal, V. V. Ranade, R. V. Chaudhari. Liquid distribution and RTD in trickle bed reactors: experiments and CFD simulations. The Canadian Journal of Chemical Engineering 81 (2003), 821-830

References

[Gun07]   P. R. Gunjal; V. V. Ranade, Modeling of laboratory and commercial scale hydro-processing reactors using CFD. Chemical engineering science, 62 (2007), 5512-5526

[Har04]   www.hartwrfs.com, World refining and fuels analysis, 2000-2015

[Har06]   E. H. Hardy, Magnetic Resonance Imaging in chemical engineering: basics and practical aspects, Chemical Engineering & Technology 29 (2006), Nr. 7, 785-795

[Hau89]   P. M. Haure, R. R. Hudgins, P. L. Silveston, Periodic operation of a trickle-bed reactor. AIChE J. 35 (1989), 1437-1444

[Hei04]   C. Heinen, MRI Untersuchungen zur Strömung newtonischer und nicht-newtonischer Fluide in porösen Strukturen. Ph. D. thesis, Universität Karlsruhe (2004)

[Ho04]   T. C. Ho, Deep HDS of diesel fuel: chemistry and catalysis, Catalysis Today, 98 (2004), Nr. 1-2, 3-18

[IEA07]   Oil supply security – emergency response of IEA countries, IEA (2007)

[Jes64]   R. Jeschar, Druckverlust in Mehrkornschüttungen aus Kugeln. Archiv Eisenhüttenwesen, 35 (1964), 91-108

[Jia01]   Y. Jiang, M. H. Al-Dahhan, M. P. Dudukovic, Statistical characterization of macroscale multiphase flow textures in trickle beds. Chemical Engineering Science. 56 (2001), Nr. 4, 1647-1656

[Jia02]   Y. Jiang, M. R. Khadilkar, M. H. Al-Dahhan, M. P. Dudukovic, CFD of multiphase flow in packed bed reactors: I. k-fluid modelling issues. AIChE Journal 48 (2002), Nr. 4, 701-715

[Kab99]   T. Kabe, A. Ishihara, W. Qian, Hydrodesulfurization and hydrodenitrogenation, Wiley-VCH (1999), ISBN 3-527-30116

[Kim97]   R. Kimmich, NMR Tomography, Diffusometry, Relaxometry, Springer-Verlag (1997), ISBN 3-540-61822-8

[Kop04]   I. V. Koptyug, A. A. Lysova, A. V. Kulikov, V. A. Kirillov, V. N. Parmon, R. Z. Sagdeev, Functional imaging and NMR spectroscopy of an operating gas-liquid-solid catalytic reactor. Applied Catalysis A 267 (2004), 143-148

[Kor96]   H. Korsten, U. Hoffmann, Three-Phase Reactor Model for Hydrotreating in Pilot Trickle-Bed Reactors. AIChE Journal, 42 (1996), Nr. 5, 1350-1360

[Kut96]   Y. E. Kutsovsky, L. E. Scriven, H. T. Davis, NMR imaging of velocity profiles and velocity distributions in bead packs. Physics of Fluids, 8 (1996), Nr. 4, 863-871

[Lar03]   F. Larachi, L. Belfares, I. Iliuta, B. P. A. Grandjean, Heat and Mass Transfer in Cocurrent Gas-Liquid Packed Beds. Analysis, Recommendations, and New Correlations. Industrial & Engineering Chemistry Research, 42 (2003), Nr. 1, 222-242

[Lev93]   O. Levenspiel, The chemical reactor omnibook. Corvallis, Or. (1993) ISBN: 0-88246-160-5

[Luc00]   A. G. Lucas, Modern petroleum technology, Volume 2: Downstream. John Wiley & Son, LTD, (2000)

[Mac04]   M. J. Macias, J. Ancheyta, Simulation of an isothermal hydrodesulfurization small reactor with different catalyst particle shapes. Catalysis Today 98 (2004), Nr. 1-2, 243-252

[Man01]   T. Mang, W. Dresel, Lubricants and lubrications. Wiley-VCH, (2001). Chapter 3.2, 23-25

[Mar63]   D. W. Marquardt, An algorithm for least squares estimation of nonlinear parameters. Journal of the Society of Industrial and Applied Mathematics 2 (1963), 431-441.

[Mar78]   H. Martin, Low peclet number particle-to-liquid heat and mass transfer in packed beds. Chemical Engineering Science 33 (1978), 913-919

[Mea71]   D. E. Mears, The role of axial dispersion in trickle flow laboratory reactors, Chemical Engineering Science 26 (1971), 1361-1366

[Moc96]   I. Mochida, K. Sakanishi, X. Ma, S. Nagao, T. Isoda, Deep hydrodesulfurization of diesel fuel: Design of reaction process and catalysts. Catalysis Today 29 (1996), Nr. 1-4, 185-190

[Mue91]   G. E. Mueller, Prediction of radial porosity distribution in randomly packed beds of uniformly sized spheres in cylindrical containers. Chemical Engineering Science 46 (1991), 706-708

[Nar02]   C. S. L. Narashimhan, R. P. Verma, A. Kundu, K. D. P. Nigam, Modeling hydrodynamics of trickle bed reactors at high pressure. AIChE Journal 48(2002), Nr. 11, 2459-2470

[Niu96]   M. Niu, T. Akiyama, R. Takahashi, J. Yagi, Reduction of the wall effect in a packed bed by a hemispherical lining. AIChE Journal 42(1996), Nr. 4, 1181-1186

[Ped03]   E. Pedernera, Tiefentschwefelung von Dieselöl im Rieselfilmreaktor, Ph. D. Thesis, Universität Karlsruhe, (2003)

[Pet03]   G. Petritsch, N. Reinecke, D. Mewes, Visualization techniques in process engineering. Ullman's Encyclopedia 38 (2003), 87-108

[Ran02]   V. V. Ranade, Computational flow modelling for chemical reactor engineering. Academic Press, San Diego, California, (2002).

[Rei98]   N. Reinecke, G. Petritsch, D. Schmitz, D. Mewes, Tomographic Measurement Techniques - Visualization of Multiphase Flows. Chemical Engineering & Technology 21 (1998), Nr. 1, 18-20

[Rei99]   H. R. Reinhoudt, The development of novel catalysts for deep hydrodesulfurization of diesel fuel, Ph. D. Thesis, University Delft, (1999)

[Ren03]   X. Ren, NMR Studies of Molecular Transport in Model Fixed-Bed Reactors, Ph. D. thesis, Technischen Hochschule Aachen (2003)

[Rid68]   K. Ridgway, K. J. Tarbuck, Voidage fluctuations in randomly packed beds of spheres adjacent to a containing wall. Chemical Engineering Science 23 (1968), 1147-1155

[Rin89]   Z.E, Ring, R. W. Missen, Trickle-bed reactors: an experimental study of partial wetting effect, AIChE journal 35 (1989), Nr. 11, 1821-1828

[Rob58]   L. H. S. Roblee, R. M. Baird, J. W. Tierney, Radial porosity variations in packed beds. AIChE Journal 4 (1958), 460-464

[Rot96]   K. Rottschäfer, Geschwindigkeitsverteilungen in durchströmten Füllkörperschüttungen. Ph. D. thesis, Technische Universität München (1996).

[Sar96]   A. K. Saroha, K. D. P. Nigam, Trickle bed reactors, Reviews in Chemical Engineering, 12 (1996), Nr. 3-4, 207

[Sch99]   H. Schulz, W. Böhringer, F. Ousmanov, P. Waller, Refractory sulfur compounds in gas oils. Fuel Processing Technology 61(1999), 5-41

[Sed97]   A. J. Sederman, M. L. Johns, A. S. Bramley, P. Alexander, L. F. Gladden, Magnetic resonance imaging of liquid flow and pore structure within packed beds. Chemical engineering science 52 (1997), Nr. 14, 2239-2250

[Sed01]   A. J. Sederman, L. F. Gladden, Magnetic resonance imaging as a quantitative probe of gas-liquid distribution and wetting efficiency in trickle bed reactors. Chemical engineering science 56 (2001), 2615-2628

[Sha01]   Sharma, S.; Mantle, M. D.; Gladden, L. F.; Winterbottom, J. M., Determination of bed voidage using water substitution and 3D magnetic resonance imaging, bed denstity and pressure drop in packed bed reactors. Chemical Engineering Science 56 (2001), Nr. 2, 587-595

[Sie98a]   S. T. Sie, R. Krishna, Process development and scale up: 1. Process development strategy and methology. Reviews in chemical engineering 14 (1993), Nr. 1, 47-88

[Sie98b]   S. T. Sie, R. Krishna, Process development and scale up: 2. Catalyst design strategy. Reviews in chemical engineering 14 (1993), Nr. 3, 159-202

[Sie98c]   S. T. Sie, R. Krishna, Process development and scale up: 3. Scale-up and scale-down of trickle bed processes, Reviews in Chemical Engineering, 14 (1998), Nr. 3, 203-251

[Sil04]   R. P. Silvy, Future trends in the refining catalyst market. Applied catalysts A 261 (2004), Nr. 2, 247-252

[Son03]   C. Song, X. Ma, New design approaches to ultra-clean diesel fuels by deep desulfurization and deep dearomatization, Applied Catalysis B, 41 (2003), Nr. 1, 207-238

[Spe77]   V. Specchia, G. Baldi, Pressure drop and liquid holdup for two phase cocurrent flow in packed beds. Chemical Engineering Science, 32 (1977), 515-523

[Sta06]   S. Stapf; S. Han, Nuclear Magnetic Resonance Imaging in Chemical Engineering. Wiley-VCH, Weinheim (2006)

[Stan94]   A. Stanislaus, B. H. Cooper, Aromatic Hydrogenation Catalysis: A Review. Catalysis Reviews: Science and Engineering, 36 (1994), Nr. 1, 75-124

[Sue03]   T. Suekane, Y. Yokouchi, S. Hirai, Inertial Flow Structures in a Simple-Packed Bed of Spheres. AIChE Journal 49 (2003), Nr. 1, 10-17

[Te03]   M. Te, C. Fairbridge, Z. Ring, Various approachs in kinetics modelling of real feedstock hydrodesulfurization, Petroleum Science and Technology, 21 (2003), Nr. 1-2, 157-181

[Toy96]   D. Toye, P. Marchot, M. Crine, G. L'Homme, Modelling of multiphase flow in packed beds by computer-assisted x-ray tomography. Measurement Science and Technology 7 (1996), Nr. 3, 436-443

[Tur59]   G. A. Turner, G. F. Hewitt, The amount of liquid held at the point of contact of spheres and the static liquid hold-up in packed beds. Trans. Inst. Chem. Eng. 37 (1959), 329

[Ull06]   W. W. Irion, O. S. Neuwirth, Oil refining. Ullmann's Encyclopedia of Industrial Chemistry, electronic version, 7th edition (2006), 1-52

[Vor83]   D. Vortmeyer, J. Schuster, Evaluation of steady flow profiles in rectangular and circular packed beds by a variational method. Chemical Engineering Science 38 (1983), Nr. 10, 406-413

[Wam91] W. J. A. Wammes, K. R. Westerterp, Hydrodynamics in a pressurized cocurrent gas-liquid trickle bed reactor. Chem. Eng. Technol. 14 (1991), 406-413

[Wan01] Z. Wang, A. Afacan, K. Nandakumar, K. T. Chuang, Porosity distribution in random packed columns by gamma ray tomography. Chemical Engineering and Processing 40 (2001), Nr. 3, 209-220

[Wes92] K. R. Westerwerp, W.J. A. Wammes, Three-phase trickle bed reactors, Ullman's Encyclopedia of Industrial Chemistry, Vol. B4 (1992), 309-321

[Whi98] D. D.Whitehurst, T. Isoda, I. Mochida, Isao, Present State of the Art and Future Challenges in the Hydrodesulfurization of Polyaromatic Sulfur Compounds, Advances in Catalysis 42 (1998), 345-472

[Yin02] F. Yin, A. Afacan, K. Nandakumar, K. T. Chuang, Liquid holdup distribution in packed columns: gamma ray tomography and CFD simulation. Chemical Engineering and Processing 41 (2002), 473-483

Appendices

Appendix A: In this appendix literature models for prediction of radial porosity distribution in random packed beds of spherical particles are given. Besides, the relative errors between the porosity's values of each packed bed determined by gravitational method and MRI-method, respectively, are presented.

Model of Martin [Mar78]	
$$\varepsilon(\frac{x}{d_p}) = \begin{cases} \varepsilon_{min} + (1-\varepsilon_{min})\left(\frac{R-x}{0.55\,d_p}-1\right)^2 & for \quad \frac{R-x}{d_p} \leq 0.55 \\ \varepsilon_\infty + A\exp\left[B\left(\frac{R-x}{d_p}\right)\right]\cos\left[2\pi\left(C\left(\frac{R-x}{d_p}\right)+D\right)\right] & for \quad \frac{R-x}{d_p} \geq 0.55 \end{cases}$$ *where* $\varepsilon_{min} = 0.23$; $\varepsilon_\infty = 0.39$; $A = 0.26$; $B = -0.32$; $C = 1.12$; $D = -0.14$	(A. 1)
Model of Cohen and Metzner [Coh81]	
$$\frac{1-\varepsilon}{1-\varepsilon_\infty} = \begin{cases} 4.5\left(x - \frac{7}{9}x^2\right) & for \quad \frac{x}{d_p} \geq 0.25 \\ a_1 e^{\left(-a_2\frac{x}{d_p}\right)}\cos\Pi\left(a_3\frac{x}{d_p}-a_4\right) & for \quad 0.25 \leq \frac{x}{d_p} \leq 8 \end{cases}$$ $$\varepsilon\left(\frac{x}{d_p}\right) = \varepsilon_\infty \qquad\qquad for \quad \frac{x}{d_p} \geq 8$$ *where* $\varepsilon_\infty = 0.39$; $a_1 = 0.3463$; $a_2 = 0.4276$; $a_3 = 2.4509$; $a_4 = 2.2011$	(A. 2)
Model of Giese [Gie98]	
$$\varepsilon\left(\frac{x}{d_p}\right) = \begin{cases} \varepsilon_\infty\left[a_1 + b_1\left(\frac{x}{d_p}\right) + c_1\left(\frac{x}{d_p}\right)^2\right] & for \quad \frac{x}{d_p} < e_2 \\ \varepsilon_\infty\left[a_2 + b_2 e^{\left\{d_2\left(\frac{x}{d_p}\right)\right\}^{f_2}}\cos\left\{c_2\left(\frac{x}{d_p}\right)-e_2\right\}\right] & for \quad \frac{x}{d_p} > e_2 \end{cases}$$ *where* $a_1 = 7.3025$; $a_2 = 1$; $b_1 = -7.7405$; $b_2 = -0.51821$; $c_1 = 2.5384$; $c_2 = 6.9813$; $d_2 = -0.15$; $e_2 = 0.55$; $f_2 = 1.5$; $\varepsilon_\infty = 0.39$	(A. 3)

Model of Mueller [Mue91]	(A. 4)

$$\varepsilon\left(\frac{x}{d_p}\right) = \varepsilon_\infty + (1-\varepsilon_\infty)J_0\left(a\frac{x}{d_p}\right)e^{\left(-b\frac{x}{d_p}\right)} \qquad for \quad \frac{x}{d_p} \geq 2.61$$

where :

$$a = 8.243 - \frac{12.98}{\frac{D}{d_p}+3.156} \quad for \quad 2.61 \leq \frac{D}{d_p} \leq 13$$

$$a = 7.383 - \frac{2.932}{\frac{D}{d_p}-9.864} \quad for \quad \frac{D}{d_p} > 13; \; b = 0.304 - \frac{0.724}{\frac{D}{d_p}} \; ; \; \varepsilon_\infty = 0.334 + \frac{0.22}{\frac{D}{d_p}}$$

J_0 *is a zero order Bessel function of the first kind*

Model of Rottschäfer [Rot96]	(A. 5)

$$\varepsilon(x_{Fo}) = c_3 \cdot \left(c_1 + \sum_{a=1}^{10}\frac{\cos(a \cdot x_{Fo})(-1)^a}{a^2}\right) \cdot e^{c_2 x_{Fo}} + \varepsilon_\infty$$

where

$$x_{Fo} = \pi\left(1 + \frac{1}{c_{max}}\left(2(c_{max}-1) + \frac{x}{d_p} + \sqrt{4\left(1-\frac{x}{d_p}\right)(c_{max}-1)^2 + \left(\frac{x}{d_p}\right)^2}\right)\right)$$

$$c_3 = \frac{\varepsilon_w - \varepsilon_\infty}{\left(c_1 + \sum_{a=1}^{10}\frac{\cos(a\pi)(-1)^a}{a^2}\right)e^{C_2\pi}}$$

$$\varepsilon_\infty = 0.375 + 0.34\frac{d_p}{D} \; ; \; \varepsilon_w = 1.0 \; ; \; c_{max} = 0.9 \; ; \; c_1 = 0.097 \; ; \; c_2 = -0.11$$

Table A1: Summary of important published models predicting radial porosity distributions

	Raschig ring d_p = 5 mm	Raschig ring d_p = 3 mm	Cylinder d_p=3.2 mm	Trilobe catalyst d_p= 2 mm
D_i (cm)	5	5	5	5
L (cm)	29.3	28.3	28.2	27.7
V_{bed} = $\pi*D_i^2/4*L$ (cm^3)	575.304	555.669	553.705	553.706
m_{water} (g)	416	312	367.6	464.9
ε_1 = $V_{voidage}/V_{bed}$ = $m_{water}*\rho_{water}/V_{bed}$	0.723	0.561	0.352	0.423
ε_2 from MRI-data	0.716	0.557	0.355	0.428
relative error between ε_1 and ε_2 (%)	0.98	0.77	1.07	1.17

Table A2: Comparison of the porosities determined by gravitational method (ε_1), and MRI-method (ε_2). Density of water is ρ_{water} = 1g/cm^3.

Appendix B: Numerical solution of HDS model

The set of differential equations 7.10 – 7.14 in chapter 7.4 is numerically solved by Newton's method. The central difference approximation was applied to discretize the equations. To do this, an equally spaced grid of P points was established along the length of the reactor with grid spacing h. The equations at i^{th} grid point (for i = 2 to i = P-1) are then as follows:

$$\frac{P_{1,i+1} - P_{1,i-1}}{2h} + \alpha_1 \left(P_{1,i} - \varphi_{2,i}\right) = 0$$

$$\frac{P_{2,i+1} - P_{2,i-1}}{2h} + \alpha_2 \left(P_{2,i} - \varphi_{3,i}\right) = 0$$

$$\frac{\varphi_{1,i+1} - 2\varphi_{1,i} + \varphi_{1,i-1}}{h^2} - Pe \frac{\varphi_{1,i+1} + \varphi_{1,i-1}}{2h} - R_1 \frac{\varphi_{1,i}^{n1} \varphi_{2,i}^{n2}}{\left(1 + k_{ad} C_{H2S,L0} \varphi_{3,i}\right)^2} = 0$$

$$\frac{\varphi_{2,i+1} - 2\varphi_{2,i} + \varphi_{2,i-1}}{h^2} - Pe \frac{\varphi_{2,i+1} + \varphi_{2,i-1}}{2h} + R_2 \left(1 - \varphi_{2,i}\right) - R_3 \frac{\varphi_{1,i}^{n1} \varphi_{2,i}^{n2}}{\left(1 + k_{ad} C_{H2S,L0} \varphi_{3,i}\right)^2} = 0$$

$$\frac{\varphi_{3,i+1} - 2\varphi_{3,i} + \varphi_{3,i-1}}{h^2} - Pe \frac{\varphi_{3,i+1} + \varphi_{3,i-1}}{2h} + R_2 \left(1 - \varphi_{3,i}\right) - R_4 \frac{\varphi_{1,i}^{n1} \varphi_{2,i}^{n2}}{\left(1 + k_{ad} C_{H2S,L0} \varphi_{3,i}\right)^2} = 0$$

At the end points, the boundary conditions are applied. At the first point (i = 1, Z=0), all the concentrations are known, so the equations there are:

$$P_{1,1} = P_{2,1} = \varphi_{1,1} = \varphi_{2,1} = \varphi_{3,1} = 1$$

At the last grid point, the gradient of each of the quantities is zero according to Danckwert's boundary, so the equations are:

$$\left.\frac{d\varphi_1}{dZ}\right|_{Z=1} = \left.\frac{d\varphi_2}{dZ}\right|_{Z=1} = \left.\frac{d\varphi_3}{dZ}\right|_{Z=1} = 0$$

$$\frac{\varphi_{1,P} - \varphi_{1,P-1}}{h} = \frac{\varphi_{2,P} - \varphi_{2,P-1}}{h} = \frac{\varphi_{3,P} - \varphi_{3,P-1}}{h} = 0$$

or $\quad \varphi_{1,P} = \varphi_{1,P-1}; \varphi_{2,P} = \varphi_{2,P-1}; \varphi_{3,P} = \varphi_{3,P-1}$

and $\quad P_{1,p} = P_{1,p-1}; \quad P_{2,p} = P_{2,p-1}$

This set of non-linear algebraic equations must be solved by using Newton's method. In preparation for doing so, the unknowns can be arranged in a vector (which is called $\underline{y}$) as follows:

$$\underline{y} = \begin{bmatrix} P_{1,1} & P_{2,1} & \varphi_{1,1} & \varphi_{2,1} & \varphi_{3,1} & P_{1,2} & P_{2,2} & \varphi_{1,2} & \cdots & P_{1,P} & P_{2,P} & \varphi_{1,P} & \varphi_{2,P} & \varphi_{3,P} \end{bmatrix}^T$$

where the superscript T indicates the transpose of the vector. The corresponding vector of algebraic equations can be written as $\underline{f}(\underline{y})$ as shown in the following.

$$\underline{f} = \begin{bmatrix}
P_{1,1} - 1 \\[4pt]
P_{2,1} - 1 \\[4pt]
\varphi_{1,1} - 1 \\[4pt]
\varphi_{2,1} - 1 \\[4pt]
\varphi_{3,1} - 1 \\[4pt]
\dfrac{P_{1,3} - P_{1,1}}{2h} + \alpha_1\left(P_{1,2} - \varphi_{2,2}\right) \\[10pt]
\dfrac{P_{2,3} - P_{2,1}}{2h} + \alpha_2\left(P_{2,2} - \varphi_{3,2}\right) \\[10pt]
\dfrac{\varphi_{1,3} - 2\varphi_{1,2} + \varphi_{1,1}}{h^2} - Pe\,\dfrac{\varphi_{1,3} - \varphi_{1,1}}{2h} - R_1\dfrac{\varphi_{1,2}^{n1}\varphi_{2,2}^{n2}}{\left(1 + k_{ad}C_{H2S,L0}\varphi_{3,2}\right)^2} \\[14pt]
\dfrac{\varphi_{2,3} - 2\varphi_{2,2} + \varphi_{2,1}}{h^2} - Pe\,\dfrac{\varphi_{2,3} - \varphi_{2,1}}{2h} + R_2\left(1 - \varphi_{2,2}\right) - R_3\dfrac{\varphi_{1,2}^{n1}\varphi_{2,2}^{n2}}{\left(1 + k_{ad}C_{H2S,L0}\varphi_{3,2}\right)^2} \\[14pt]
\dfrac{\varphi_{3,3} - 2\varphi_{3,2} + \varphi_{3,1}}{h^2} - Pe\,\dfrac{\varphi_{3,3} - \varphi_{3,1}}{2h} + R_2\left(1 - \varphi_{3,2}\right) - R_4\dfrac{\varphi_{1,2}^{n1}\varphi_{2,2}^{n2}}{\left(1 + k_{ad}C_{H2S,L0}\varphi_{3,2}\right)^2} \\[14pt]
\vdots \\
\vdots \\[6pt]
\dfrac{P_{1,P} - P_{1,P-2}}{2h} + \alpha_1\left(P_{1,P-1} - \varphi_{2,P-1}\right) \\[10pt]
\dfrac{P_{2,P} - P_{2,P-2}}{2h} + \alpha_2\left(P_{2,P-1} - \varphi_{3,P-1}\right) \\[10pt]
\dfrac{\varphi_{1,P} - 2\varphi_{1,P-1} + \varphi_{1,P-2}}{h^2} - Pe\,\dfrac{\varphi_{1,P} - \varphi_{1,P-2}}{2h} - R_1\dfrac{\varphi_{1,P-1}^{n1}\varphi_{2,P-1}^{n2}}{\left(1 + k_{ad}C_{H2S,L0}\varphi_{3,P-1}\right)^2} \\[14pt]
\dfrac{\varphi_{2,P} - 2\varphi_{2,P-1} + \varphi_{2,P-2}}{h^2} - Pe\,\dfrac{\varphi_{2,P} - \varphi_{2,P-2}}{2h} + R_2\left(1 - \varphi_{2,P-1}\right) - R_3\dfrac{\varphi_{1,P-1}^{n1}\varphi_{2,P-1}^{n2}}{\left(1 + k_{ad}C_{H2S,L0}\varphi_{3,P-1}\right)^2} \\[14pt]
\dfrac{\varphi_{3,P} - 2\varphi_{3,P-1} + \varphi_{3,P-2}}{h^2} - Pe\,\dfrac{\varphi_{3,P} - \varphi_{3,P-2}}{2h} + R_2\left(1 - \varphi_{3,P-1}\right) - R_4\dfrac{\varphi_{1,P-1}^{n1}\varphi_{2,P-1}^{n2}}{\left(1 + k_{ad}C_{H2S,L0}\varphi_{3,P-1}\right)^2} \\[14pt]
P_{1,P} - P_{1,P-1} \\[4pt]
P_{2,P} - P_{2,P-1} \\[4pt]
\varphi_{1,P} - \varphi_{1,P-1} \\[4pt]
\varphi_{2,P} - \varphi_{2,P-1} \\[4pt]
\varphi_{3,P} - \varphi_{3,P-1}
\end{bmatrix}$$

For purposes of solving the equations, it is useful to number the components of vector $\underline{y}$ of length $5P$ as follows:

$$\underline{f}(\underline{y}) = \begin{bmatrix}
y_1 - 1 \\
y_2 - 1 \\
y_3 - 1 \\
y_4 - 1 \\
y_5 - 1 \\
\dfrac{y_{11} - y_1}{2h} + \alpha_1(y_6 - y_9) \\
\dfrac{y_{12} - y_2}{2h} + \alpha_2(y_7 - y_{10}) \\
\dfrac{y_{13} - 2y_8 + y_3}{h^2} - Pe\,\dfrac{y_{13} - y_3}{2h} - R_1 \dfrac{y_8^{n1} y_9^{n2}}{\left(1 + k_{ad} C_{H2S,L0} y_{10}\right)^2} \\
\dfrac{y_{14} - 2y_9 + y_4}{h^2} - Pe\,\dfrac{y_{14} - y_4}{2h} + R_2(1 - y_9) - R_3 \dfrac{y_8^{n1} y_9^{n2}}{\left(1 + k_{ad} C_{H2S,L0} y_{10}\right)^2} \\
\dfrac{y_{15} - 2y_{10} + y_5}{h^2} - Pe\,\dfrac{y_{15} - y_5}{2h} + R_2(1 - y_{10}) - R_4 \dfrac{y_8^{n1} y_9^{n2}}{\left(1 + k_{ad} C_{H2S,L0} y_{10}\right)^2} \\
\vdots \\
\vdots \\
\dfrac{y_{5p-4} - y_{5P-14}}{2h} + \alpha_1\left(y_{5P-9} - y_{5P-6}\right) \\
\dfrac{y_{5P-3} - y_{5P-13}}{2h} + \alpha_2\left(y_{5P-8} - y_{5P-6}\right) \\
\dfrac{y_{5P-2} - 2y_{5P-7} + y_{5P-12}}{h^2} - Pe\,\dfrac{y_{5P-2} - y_{5P-12}}{2h} - R_1 \dfrac{y_{5P-7}^{n1} y_{5P-6}^{n2}}{\left(1 + k_{ad} C_{H2S,L0} y_{5P-5}\right)^2} \\
\dfrac{y_{5P-1} - 2y_{5P-6} + y_{5P-11}}{h^2} - Pe\,\dfrac{y_{5P-1} - y_{5P-11}}{2h} + R_2(1 - y_{5P-6}) - R_3 \dfrac{y_{5P-7}^{n1} y_{5P-6}^{n2}}{\left(1 + k_{ad} C_{H2S,L0} y_{5P-5}\right)^2} \\
\dfrac{y_{5P} - 2y_{5P-5} + y_{5P-10}}{h^2} - Pe\,\dfrac{y_{5P} - y_{5P-10}}{2h} + R_2(1 - y_{5P-5}) - R_4 \dfrac{y_{5P-7}^{n1} y_{5P-6}^{n2}}{\left(1 + k_{ad} C_{H2S,L0} y_{5P-5}\right)^2} \\
y_{5P-4} - y_{5P-9} \\
y_{5P-3} - y_{5P-8} \\
y_{5P-2} - y_{5P-7} \\
y_{5P-1} - y_{5P-6} \\
y_{5P} - y_{5P-5}
\end{bmatrix}$$

The Newton method for a system of equations is:

$$\underline{y}_i^{k+1} = \underline{y}_i^k - \underline{\underline{J}}_{ij}^k \underline{f}(\underline{y}^k) \text{ for } 1 \le k \le 5P;\ 1 \le i \le P \text{ and } 1 \le j \le 5$$

where $\underline{\underline{J}}_{ij}^k$ is the Jacobian matrix as defined by: $\underline{\underline{J}}_{ij}^k = \left.\dfrac{\partial \underline{f}_i}{\partial \underline{y}_j}\right|_{\underline{y}k}$

The Jacobian matrix is made up of 5x5 sub-matrices, since the equation system has 5 independent variables.

$$\underline{\underline{J}} = \begin{bmatrix} \underline{\underline{M}}_{1,1} & \underline{\underline{0}} & \underline{\underline{0}} & \underline{\underline{0}} & \underline{\underline{0}} & \cdots & \underline{\underline{0}} & \underline{\underline{0}} & \underline{\underline{0}} & \underline{\underline{0}} \\ \underline{\underline{M}}_{2,1} & \underline{\underline{M}}_{2,2} & \underline{\underline{M}}_{2,3} & \underline{\underline{0}} & \underline{\underline{0}} & \cdots & \underline{\underline{0}} & \underline{\underline{0}} & \underline{\underline{0}} & \underline{\underline{0}} \\ \underline{\underline{0}} & \underline{\underline{M}}_{3,2} & \underline{\underline{M}}_{3,3} & \underline{\underline{M}}_{3,4} & \underline{\underline{0}} & \cdots & \underline{\underline{0}} & \underline{\underline{0}} & \underline{\underline{0}} & \underline{\underline{0}} \\ \underline{\underline{0}} & \underline{\underline{0}} & \underline{\underline{M}}_{4,3} & \underline{\underline{M}}_{4,4} & \underline{\underline{M}}_{4,5} & \cdots & \underline{\underline{0}} & \underline{\underline{0}} & \underline{\underline{0}} & \underline{\underline{0}} \\ \cdots & \cdots & \cdots & \cdots & \cdots & \cdots & \cdots & \cdots & \underline{\underline{0}} & \underline{\underline{0}} \\ \cdots & \cdots & \cdots & \cdots & \cdots & \cdots & \cdots & \cdots & \cdots & \cdots \\ \underline{\underline{0}} & \underline{\underline{0}} & \underline{\underline{0}} & \underline{\underline{0}} & \cdots & \underline{\underline{M}}_{5P-3,5P-4} & \underline{\underline{M}}_{5P-3,5P-3} & \underline{\underline{M}}_{5P-3,5P-2} & \underline{\underline{0}} & \underline{\underline{0}} \\ \underline{\underline{0}} & \underline{\underline{0}} & \underline{\underline{0}} & \underline{\underline{0}} & \cdots & \underline{\underline{0}} & \underline{\underline{M}}_{5P-2,5P-3} & \underline{\underline{M}}_{5P-2,5P-2} & \underline{\underline{M}}_{5P-2,5P-1} & \underline{\underline{0}} \\ \underline{\underline{0}} & \underline{\underline{0}} & \underline{\underline{0}} & \underline{\underline{0}} & \cdots & \underline{\underline{0}} & \underline{\underline{0}} & \underline{\underline{M}}_{5P-1,5P-2} & \underline{\underline{M}}_{5P-1,5P-1} & \underline{\underline{M}}_{5P-1,5P} \\ \underline{\underline{0}} & \underline{\underline{0}} & \underline{\underline{0}} & \underline{\underline{0}} & \cdots & \underline{\underline{0}} & \underline{\underline{0}} & \underline{\underline{0}} & \underline{\underline{M}}_{5P,5P-1} & \underline{\underline{M}}_{5P,5P} \end{bmatrix}$$

where each of the sub-matrices $\underline{\underline{M}}_{i,j}$ is a 5 x 5 matrix of the appropriate derivaties.

$$\underline{\underline{M}}_{1,1} = \begin{bmatrix} 1 & 0 & 0 & 0 & 0 \\ 0 & 1 & 0 & 0 & 0 \\ 0 & 0 & 1 & 0 & 0 \\ 0 & 0 & 0 & 1 & 0 \\ 0 & 0 & 0 & 0 & 1 \end{bmatrix}$$

$$\underline{\underline{M}}_{2,1} = \begin{bmatrix} -\dfrac{1}{2h} & 0 & 0 & 0 & 0 \\ 0 & -\dfrac{1}{2h} & 0 & 0 & 0 \\ 0 & 0 & \dfrac{1}{h^2} + \dfrac{Pe}{2h} & 0 & 0 \\ 0 & 0 & 0 & \dfrac{1}{h^2} + \dfrac{Pe}{2h} & 0 \\ 0 & 0 & 0 & 0 & \dfrac{1}{h^2} + \dfrac{Pe}{2h} \end{bmatrix}$$

$$\underline{\underline{M}}_{2,2} = \begin{bmatrix} \alpha_1 & 0 & 0 & -\alpha_1 & 0 \\[2mm] 0 & \alpha_2 & 0 & 0 & -\alpha_2 \\[2mm] 0 & 0 & -\dfrac{2}{h^2} - \dfrac{n_1 R_1 \varphi_{1,2}^{n1-1} \varphi_{2,2}^{n2}}{\left(1 + k_{ad} C_{H2S,L0} \varphi_{3,2}\right)^2} & -\dfrac{n_2 R_1 \varphi_{1,2}^{n1} \varphi_{2,2}^{n2-1}}{\left(1 + k_{ad} C_{H2S,L0} \varphi_{3,2}\right)^2} & \dfrac{2 R_1 k_{ad} C_{H2S,L0} \varphi_{1,2}^{n1} \varphi_{2,2}^{n2}}{\left(1 + k_{ad} C_{H2S,L0} \varphi_{3,2}\right)^3} \\[4mm] 0 & 0 & -\dfrac{n_1 R_3 \varphi_{1,2}^{n1-1} \varphi_{2,2}^{n2}}{\left(1 + k_{ad} C_{H2S,L0} \varphi_{3,2}\right)^2} & -\dfrac{2}{h^2} - R_2 - \dfrac{n_2 R_3 \varphi_{1,2}^{n1} \varphi_{2,2}^{n2-1}}{\left(1 + k_{ad} C_{H2S,L0} \varphi_{3,2}\right)^2} & \dfrac{2 R_3 k_{ad} C_{H2S,L0} \varphi_{1,2}^{n1} \varphi_{2,2}^{n2}}{\left(1 + k_{ad} C_{H2S,L0} \varphi_{3,2}\right)^3} \\[4mm] 0 & 0 & -\dfrac{n_1 R_4 \varphi_{1,2}^{n1-1} \varphi_{2,2}^{n2}}{\left(1 + k_{ad} C_{H2S,L0} \varphi_{3,2}\right)^2} & -\dfrac{n_2 R_4 \varphi_{1,2}^{n1} \varphi_{2,2}^{n2-1}}{\left(1 + k_{ad} C_{H2S,L0} \varphi_{3,2}\right)^2} & -\dfrac{2}{h^2} - R_2 + \dfrac{2 R_4 k_{ad} C_{H2S,L0} \varphi_{1,2}^{n1} \varphi_{2,2}^{n2}}{\left(1 + k_{ad} C_{H2S,L0} \varphi_{3,2}\right)^3} \end{bmatrix}$$

$$\underline{\underline{M}}_{2,3} = \begin{bmatrix} \dfrac{1}{2h} & 0 & 0 & 0 & 0 \\[3mm] 0 & \dfrac{1}{2h} & 0 & 0 & 0 \\[3mm] 0 & 0 & \dfrac{1}{h^2} - \dfrac{Pe}{2h} & 0 & 0 \\[3mm] 0 & 0 & 0 & \dfrac{1}{h^2} - \dfrac{Pe}{2h} & 0 \\[3mm] 0 & 0 & 0 & 0 & \dfrac{1}{h^2} - \dfrac{Pe}{2h} \end{bmatrix}$$

Generally, a pattern for the three sub-matrices in a given row for $\ell = 2$ to $\ell = P-1$ is as follows.

$$\underline{\underline{M}}_{\ell,\ell-1} = \begin{bmatrix} -\dfrac{1}{2h} & 0 & 0 & 0 & 0 \\[3mm] 0 & -\dfrac{1}{2h} & 0 & 0 & 0 \\[3mm] 0 & 0 & \dfrac{1}{h^2} + \dfrac{Pe}{2h} & 0 & 0 \\[3mm] 0 & 0 & 0 & \dfrac{1}{h^2} + \dfrac{Pe}{2h} & 0 \\[3mm] 0 & 0 & 0 & 0 & \dfrac{1}{h^2} + \dfrac{Pe}{2h} \end{bmatrix}$$

109

$$\underline{\underline{M}}_{\ell,\ell} = \begin{bmatrix} \alpha_1 & 0 & 0 & -\alpha_1 & 0 \\[6pt] 0 & \alpha_2 & 0 & 0 & -\alpha_2 \\[6pt] 0 & 0 & -\dfrac{2}{h^2}-\dfrac{n_1 R_1 \varphi_{1,\ell}^{n1-1}\varphi_{2,\ell}^{n2}}{\left(1+k_{ad}C_{H2S,L0}\varphi_{3,\ell}\right)^2} & -\dfrac{n_2 R_1 \varphi_{1,\ell}^{n1}\varphi_{2,\ell}^{n2-1}}{\left(1+k_{ad}C_{H2S,L0}\varphi_{3,\ell}\right)^2} & \dfrac{2R_1 k_{ad}C_{H2S,L0}\varphi_{1,\ell}^{n1}\varphi_{2,\ell}^{n2}}{\left(1+k_{ad}C_{H2S,L0}\varphi_{3,\ell}\right)^3} \\[10pt] 0 & 0 & -\dfrac{n_1 R_3 \varphi_{1,\ell}^{n1-1}\varphi_{2,\ell}^{n2}}{\left(1+k_{ad}C_{H2S,L0}\varphi_{3,\ell}\right)^2} & -\dfrac{2}{h^2}-R_2-\dfrac{n_2 R_3 \varphi_{1,\ell}^{n1}\varphi_{2,\ell}^{n2-1}}{\left(1+k_{ad}C_{H2S,L0}\varphi_{3,\ell}\right)^2} & \dfrac{2R_3 k_{ad}C_{H2S,L0}\varphi_{1,\ell}^{n1}\varphi_{2,\ell}^{n2}}{\left(1+k_{ad}C_{H2S,L0}\varphi_{3,\ell}\right)^3} \\[10pt] 0 & 0 & -\dfrac{n_1 R_4 \varphi_{1,\ell}^{n1-1}\varphi_{2,\ell}^{n2}}{\left(1+k_{ad}C_{H2S,L0}\varphi_{3,\ell}\right)^2} & -\dfrac{n_2 R_4 \varphi_{1,\ell}^{n1}\varphi_{2,\ell}^{n2-1}}{\left(1+k_{ad}C_{H2S,L0}\varphi_{3,\ell}\right)^2} & -\dfrac{2}{h^2}-R_2+\dfrac{2R_4 k_{ad}C_{H2S,L0}\varphi_{1,\ell}^{n1}\varphi_{2,\ell}^{n2}}{\left(1+k_{ad}C_{H2S,L0}\varphi_{3,\ell}\right)^3} \end{bmatrix}$$

$$\underline{\underline{M}}_{\ell,\ell+1} = \begin{bmatrix} \dfrac{1}{2h} & 0 & 0 & 0 & 0 \\[8pt] 0 & \dfrac{1}{2h} & 0 & 0 & 0 \\[8pt] 0 & 0 & \dfrac{1}{h^2}-\dfrac{Pe}{2h} & 0 & 0 \\[8pt] 0 & 0 & 0 & \dfrac{1}{h^2}-\dfrac{Pe}{2h} & 0 \\[8pt] 0 & 0 & 0 & 0 & \dfrac{1}{h^2}-\dfrac{Pe}{2h} \end{bmatrix}$$

Finally, the last submatrices (ℓ = P) are:

$$\underline{\underline{M}}_{P,P-1} = \begin{bmatrix} -1 & 0 & 0 & 0 & 0 \\ 0 & -1 & 0 & 0 & 0 \\ 0 & 0 & -1 & 0 & 0 \\ 0 & 0 & 0 & -1 & 0 \\ 0 & 0 & 0 & 0 & -1 \end{bmatrix} \qquad \underline{\underline{M}}_{P,P} = \begin{bmatrix} 1 & 0 & 0 & 0 & 0 \\ 0 & 1 & 0 & 0 & 0 \\ 0 & 0 & 1 & 0 & 0 \\ 0 & 0 & 0 & 1 & 0 \\ 0 & 0 & 0 & 0 & 1 \end{bmatrix}$$

Now, the data of these matrices are then implemented in Matlab program to solve the equations.